

**Non-linear simulations of the interaction
of pre-existing magnetic islands in tokamak plasmas
with massive deuterium injection
for disruption mitigation**

Fabian Wieschollek

Vollständiger Abdruck der von der TUM School of Natural Sciences der Technischen Universität München zur Erlangung des akademischen Grades eines

Doktors der Naturwissenschaften (Dr. rer. nat.)

genehmigten Dissertation.

Vorsitz:

Prof. Dr. Katharina Krischer

Prüfer*innen der Dissertation:

1. Hon.-Prof. Dr. Sibylle Günter
2. Prof. Dr. Shimpei Futatani

Die Dissertation wurde am 03.04.2023 bei der Technischen Universität München eingereicht und durch die TUM School of Natural Sciences am 20.07.2023 angenommen.

Dissertation

Non-linear simulations of the interaction of pre-existing magnetic islands in tokamak plasmas with massive deuterium injection for disruption mitigation

Fabian Wieschollek

31. Januar 2023

Academic Supervisor: Hon.-Prof. Dr. Sibylle Günter
Scientific Supervisor: Dr. Matthias Hölzl

durchgeführt am Max-Planck-Institut für Plasmaphysik,
Garching bei München



MAX-PLANCK-INSTITUT
FÜR PLASMAPHYSIK



EUROfusion

Abstract

Motivated by the idea of generating energy through controlled nuclear fusion in a hot plasma, research has been ongoing since the fifties of last century in order to confine and stabilize such as plasma. One of the more promising approaches is the tokamak, where the plasma is confined within a toroidal device by magnetic fields. While the toroidal fraction of the field is produced by magnetic coils, the poloidal part is produced by the plasma itself from an induced toroidal current. However, this current makes the plasma prone to a set of magnetic instabilities – in particular the 2/1 neoclassical tearing mode – which can lead to full stochastization of the plasma and consequently a disruption, if not stopped early enough. This sudden loss of the plasma confinement can potentially damage large-scale machines. These consequences are massive heat loads, which primary damage first wall materials, massive mechanical loads, which could even damage supporting structures, and the generation of runaway electron, which are a threat to the first wall as well but could for example also destroy cooling systems and trigger a loss-of-coolant-accident, hence.

As it is unclear, if disruptions could ever be fully avoidable, approaches are followed to mitigate disruptions as a last line of defense. Massive material injection in the form of shattered pellet injection (SPI) is the mitigation approach followed for the large-scale experiment ITER. Diluting the plasma via deuterium SPI could mitigate the risk of runaway electron generation, which are more likely to establish at lower plasma densities. The motivation of the following work is to study, how reliably the material injection dilutes the plasma uniformly under the real circumstances of a disruption onset. The magnetic instabilities existing to this point can interact with the injected material, i.e., deteriorate the dilution or their growth can accelerate or decelerate. Hence, the non-linear extended magneto-hydrodynamic code JOEKEK was applied to investigate these questions in a fundamental, qualitative way for massive deuterium injection into an ASDEX Upgrade L-mode case, that may exhibit a pre-existing 2/1 magnetic island initially. A broad series of simulations were performed, which scan over several plasma and injection parameters. These are in particular the size of the pre-existing island, the amount of material injected and the toroidal phase between the pre-existing island and the injection nozzle. Also, the effect of different concentrations of background impurities – argon or tungsten – was investigated.

An amount of injected material was identified, which itself triggers full stochastization (FS) in an unperturbed case only at a late point in time, where all material is fully ablated and has diluted the plasma uniformly already for about one millisecond. This is an important case, as the effect of a pre-existing island is expected to be most pronounced and critical here. It is found that injecting this amount of material in the toroidal phase of the O-point of a large island, the FS is delayed further and only appears 1.5

Abstract

milliseconds after full ablation. This is a good, but unexpected behavior, as it gives more time for plasma dilution and provides time for additional measures against the disruption consequences in a multi-stage mitigation approach. However, simulations, on the other hand, show that injection into the X-point makes the plasma dynamics more violent and FS occurs earlier. A lower amount of injected material, which would not trigger FS alone in a plasma without a pre-existing island, drives the plasma into FS, if it is injected into the X-point. These observations suggest, in general, that in future experiments, the injection into the region of the X-point should be avoided. Further analyses have shown, that the current profile evolution, that is induced from the plasma injection, could be a relevant factor for the differences in the plasma behavior of the analyzed cases. The closer the injection is towards the X-point (or O-point), the more the profile changes its shape in a way which destabilizes (or stabilizes) the 2/1 magnetic island. All investigated cases suggest that the effect of the island itself on the dilution up to the point of FS is rather marginal, which can be understood as a positive observation in terms of disruption mitigation. The effect of background impurities does not change the overall dynamics: the delaying effect of an injection into the O-point is found to be smaller but still observable. For the case of X-point injection, the background impurities only have a very small impact. Overall, these simulations suggest that the injection of large amounts of deuterium to dilute the plasma and reduce the risk of runaway electron formation might still be applicable close to the onset of a natural disruption, where MHD mode activity has already occurred.

Zusammenfassung

Ausgehend von der Idee, Energie durch kontrollierte Kernfusion in einem heißen Plasma zu erzeugen, wird seit den fünfziger Jahren des letzten Jahrhunderts daran geforscht, ein solches Plasma einzuschließen und zu stabilisieren. Einer der vielversprechendsten Ansätze ist der Tokamak, bei dem das Plasma in einer toroidalen Vorrichtung durch Magnetfelder eingeschlossen wird. Während der toroidale Teil des Feldes durch Magnetspulen erzeugt wird, wird der poloidale Teil vom Plasma selbst durch einen induzierten toroidalen Strom erzeugt. Dieser Strom macht das Plasma jedoch anfällig für eine Reihe von magnetischen Instabilitäten - insbesondere der neoklassischen $2/1$ -Tearing-Mode - die zu einer vollständigen Stochastisierung des Plasmas und folglich zu einer Disruption führen können, wenn sie nicht rechtzeitig Gegenmaßnahmen getroffen werden. Dieser plötzliche Verlust des Plasmaeinschlusses kann potenziell großskalige Anlagen beschädigen. Die Folgen sind massive Wärmebelastungen, die primär die Materialien der ersten Wand schädigen, massive mechanische Belastungen, die sogar die tragenden Strukturen beschädigen könnten, und die Erzeugung von Runaway-Elektronen, die ebenfalls eine Bedrohung für die erste Wand darstellen, aber beispielsweise auch Kühlsysteme zerstören und damit einen Kühlmittelverluststörfall auslösen könnten.

Da unklar ist, ob sich Disruptionen jemals vollständig vermeiden lassen, werden als eine Art letztes Verteidigungsmittel Konzepte zur Mitigation von Disruptionen verfolgt. Massive Materialinjektion in Form der Injektion von zerbrochenen Pellets (SPI) ist der Ansatz zur Abschwächung von Störungen, der für das großskalige Experiment ITER verfolgt wird. Durch die Verdünnung des Plasmas mittels Deuterium-SPI könnte das Risiko einer Runaway-Elektronenerzeugung, die bei niedrigeren Plasmadichten wahrscheinlicher ist, gemindert werden. Die Motivation der folgenden Arbeit ist es, zu untersuchen, wie zuverlässig die Materialinjektion das Plasma unter den realen Umständen eines Disruptionseintritts gleichmäßig verdünnt. Die bis zu diesem Zeitpunkt vorhandenen magnetischen Instabilitäten können mit dem injizierten Material wechselwirken, d.h. die Verdünnung verschlechtern oder die Injektion das Modenwachstum beschleunigen oder verlangsamen. Daher wurde der nichtlineare erweiterte Magnetohydrodynamik-Code JOREK eingesetzt, um diese Fragen auf grundlegende, qualitative Weise für eine massive Deuterium-Injektion in einen ASDEX-Upgrade L-Mode-Fall zu untersuchen, der anfangs eine vorbestehende $2/1$ -magnetische Insel aufweisen kann. Es wurde eine breite Reihe von Simulationen durchgeführt, die mehrere Plasma- und Injektionsparameter scannen. Dies sind insbesondere die Größe der vorbestehenden Insel, die Menge des injizierten Materials und die toroidale Phase zwischen der vorbestehenden Insel und der Injektionsvorrichtung. Außerdem wurde die Wirkung verschiedener Konzentrationen von Hintergrundverunreinigungen - Argon oder Wolfram - untersucht.

Zusammenfassung

Es wurde eine Menge an injiziertem Material identifiziert, die selbst im ungestörten Fall die volle Stochastisierung (FS) erst zu einem späten Zeitpunkt auslöst, wenn alles Material vollständig verdampft ist und das Plasma bereits seit etwa einer Millisekunde gleichmäßig verdünnt hat. Dies ist ein wichtiger Fall, da die Wirkung einer vorbestehenden Insel hier am stärksten und kritischsten sein dürfte. Es zeigt sich, dass die Injektion dieser Materialmenge in die toroidale Phase des O-Punkts einer großen Insel die FS weiter verzögert und erst 1,5 Millisekunden nach der vollständigen Ablation auftritt. Dies ist ein gutes, aber unerwartetes Verhalten, welches mehr Zeit für die Verdünnung des Plasmas gibt und Zeit für zusätzliche Maßnahmen gegen die Folgen der Störung in einem mehrstufigen Mitigationsansatzes ermöglicht. Andererseits zeigen Simulationen, dass die Injektion in den X-Punkt die Plasmadynamik zusätzlich destabilisiert macht und die FS früher einsetzt. Eine geringere Menge an injiziertem Material, die in einem Plasma ohne vorbestehende Insel allein keine FS auslösen würde, treibt das Plasma in die FS, wenn in den X-Punkt injiziert wird. Diese Beobachtungen legen im Allgemeinen nahe, dass in zukünftigen Experimenten die Injektion in den Bereich des X-Punktes vermieden werden sollte. Weitere Analysen haben gezeigt, dass die durch die Injektion induzierte Stromprofilentwicklung ein relevanter Faktor für die Unterschiede im Plasmapverhalten der untersuchten Fälle sein könnte. Je näher die Injektion an den X-Punkt (oder O-Punkt) heranrückt, desto mehr ändert das Profil seine Form in einer Weise, die die 2/1-magnetische Insel destabilisiert (oder stabilisiert). Alle untersuchten Fälle deuten darauf hin, dass die Wirkung der Insel selbst auf die Verdünnung bis zum FS-Punkt eher marginal ist, was als positive Beobachtung in Bezug auf die Mitigation von Disruptionen verstanden werden kann. Die Wirkung von Hintergrundverunreinigungen verändert die Gesamtdynamik nicht: Die verzögernde Wirkung einer Injektion in den O-Punkt ist zwar geringer, aber immer noch zu beobachten. Im Falle der Injektion in den X-Punkt haben die Hintergrundverunreinigungen nur eine sehr geringe Auswirkung. Insgesamt deuten diese Simulationen darauf hin, dass die Injektion großer Mengen von Deuterium zur Verdünnung des Plasmas zur Verringerung des Risikos der Bildung von Runaway-Elektronen auch während des Disruptionseintritts, bei welcher bereits starke MHD-Aktivität vorliegt, anwendbar sein könnte.

Important quantities and abbreviations

E_{core} Thermal energy content the core region of the plasma.

E_{tot} Thermal energy content of the total plasma.

N_{SPI} Amount of material in the pellet.

N_{core} Amount of material in the core region of the plasma.

N_{tot} Amount of material in the total plasma.

P_{Ω} Ohmic heating power.

P_{rad} Radiative cooling power.

ϕ_{O} Relative toroidal angle between the SPI-nozzle and the O-point of a pre-existing island.

$n_{Z,\text{bg}}$ Concentration of background impurities of species Z .

w_i Initial size of a pre-existing 2/1 island ($w_i = 0$: no pre-existing island).

DMS Disruption mitigation system.

FS Full stochastization.

ITER International Thermonuclear Experimental Reactor.

MHD Magneto-hydrodynamics.

MMI Massive material injection.

NI-case Case of an injection into a plasma without a pre-existing island.

OI-case Case of an injections in phase with the O-point of a pre-existing island.

RE Runaway electrons.

SPI Shattered Pellet Injection.

TQ Thermal quench.

XI-case Case of an injections in phase with the X-point of a pre-existing island.

Contents

Abstract	v
Zusammenfassung	vii
Contents	xi
1 Introduction	1
1.1 Nuclear Fusion	2
1.2 The tokamak	3
1.3 Theoretical description of a fusion plasma	5
1.4 Disruptions and their mitigation	6
1.5 Thesis outline	7
2 Background	9
2.1 Physics of disruption mitigation	9
2.1.1 The disruption onset and thermal quench	9
2.1.2 Impurities and the radiative collapse	10
2.1.3 Runaway electrons	12
2.1.4 Disruption mitigation via shattered pellet injection	13
2.2 Models for tokamak plasmas	16
2.2.1 Introduction of the magneto-hydrodynamics (MHD) equations	16
2.2.2 Plasma equilibrium in the tokamak	17
2.2.3 Stability analysis of the kink mode and tearing mode	18
2.2.4 Extension of the MHD equations	21
2.2.5 The non-linear extended MHD code JOREK	22
2.3 Scientific questions	27
3 Massive deuterium injection into an ASDEX Upgrade equilibrium	29
3.1 Simulation setup	29
3.1.1 Generation of the initial perturbation	31
3.1.2 Setup of the shattered pellet injection	32
3.2 Injection into an unperturbed plasma	33
3.2.1 Dynamics with varying amounts of injected material	33
3.2.2 Detailed analysis for 6×10^{20} atoms injected	35
3.2.3 Change of the island phase during the injection	39
3.3 Injection into the O-point of a pre-existing 2/1 magnetic island	42
3.3.1 Impact of a pre-existing island onto MHD dynamics and TQ onset	42

CONTENTS

3.3.2	Detailed analysis of the dynamics	46
3.4	Injection in different phases with respect to the island	50
3.4.1	Observed dynamics and impact onto the TQ	50
3.4.2	Mechanisms affecting the TQ time	52
4	Role of background impurities in an MHD-active ASDEX Upgrade equilibrium	59
4.1	Injections with argon impurities	60
4.1.1	No pre-existing island compared to O-point injection	60
4.1.2	Injection with different injection angles	67
4.2	The role of tungsten	70
5	Conclusion	73
	Bibliography	75
	List of Figures	87

1 Introduction

The central goal of fusion research is to establish fusion processes at rates that provide a net energy gain. However, this is a huge effort due to physical constraints and therefore, it has been a field of active research since the early fifties of last century without having produced any bit of electricity so far. The thermonuclear fusion of deuterium and tritium in a magnetic confined plasma is one of the most promising approaches. The plasma needs to be heated up to about a hundred million Kelvin to reach conditions where fusion processes are possible in a large number. A first fusion reactor of this kind, that should gain a net energy balance, is now being built in South France called ITER. The net energy balance here refers to the ratio of the gain of fusion energy and net thermal energy required for plasma heating, but not the energy balance of the whole machine, which will still be fairly negative. The magnetic configuration of ITER is based on the tokamak concept. The tokamak is, besides the stellarator, currently seen as the most promising configuration. Despite its fairly developed state, plenty of topics still remain critical research areas in the field of plasma physics. (Beyond of this, proof of concepts for fundamental R&D question that would be relevant for a power plant – like sufficient tritium breeding or conversion of fusion power to electricity – will only be faced by DEMO in the second half of this century [1]). One problem is the major disruption event: it is a sudden loss of the magnetic confinement within a fraction of a second, where the plasma at first loses its thermal energy content (thermal quench, TQ) and second, the plasma current, which is required for the magnetic confinement, breaks down (current quench, CQ). [2] A disruption does not only mean a sudden end of all fusion processes. It also has violent consequences for large machines like ITER, because it causes massive heat and mechanical loads and also the generation of relativistic electrons (runaway electrons, RE), that could cause deep melting. Although a goal of ongoing research[3] is to avoid disruptions wherever possible, a limited number of disruptions has to be expected during the operation of ITER, and it is unclear if they can be fully avoidable *or* tolerable in tokamak-based power-plant (This motivates to follow alternative paths to fusion, which some people find more promising [4]). Those unavoidable disruptions need to be mitigated in their consequences. The disruption mitigation system selected for ITER is based on the strategy of massive material injection via shattered pellet injection (SPI). The effective application of material injection during a disruptive scenario may help to modify the time scales of the disruption, helps to decrease the thermal and mechanical loads, and also helps to mitigate or even avoid runaway electrons. To determine the exact schemes how the mitigation system – with many degrees of freedom for larger number of individual injectors – should be applied, dedicated experimental and theoretical work is still needed. Before ITER goes into operation by the end of this decade, research is conducted at smaller, but existing machines like ASDEX Upgrade. The aim of these

1 Introduction

studies is to understand the fundamental physics and later on extrapolate to the scale of ITER. Numerical simulations play an essential role in this process. These predictions help to prepare for ITER's operation in the best possible way.

The present project deals with the theoretical understanding of deuterium shattered pellet injection into a plasma during a disruption onset. Deuterium injection could help to increase the plasma density prior to the TQ, helping to prevent runaway electrons, as one step of a multi-stage mitigation system. During the disruption onset, the plasma often forms a precursor in the form of a non-rotating neoclassical tearing mode (NTM). The understanding of the interaction of this precursor NTM and deuterium injection is not well known yet. Therefore, in this thesis, a comprehensive numerical modelling effort is conducted based on plasma equilibria of the ASDEX Upgrade tokamak. Relevant dynamics and the underlying processes are studied by varying plasma and injection parameters.

In the following sections of this introduction, the fundamental physics of magnetic confinement fusion and disruptions are discussed.

1.1 Nuclear Fusion

The binding energy per nucleon within an atomic nucleus is a function of its number of neutrons and protons. It is largest for ^{56}Fe and drops substantially for lighter or heavier elements. As a consequence, the fusion of lighter elements or the fission of heavier elements will lead to a release of energy, that is equal to the difference between the sum of the binding energies of the "fuel" nuclei and the reaction products. As an example, the fusion reaction between deuterium and tritium is given by:



According to classical momentum conservation, the gained energy is distributed as kinetic energy between the helium and the neutron. The probability for a fusion reaction – quantified by the energy dependent nuclear cross-section σ – during a single collision of a pair of deuterium and tritium nuclei is generally very small, as they need to get very close to overcome the Coulomb barriers, which is only possible by quantum tunneling for relative kinetic energies of even $\lesssim 400 \text{ keV}$ – a hardly realizable energy. A sufficient number of reactions per time, i.e., a sufficient large fusion power, is therefore only possible with a very high collision frequency. This can be conducted by bringing the fusion material into a thermal equilibrium at a large temperature, called thermonuclear fusion. The frequency of reactions per volume is then given by

$$f_{\text{fus}} = n_D n_T \langle v\sigma \rangle, \quad (1.1.2)$$

where the reactivity $\langle v\sigma \rangle$ is averaged over the thermal distribution and the densities of tritium and deuterium are denoted as n_T and n_D . The reactivity reaches a maximum at a temperature of about $T = 10 \text{ keV}$, which is the approximately targeted temperature for ITER operation. At such temperature, the fusion fuel is fully ionized and constitutes

a plasma state, which is advantageous: the fuel is electrically charged and interacts with magnetic field lines. For this reason, the approach of magnetic confined fusion has been developed, in which the fuel is confined by a dedicated field line configuration and heated up to a point, where fusion reactions set in. As produced helium ions are also confined within the plasma, they will support the further heat supply of the plasma by “helium heating”. The neutrons, however, leave the plasma and its energy could be harvested.

If the fusion power is large enough that helium heating is almost or fully sufficient for maintaining the plasma temperature, it is referred to as a “burning plasma”. More details of fundamental plasma physics would be out of the scope of this overview, however, and are discussed for example in [5]. The next section briefly discusses the plasma confinement configuration of the tokamak, which is the base for experiments like ASDEX Upgrade or ITER.

1.2 The tokamak

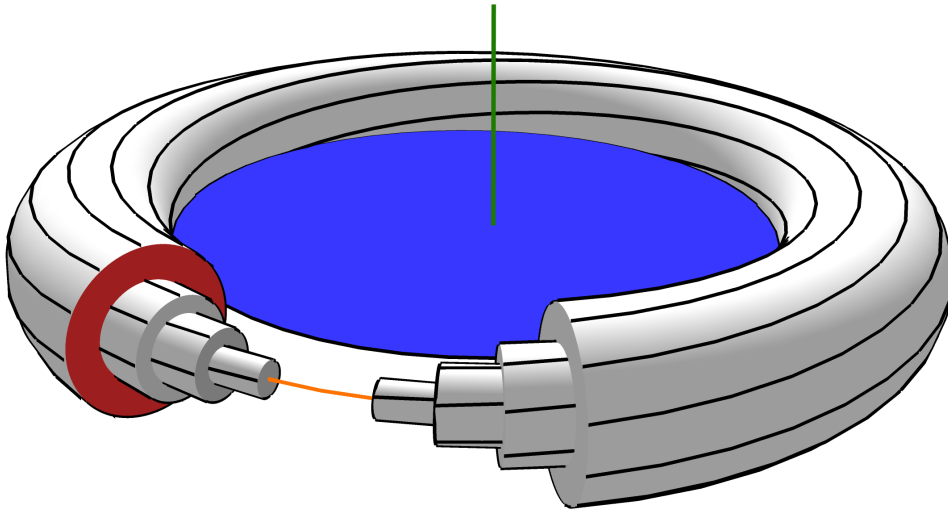


Figure 1.1: Schematic sketch of flux surfaces within a tokamak. Black lines represent the helical field lines on some flux surfaces (white). The poloidal flux Ψ of the outermost flux surface is defined as the flux going through the blue area S_p , while the toroidal flux Φ is defined by the red area S_t . The magnetic axis is marked in orange. The central solenoid lies close to the torus axis (green). Figure excerpted from [6].

In a magnetized plasma, the motion of particles perpendicular to magnetic field lines is restricted, which is the basic property of plasma confinement. In a homogeneous field, ions and electrons would rotate with the gyroradius in the plane perpendicular to field lines, but can move freely in the parallel direction. The parallel mobility can be restricted in a toroidal arrangement of the field lines. However, a configuration of a purely toroidal field B_{tor} would not lead to confinement: as a result of the divergence-

1 Introduction

freeness, $\nabla \cdot \vec{B}_{\text{tor}} = 0$, the field strength decreases radially by $B_{\text{tor}} \propto 1/R$. This causes plasma drifts, which eventually prevent a stable confinement. By an additional poloidal field component B_{pol} , the confinement in a toroidal arrangement becomes possible. The toroidal field component can be generated by magnetic field coils. In a tokamak, the poloidal field component is generated by a toroidal plasma current. Classically, this current is generated by induction, where the plasma acts as a secondary coil with only one winding of a large transformer. This is the basic concept of the tokamak. Experimental studies have shown, that parts or possibly the full toroidal current could also be produced by neoclassical effects and other current drive techniques [7]. The generation of the poloidal field by 3D-coils instead of a toroidal current is the concept of the alternative stellarator configuration. Today's tokamaks also take advantage of plasma shaping, where the originally circular cross-section of the plasma is being formed into a "D-shape". This improves the plasma performance for different reasons [8]. The lower (sometimes also the upper) region of the plasma touches the tokamak vessel in the divertor region.

The field lines in the tokamak are helical and form flux surfaces. Everywhere on a flux surface, $\vec{n}_f \cdot \vec{B} = 0$ holds, with the flux surface normal \vec{n}_f and $\vec{B} = \vec{B}_{\text{tor}} + \vec{B}_{\text{pol}}$. In a shaped plasma, the plasma is divided into closed flux surfaces and open flux surfaces, that touch the divertor region, by the separatrix. The plasma shaping leads to an X-point close to the divertor region, at which the poloidal field has zero magnitude.

Each flux surface is associated with the toroidal flux $\Phi = \int_{S_t} \vec{B} \cdot \vec{n}_{S_t} dS$, where S_t is the toroidal area encapsulated by a regarding flux surface. Similarly, the poloidal flux is defined by $\Psi = \int_{S_p} \vec{B} \cdot \vec{n}_{S_p} dS$ (see Fig. 1.1). In the tokamak, Ψ changes monotonically with the radial position of the corresponding flux surface, from the magnetic axis value Ψ_{axis} to the value at the last closed flux surface Ψ_{bnd} . From this, the normalized flux Ψ_N is defined by

$$\Psi_N = \frac{\Psi - \Psi_{\text{axis}}}{\Psi_{\text{bnd}} - \Psi_{\text{axis}}}. \quad (1.2.1)$$

and often used as a radial coordinate in a flux surface aligned coordinate system. The safety factor $q(\Psi_N)$ is the ratio of the number of toroidal turns of a field line per poloidal turns and can be defined by

$$q = \frac{d\Phi}{d\Psi}. \quad (1.2.2)$$

If the safety factor becomes a rational number $q = m/n$ (with m referred to as the poloidal number and

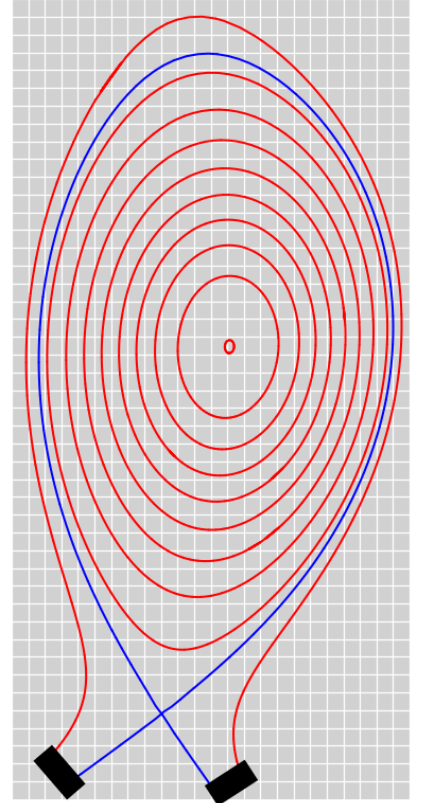


Figure 1.2: Poloidal cross-section of flux surfaces of a plasma in divertor configuration. The plasma is divided by the separatrix (blue) into the inner region of closed magnetic field lines and the outer region of open field lines. Field lines outside the separatrix hit the divertor plates (black). Figure excerpted from [6].

n the toroidal number), the corresponding flux surface is called a resonant surface and the magnetic field lines close in themselves. The character of the q -profile is an important feature of every tokamak, as it defines its stability to certain modes. This is discussed in more detail in Subsections 2.1.1 and 2.2.3. More general information about the tokamak configuration can be found in [9].

For the theoretical description of the tokamak (and a plasma in general) several models have been developed, which can be selected regarding the aimed application. A short overview is given in the next section.

1.3 Theoretical description of a fusion plasma

A magnetized plasma represents a many-body problem, that can only be described after large simplifications. The selection of the proper model relies heavily on the spacial and time scales, being investigated. The kinetic model is the most detailed statistical model, which averages over very small volumes (i.e., Debye-spheres) and assigns each plasma species α (i.e., electrons and ions) to distribution functions $f_\alpha(x, v, t)$ in the six-dimensional phase space. These f_α are being evolved according to the interaction among particles itself and with the electromagnetic fields. Due to its complexity, the kinetics model is very costly to solve. Only small regions of the plasma or small-time intervals in the order of $1 \mu\text{s}$ can be investigated with a realistic effort. It is required to describe localized processes like collisions or scattering or allows to precisely determine local transport coefficients. Further simplifications are made, to enable the description of the full plasma volume. In the fluid approach, we assume f_α to be Maxwellian, which justifies to describe the plasma as multiple or even only one fluid. Hence, the plasma can be described by the magneto-hydrodynamic (MHD) equations. They are basically derived from the coupling of hydrodynamic and Maxwell equations under some further assumption. Large scale magnetic instabilities like tearing modes, kink modes or vertical displacement events can be investigated properly by the MHD approach. Total momentum, thermal or magnetic energies of the plasma can be treated and local parameters like plasma density n or Temperature T are introduced.

In hybrid codes, both the kinetic and the fluid approach are coupled, which becomes necessary for some application. This allows for example the simulation of magnetic instabilities under the realistic evolution of transport coefficient, as well as the treatment of neutral kinetic particles in the presence of the plasma fluid. For charged particles, nearly always gyrokinetic models are in use, which basically reduce the phase space of the kinetic description to five dimensions by averaging over the microscopic gyromotions.

The MHD framework plays an important role for the modelling of disruptions, and also this work is based on that: global instabilities are a prominent cause and result of disruption events. The next section gives an overview of the disruption.

1.4 Disruptions and their mitigation

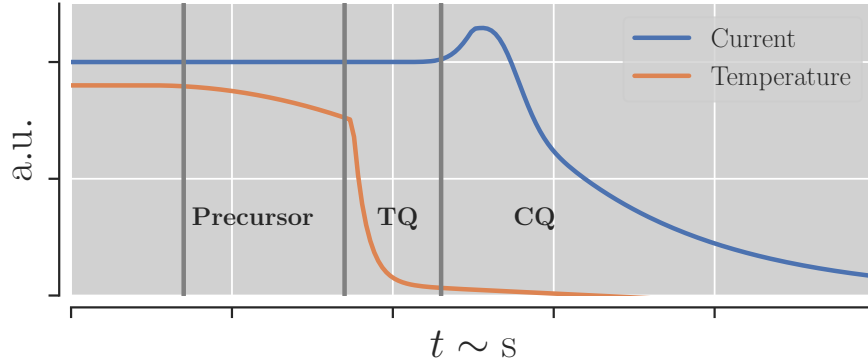


Figure 1.3: Schematic sequence of events during a disruption.

The major disruption is a sudden, complete loss of the magnetic confinement. The sequence of a disruption and its time scales can differ greatly, depending on the type of mechanisms involved or the machine size. Yet, it typically consists of three phases (see Fig. 1.3): in the precursor phase, first perturbations of various kinds occur. The cause of these perturbations is usually a complex pattern of events, including physical instabilities and control errors. It can last up to a few hundred milliseconds. Second, the thermal quench (TQ) sets in, when the perturbation amplitudes reach a certain level. During the thermal quench, the thermal energy drops and the temperature reduces by several orders of magnitude. At these low temperatures, radiative losses due to impurities play a key role, which further reduce the plasma temperature to just a few eV eventually. Due to the low temperatures, the resistivity rapidly increases due to its dependency $\eta \propto T^{-3/2}$. This is referred to as the current quench (CQ). Besides major disruptions, sometimes minor disruptions occur, which do not go through the full course as described above. In these cases, it may still be possible to turn the plasma back into a stable state.

A disruption would not only mean a sudden stop of fusion energy generation. They have already violent consequences on present machines. First, the sudden loss of thermal energy leads to massive heat loads which strain plasma facing components. These thermal energies have the capability to even melt materials within the vacuum vessel. Second, during the loss of the plasma current, an elongated plasma becomes vertically unstable. As a result of the occurring vertical displacement event (VDE), halo and eddy currents are induced into the vacuum vessel, which leads to strong Lorentz forces. These mechanical loads must be absorbed by the supporting structures of the machine. Third, as a consequence of the increasing toroidal electric field due to increased η , the generation of runaway electrons, especially in larger machines, becomes an additional threat. When colliding with the first wall, the runaway electrons cause serious damage, that makes costly replacement of wall tiles necessary. The severity of a disruption increases with machine size: for ITER, estimates calculate heat loads on the divertor components of 10 GW/m^2 (enough to melt or sublimate the materials) or a conversion of 70% of the

initial plasma current $I_p = 15\text{MA}$ into REs. [10, p. 128 - 202]. Therefore, disruptions pose a major threat to ITER that could potentially destroy the entire machine.

Because of this relevance, disruption have gained a growing interest in recent years. It is not certain that, even if the understanding grows, disruptions could be fully avoided in the future. Hence, for ITER – and possibly future fusion experiments – mitigation systems are necessary as a last line of defense. In case of a non-avoidable disruption, the aim is to mitigate its consequences. The main approach for the disruption mitigation scheme (DMS) is in the form of massive material injection (MMI). By injecting amounts of material in the order of the plasma content, the plasma gets diluted and – in case of impurity material injection – cooled down by radiative losses. Thereby, all three violent consequences of a disruption might be reduced. For ITER, the DMS will be realized by shattered pellet injection (SPI). The design of a robust and thoroughly validated DMS remains one of the outstanding challenges for ITER [11] and motivation for this work.

1.5 Thesis outline

The rest of the thesis is structured as follows: in Chapter 2, the theoretical background necessary for the theoretical disruption mitigation studies considered in this work are discussed. At first, physical backgrounds of the disruption onset and disruption mitigation are shown in more detail in Section 2.1. The modelling of tokamak plasmas is discussed in Section 2.2, including a description of the applied code JOREK. From this, the open scientific questions covered in this work are motivated in Section 2.3. The central Chapter 3 of this thesis presents the results of a large set of simulations for an ASDEX Upgrade equilibrium. Scans of different mitigation and plasma parameters are described and discussed here in detail. The simulations are extended to take the effect of background impurities into account, which is shown in Chapter 4. The work is concluded by Chapter 5.

2 Background

2.1 Physics of disruption mitigation

2.1.1 The disruption onset and thermal quench

Neoclassical Tearing Modes The exact roots of disruptions are often a complex chain of events and include system errors as well as plasma phenomena. However, experimental studies in JET[12], DIII-D[13] or ASDEX Upgrade[14] and simulations[15] of disruptions have shown, that the $m = 2/n = 1$ neoclassical tearing mode often plays a crucial role in the final phase of the disruption onset. It is also expected, that in unavoidable disruptions in ITER, the 2/1 neoclassical tearing mode will become relevant[16], [17, Fig.2]. A m/n tearing mode is a magnetic instability arising due to the current gradient at a corresponding rational surface, involving magnetic reconnection at finite resistivity. The tearing mode results in a modification of the magnetic topology in the vicinity of the rational surface by forming magnetic islands. A helical current perturbation at the rational surface is an important feature of the tearing mode. The linear theory of the *classical* tearing mode is described in Subsection 2.2.3. Due to enhanced radial heat conductivity, the temperature, and pressure profiles flatten within the island. This leads to a decrease of the neoclassical bootstrap current within the island. As a result, this effective helical current perturbation amplifies the island. Even if a plasma equilibrium is classically stable against the 2/1 tearing mode, a seeding mode, triggered by other effects may appear, which then grows by this neoclassical drive. The theory of *neoclassical* tearing modes (NTM) is further explained in Subsection 2.2.4. A tearing mode couples with other rational surfaces and therefore triggers the growth of further islands at different radial locations: by linear coupling, modes of the same toroidal mode number $n = 1$ and larger m are then growing with the same growth rates as the primary mode. Due to non-linear terms, modes with larger n may couple and grow with larger rates compared to the primary mode. [18, 19]

Mode locking In normal operation, the tokamak plasma rotates. The rotation is caused on one hand intrinsically due to the diamagnetic drift as well as the neoclassical E-cross-B drift[20, 21]. It is to note that both drifts are $\propto \nabla p$, which implies that a large island can reduce both drift effects. On the other hand, the torque by neutral beam injection drives the rotation externally. TMs typically rotate with frequencies of ~ 10 kHz[22, 23], which has a stabilizing effect onto the mode and can prevent coupling to other rational surfaces due to rotation shear[24, 25]. If a tearing mode grows in a rotating plasma, the time varying magnetic perturbation will induce eddy currents in the vacuum vessel as well as in conducting structures inside. As these helical currents and magnetic fields

2 Background

are not completely in phase, $j \times B$ forces occur, that eventually leads to momentum transfer between plasma and machine. Plasma rotation drops eventually to zero, which is referred to as mode locking. Also, error fields, e.g., by coils, play an important role in this process[26]. The acting forces are highly dependent on rotational frequency and wall resistivity. The break-down of mode rotation enhances mode coupling to other rational surfaces and eventually overlapping of neighboring islands.

Stochastization is a crucial effect during the disruption onset, it is loosely speaking a chaotic behavior of magnetic field lines, where flux surfaces are non-existing and the radial transport is heavily increased (by parallel transport along the chaotic field having a radial component). As a result, in a stochastic region the temperature profile becomes flattened and in case of a fully stochastic plasma, the confinement is lost. [27] If magnetic islands on two neighboring rational surfaces overlap, they produce a stochastic layer. This feature is described by the Chirikov-criterion[28]. In case of a highly perturbed plasma, where many modes are excited and overlap, this leads to large regions of stochastization.

Thermal quench Because of stochastization, plasma confinement is massively deteriorated, and both the radial heat and particle transport increase. As a consequence, the temperature of the whole plasma collapses to low values of the order of 100 eV. It may take up to a few hundred milliseconds in large machines from the appearance of first rotating modes to the thermal quench onset. The thermal quench itself takes about one ms. In the last stage of the thermal quench, background impurities become relevant, which is described in the next Subsection 2.1.2. The disruption proceeds with the current quench as introduced in Section 1.4.

2.1.2 Impurities and the radiative collapse

The plasma in a magnetic confinement experiment can never exclusively consist of hydrogen or helium isotopes, but will always exhibit traces of heavier species, the so-called impurities. They originate from the fact, that the vacuum in the vessel is never perfect and also, that first-wall materials elements will erode to some extent. [29] Consequently, typical impurities are nitrogen or tungsten. These impurities are often referred to as background impurities to distinguish from those high-Z materials that are artificially shot into the vessel in a much larger amount (for improving the performance[30], or disruption mitigation (see Subsection 2.1.4)).

As some of these materials do not get fully ionized at typical plasma core temperatures, atomic physics play a crucial role. This is discussed for example in [31]. The full evolution of ionization states are not modelled in this work, and only the calculation of radiative losses in the coronal equilibrium assumption are of interest.

Radiative losses Radiative losses, i.e., effectively the conversion of thermal energy into radiation in the range of visible light up to X-rays, arise from three mechanism:

- **Line radiation** An excited ion falls back into its ground state or at least a lower energy state without changing the charge state of the ion. The discrete energy of this transition is emitted in the form of a photon.
- **Line radiation from recombination** A free electron is captured by an ion, recombines and the ion or atom is usually in an excited state. Similarly to the mechanism above, line radiation is emitted, but the ion has changed its charge state.
- **Bremsstrahlung** Free electrons become accelerated when passing the Coulomb field of an ion closely. This results in the emission of Bremsstrahlung. This radiation is still present in a very hot plasma with fully ionized impurities.

Also, for the hydrogen isotopes of the background plasma, these effects exist. The radiative losses of hydrogen are very small compared to the losses due to impurities. They are quantified by radiation coefficients, L_{rad} which are derived from proper models like the collisional-radiative model and fundamental empirical data. For fusion plasmas, these coefficients are strongly dependent on the plasma temperature and weakly dependent on the plasma density. Regarding the complexity of the model, coefficients for all metastable states of every charge state, one coefficient for each charge state only, or even only one coefficient for the whole impurity population are of interest. The latter case implies the assumption, that the charge state distribution is in an equilibrium state. Impurities in a plasma approach an equilibrium after a few ms, if T_e and n_e are constant in time. [32] As the radiated power P_{rad} is also proportional to background and electron density, the coefficients are given in units of W/m^3 . For example, the line radiation of the i -th charge state is then given by:

$$P_{\text{line},i} = L_{\text{line},i}(T_e, n_e)n_{\text{imp},i}n_e, \quad (2.1.1)$$

where n_{imp} is the total impurity density and $0 < f_i < 1$ is the fraction of impurities in the i -th charge state.

Radiative collapse Background or injected impurities play an important role during a disruption: when temperatures have dropped to ~ 100 eV during the TQ, diffusive transport from stochastic field lines becomes too inefficient for further plasma cooling[33]. In a “complete” thermal quench, which we define here as a case where the electron temperature flattens at a few eV, radiative cooling plays a key role. As it can be seen from Fig. 2.7, radiative losses by impurities like argon or neon only become maximal at temperature below 100 eV. Consequently, an already cooled down plasma might run into a runaway effect, where it is pushed to even lower temperatures now dominantly due to radiative losses. [34] This is referred to as the radiative collapse. A counteracting mechanisms however comes from Ohmic heating, which is temperature dependent by $\propto T^{-3/2}$ and becomes significant at temperatures below 100 eV as well. Both effects might equilibrate after some time, and the plasma temperature reaches a steady state. As $P_{\text{rad}} \propto n_{\text{imp}}$, the occurrence of a thermal collapse is dependent on the impurity

2 Background

concentration. The timescale for this radiative collapse can roughly be approximated as (with Euler number e and $k_B = 1$) [35]:

$$\tau_{RC} \approx \frac{eT_e}{L_{rad}n_{imp}}, \quad (2.1.2)$$

when ignoring Ohmic heating. For too small n_{imp} , τ_{RC} becomes very large. Hence, the collapse does not happen during the usual timescale of a disruption. As a second effect of a too small value of n_{imp} , Ohmic heating will dominate, preventing the collapse all together. From that, it follows that it needs to exceed a certain threshold to trigger the radiative collapse.

2.1.3 Runaway electrons

As introduced in Section 1.4, disruptions are a major concern, due to the three consequences: heat loads, mechanical loads and runaway electrons. The phenomenon of runaway electrons is discussed here further, as its mitigation is a primary motivation for the disruption mitigation addressed in this work. Runaway electrons (RE) are a fraction of the free electrons in the plasma, for which the kinetic energy continuously increases, as the accelerating forces due to the toroidal electric field exceed the decelerating friction forces. By this, REs can reach relativistic energies. When a beam of such relativistic electrons leaves the plasma and hits the wall, severe damage is possible. [36] If a RE beam destroys cooling structures within the vessel, the machine could even run into a loss-of-coolant-accident. [37]

During a disruption a strong toroidal electric field E is generated, caused by the increased plasma resistivity due to the TQ, while the plasma current is still high. The friction force however is highly energy dependent with a peak around the thermal electron velocity. For larger energies, it rapidly reduces [36, Figure 1][38]. Four primary sources for runaway electron *seeds* are known: common in Fusion experiments is seeding by the Dreicer effect, as well as the hot tail generation. While the Dreicer effect is rather negligible, the hot tail mechanism plays an important role in a fast thermal quench: if the temperature drops faster than the timescale for electron thermalization, a small fraction of electrons may remain at larger temperatures, i.e., it establishes a “tail” in the velocity distribution. As only small friction forces act onto the tail, it easily converts to runaway electrons. Two additional seeds for RE, which only become relevant in the radioactive phase of a plasma experiment, are electrons from tritium decay and Compton scattering, triggered by the gamma emissions of the activated walls.

Secondarily, these RE seeds may trigger electron avalanches, when they collide with slower electrons and push them to larger velocities. Due to the avalanche effect, even small seeds can produce a large beam RE eventually. In large machines like ITER, the avalanche is much more violent than in present devices.

The critical electric field strength for RE generation is dependent on the plasma density by $E_c \propto n_e \ln \lambda / T_e$ with the Coulomb Logarithm $\ln \lambda$. Consequently, an increase of n_e could mitigate the generation of REs. Avoiding any avalanche could only be achieved

at the Rosenbluth density [10], which is two order of magnitudes larger than the plasma density.

2.1.4 Disruption mitigation via shattered pellet injection

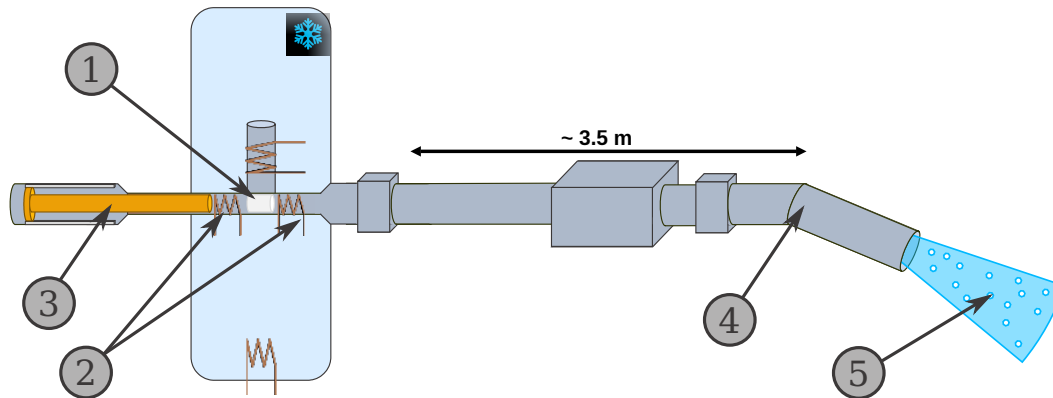


Figure 2.1: Basic procedure of an injection: in the cooling chamber, a pellet is formed by gas condensation (1). The pellet's form is controlled by several barrel heaters, which acts in different ways during and after the pellet formation (2). Using a propellant gas, the pellet is pushed at a speed in the order of hundreds of m/s into the pipe towards the plasma (right direction) (3). The tube has a miter bend in the end, so that the pellet crashes and shatters (4). The shards are injected through the nozzle into the plasma (5). Graphic adopted with courtesy of Paul Heinrich.

Research on disruption mitigation has been an important field over the last twenty years. Mitigation through the injection of material into the plasma seems to be the most promising approach[39]. The injected material acts in different ways on the plasma:

- The injected material dilutes the plasma. This leads to an adiabatic cooling and an increase of the plasma density. As RE beam generation is more likely at lower densities (see Subsection 2.1.3), dilution is advantageous for RE mitigation.
- When the injected material gets heated, it becomes radiating. This is rather negligible for pure hydrogen pellets. However, these radiative losses – mostly driven by line radiation – are significant, if heavier elements are injected (see Subsection 2.1.2 and Fig. 2.7). Neon or argon are usually considered for this[40]. The impurity radiation is isotropic and decreases the thermal energy content of the plasma, which reduced localized heat loads of a disruption.
- The post-thermal quench temperatures of the plasma determine the time scales of the current quench, which eventually determines the nature of mechanical loads on the machine by the amplitude of halo and eddy currents. Hence, the material

2 Background

injection can indirectly mitigate mechanical stresses by achieving the optimal current quench time, for which the mechanical stress and additional issues like arcing gets minimized. [41]

Efficient massive material injection (MMI) is the subject of continued research. The most straightforward way to deliver MMI is via direct gas injection with in- or ex-vessel valves, referred to as massive gas injection (MGI). MGI has been employed on numerous tokamaks both for machine protection and as disruption mitigation actuators for research[42]. However, it still appears to have limited penetration properties, which scale unfavorable with machine size[43]. This may lead to insufficient material assimilation in the core region, making it prone to the generation of RE currents. Another extreme case is to inject the material as one single pellet, which ablates while travelling through the plasma. Although it has good penetration properties, the amount of material that can be effectively ablated would be far too small, in that case. A large pellet would even crash onto the vessel at the opposite side of injection and potentially damage it. Because of this, the approach of *shattered* pellet injection is now being developed. Here, the pellet is broken intentionally by colliding with a shatter unit before entering the plasma. The shattering is a probabilistic process. A schematic picture of a full SPI system is given in Fig. 2.1. Experimental work is or has been carried out at different machines [44, 45, 46] as well as in theoretical work [47, 32, 35, 48].

SPI systems can exhibit several degrees of freedom, e.g. the size of the pellet, its injection velocity, its composition, the injection and shattering angles. For the different mitigation goals, specific configurations are needed, and it has emerged from recent studies, to apply staggered mitigation schemes [35, 49]:

1. First, a pure deuterium injection dilutes the plasma, but is not targeted to trigger the thermal quench yet. It has been shown theoretically for ITER, that this might be possible without immediately triggering MHD activity, i.e., not affecting the time point of the TQ. Generation of a hot tail could be avoided hereby.
2. After that, the diluted plasma still exhibits a large fraction of its original thermal energy content. SPI is triggered for a second time, using impurity and/or mixed pellets to radiate the plasma thermal energy by provoking a radiative collapse. As the plasma density is already large due to the primary injection, RE generation is reduced.
3. Further stages of disruption mitigation, for example during the post-thermal quench phase, are conceivable. [50].

Furthermore, in some experiments, it is intended to inject the material not only from the valve, but from multiple – toroidal, as well as poloidal – positions. By this, the material can be distributed more uniformly. In case of impurity SPI, radiation asymmetries are reduced. In ITER, a complex SPI system will be installed with multiple injectors. [51] The optimization of disruption mitigation strategies via SPI stays a very important field and to this point, it cannot be guaranteed, that sufficient mitigation just

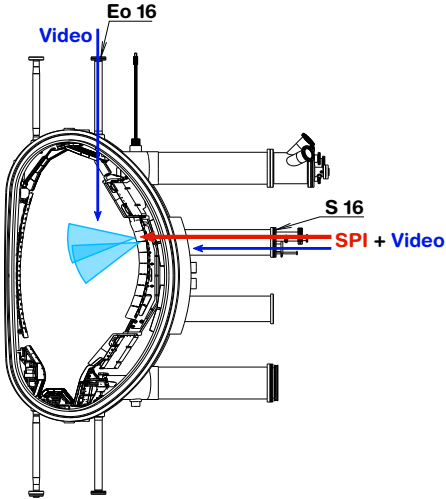


Figure 2.2: Poloidal cut of the ASDEX Upgrade vessel. The injector is located in Port S16. The shatter bends are about 35 cm and 39 cm above the midplane, with the aim to shoot at the axis.

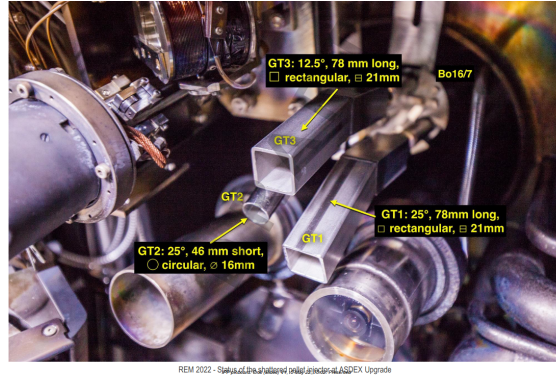


Figure 2.3: Shatter head configuration in the 2022 SPI campaign inside the vacuum vessel. Rectangular and circular shatter plates with different angles are mounted. Graphic and picture adopted with courtesy from Gergely Papp.

via SPI is possible in a fusion power plant: during nuclear operation, additional RE seeds from tritium decay and from Compton scattering (triggered from the highly radioactive [52] walls) will possibly become too aggressive for a treatment with MMI. [49] Also, impurity SPI – required for controlling thermal loads – makes the plasma more prone to REs, as the large number of bound electrons of the injected impurities will lower the critical electric field E_c . [53]

The ASDEX Upgrade SPI system In light of grown interest on research and development for the ITER DMS, also ASDEX Upgrade has been equipped with an SPI in 2021. [54, 55] The uniqueness of this system is reflected in the option to vary many parameters, in particular of the shattering angle. SPIs of other tokamaks have typically just one angle. The goal is to try a large variety of pallet compositions, sizes, and shatter spray distributions (both for size and speed). The system consists of three independent barrels. The pellet can be made of deuterium, neon, or a mixture of both. Different pellet diameters between 1 mm to 8 mm are possible, where lengths up to ~ 11 mm have been realized in laboratory tests. It has been shown that the pellets can be accelerated to velocities between 60 m/s to 750 m/s, where the exact range depends on the pellet mass. Each barrel can be equipped with different nozzles with varying shattering angles and cross-sections. For the 2022 SPI campaign, angles of 0° i.e., no explicit shattering

2 Background

at all, 12.5° and 25° and rectangular and circular cross-sections were used in the final configuration.

2.2 Models for tokamak plasmas

As introduced in Section 1.3, several approaches for the description of fusion plasmas have been established. The physics and control of disruptions are highly related to magneto-hydrodynamics (MHD), as their features (global magnetic modes, stochastization, thermal and current quench) are covered by these models. In the past, only the modelling of the fundamental instabilities in simplified geometries were possible. [15] Thanks to the rapid development of high performance computing, extensive simulations of realistic plasma configurations became an important tool to studying disruptions. The basic MHD equations are shown in the following, and the MHD description of some relevant instabilities is shortly discussed.

2.2.1 Introduction of the magneto-hydrodynamics (MHD) equations

The one-fluid viscoresistive MHD equations can be derived from the Fokker-Planck equation, which is the fundamental equation of motion in the kinetic picture:

$$\frac{\partial f_\alpha}{\partial t} + v \cdot \nabla_x f_\alpha + \frac{q_\alpha}{m_\alpha} (E + v \times B) \cdot \nabla_v f_\alpha = \left(\frac{\partial f_\alpha}{\partial t} \right)_{\text{coll}}. \quad (2.2.1)$$

Assuming a thermodynamic equilibrium, f_α becomes (nearly) Maxwellian and the moments of the distribution function can be defined: density n_α , fluid velocity u_α and pressure $p_\alpha = n_\alpha T_\alpha$. Having ions i and electrons e as the only species, two-fluid MHD equations are derived. These can be reduced to the single fluid MHD equations with the definitions and approximations: $\rho = m_i n_i + m_e n_e \approx m_i n_i$, $n = n_e \approx n_i$, $v = \frac{1}{\rho} (n_i m_i u_i + n_e m_e u_e) \approx u_i$ and $j = en_i u_i - en_e u_e = en(u_i - u_e)$. They are listed below:

- The continuity equation:

$$\frac{\partial \rho}{\partial t} - \nabla \cdot (\rho v) = 0. \quad (2.2.2)$$

- The velocity equation with viscosity μ :

$$\rho \frac{\partial v}{\partial t} = -\rho v \cdot \nabla v - \nabla p + j \times B + \nabla \cdot (\mu \nabla v). \quad (2.2.3)$$

- The energy equation:

$$\frac{\partial p}{\partial t} = -v \cdot \nabla p + \gamma p \nabla \cdot v - \nabla q. \quad (2.2.4)$$

Here the Braginskii closure [56] is applied with the ratio of specific heat $\gamma = 5/3$ and the heat flux $q = \kappa \nabla T$.

- The Ohm's law with resistivity η :

$$E = -v \times B + \eta j. \quad (2.2.5)$$

- And the Maxwell equations:

$$\frac{\partial B}{\partial t} = -\nabla \times E, \quad (2.2.6)$$

$$\nabla \times B = j, \quad (2.2.7)$$

$$\nabla \cdot B = 0. \quad (2.2.8)$$

In the approximation of a non-resistive plasma, $\eta = 0$ and $\mu = 0$, the problem can be described by the ideal MHD equations. However, resistive effects play a crucial role during disruptions. The shown MHD model could be extended by including two-fluid effects. For example, introducing dedicated temperatures for electrons and ions, T_e, T_i , would lead to one type of extended MHD equations. Temperature differences between electrons and ions might become relevant in simulations of the full current quench, which is however out of the scope of this work.

2.2.2 Plasma equilibrium in the tokamak

After unsuccessful approaches of confining a plasma in Pinch configurations, the tokamak configuration established, which allows stable plasma equilibria. [57] In the model of ideal MHD, an equilibrium state requires a compensation of the pressure gradient by Lorentz forces,

$$\nabla p = j \times B, \quad (2.2.9)$$

which is equivalent to Eq. 2.2.3 with $v = 0$. The plasma equilibrium in a two-dimensional configuration like the tokamak has been derived from that independently by Grad and Rubin in 1958[58], as well as by Shafranov in 1966[59], which is given in its most general form by

$$\Delta^* \Psi = -R^2 \frac{dp}{d\psi} - F \frac{dF}{d\psi} \quad (2.2.10)$$

with the radial, flux aligned coordinate ψ , the Grad-Shafranov operator is used $\Delta^* \Psi = R^2 \nabla \cdot \left(\frac{\nabla \psi}{R^2} \right)$, and the toroidal and poloidal field components by B are separately determined by scalar functions ψ and $F(\psi)$:

$$B_\phi = F(\psi) \nabla \phi, \quad B_\psi = \nabla \psi \times \nabla \phi, \quad (2.2.11)$$

with the toroidal coordinate ϕ .

The equation only describes a classical hot thermal, and it is still a fundamental equation in today's tokamak research. When a large fraction of the plasma current is carried by REs (i.e., during a disruption), the application of Eq. 2.2.10 becomes

2 Background

potentially invalid and more extensive descriptions might be necessary [60, 61]. The magnetic confinement is often quantified by the value of the plasma-beta,

$$\beta = \frac{p}{B^2/2\mu_0}, \quad (2.2.12)$$

which is the ratio of the plasma pressure and the magnetic pressure $p_{\text{mag}} = \frac{B^2}{2\mu_0}$. In case of a fusion plasma, a large β is preferable, because the fusion rates scale with p^2 and the energy demand for the magnets scale with p_{mag}^2 . The maximal achievable β is limited by plasma instabilities, however. [62]

L-mode and H-mode The pressure profile $p(\psi)$ is one degree of freedom of Eq. 2.2.11. In the L-mode or low-confinement mode, the plasma exhibits a pressure profile that is steadily increasing from the plasma edge towards the core. It has been the usual operation mode up to the 80s, until the high-confinement (H-mode) was discovered in ASDEX [63]. Its feature is a strong increase of the pressure in the edge region known as the pedestal. In the H-mode, conditions for fusion are favorable compared to L-mode due to increased confinement and is the foreseen operational regime for ITER. In case of a disruption, the plasma usually undergoes an H to L transition early due to confinement losses at the edge. [64] Because of this, in this study, only L-mode equilibria are considered.

2.2.3 Stability analysis of the kink mode and tearing mode

The analysis of the Grad-Shafranov equation can not clarify the stability of a magnetic configuration. It can be investigated however by an energy principle, i.e., a variational formalism in the MHD picture. [21] Roughly speaking, (linear) stability of a system is given, if it is in an equilibrium state and a little perturbation would produce a counter-acting force, that pulls the system back to the equilibrium point. However, if an arbitrary small perturbation produces a positive feed-back force, the system moves away from the equilibrium and is referred to as unstable. A system also might be meta-stable: in that case, a sufficiently large perturbation might push a system into an unstable state, while the system remains stable against every smaller perturbation. Considering the change of the potential energy δW by the system through a perturbation or Eigenfunction ξ , it holds that:

$$\delta W(\xi) < 0 : \text{unstable} \quad (2.2.13)$$

$$\delta W(\xi) > 0 : \text{stable} \quad (2.2.14)$$

In the following, only internal modes are considered, i.e., perturbations of the magnetic field within the plasma volume. For this, δW is given by [65]:

$$\delta W_{\text{plasma}} = \frac{1}{2} \int_{\text{plasma}} \frac{B_1^2}{\mu_0} - \underline{j_0 \cdot (B_1 \times \xi)} + \gamma p_0 |\nabla \cdot \xi|^2 + \underline{(\xi \cdot \nabla p_0)(\nabla \cdot \xi)} dV, \quad (2.2.15)$$

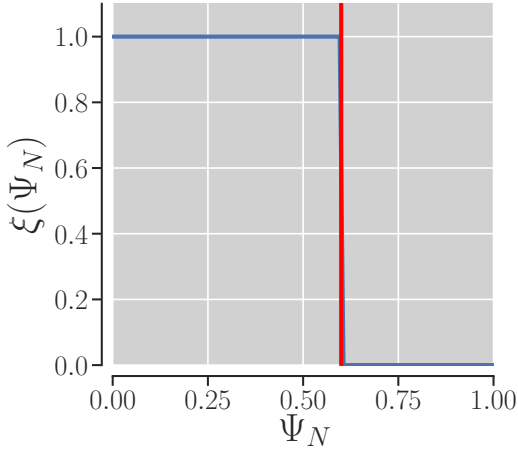


Figure 2.4: Schematic sketch of a kink mode. The Eigenfunction has a constant value inside the rational surface (at $\Psi_N = 0.6$) and drops to zero outside.

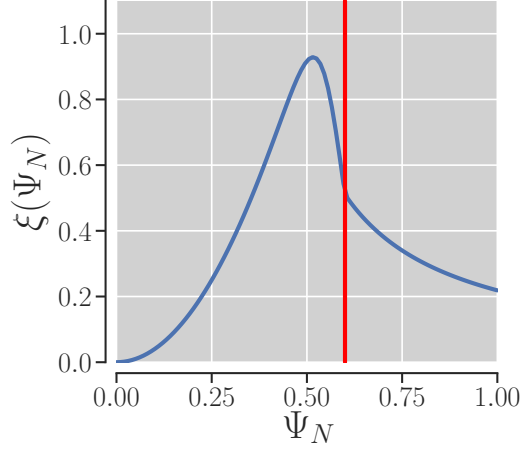


Figure 2.5: Schematic sketch of a tearing mode. A discontinuity of the first derivation at the radial position of the corresponding rational surface is an important property. The Eigenfunction is determined by the Rutherford equation.

where index 0 denotes the equilibrium quantities and index 1 the perturbations, related to ξ . Only the two underlined terms can become negative, where the first is proportional to j_0 and the second is proportional to ∇p_0 . Hence, the related instabilities are referred to as “current driven” respectively “pressure driven”.

In the further course of this work, only current driven modes are of interest. These are in particular the internal kink mode, as well as the already introduced tearing mode. Both kinds of modes are equipped with periodic Eigenfunctions,

$$\xi = \xi(\psi) e^{i(m\theta^* - n\phi)}, \quad (2.2.16)$$

where the straight field line angle θ^* takes account of toroidicity and shaping of the plasma, which is also known as the Merezhkin correction. [21, p. 35].

Whereas the kink mode can be described from the ideal MHD and directly derived from Eq. 2.2.15, resistive effects in a small layer of the width $\delta \propto \eta^{1/4}$ around a resonant surface r_s cause tearing instabilities [21, p. 126]. Because of this, growth rates for both modes differ strongly. For the kink mode, it is in order of the Alfvén time τ_A . For the tearing mode, where it is an interplay of resistive and ideal effects, the timescale is a hybrid timescale much larger than Alfvén-scale but much smaller than the resistive-diffusion time. A schematic picture of the Eigenmodes of both modes is given in Fig. 2.2.

Rutherford equation An important feature of the tearing mode is the generation of a helical field perturbation Ψ_1 , that is equipped with a helical current perturbation j_1 .

2 Background

Due to $\nabla \cdot B = 0$, magnetic reconnection is forced inside the layer. Outside the layer, ideal MHD remains valid still, and the energy principle may be applied, as well. From that the tearing mode equation is derived:[21]

$$\Delta \Psi_1 - \frac{\mu_0 \partial_r j_{0,z}}{B_{0,\theta}(r)(1 - q(r)n/m)} \Psi_1 = 0 \quad (2.2.17)$$

Two independent solutions for Ψ_1 – inside and outside the rational surface – need to be found, which match asymptotically at r_s . This implies a jump of Ψ_1 , known as the linear stability parameter[26]

$$\Delta' = \left[\frac{1}{\Psi_1} \frac{d\Psi_1}{dr} \right]_{r_s - \delta/2}^{r_s + \delta/2} \quad (2.2.18)$$

If $\Delta' > 0$, then $\delta W < 0$ and the plasma is unstable against that tearing mode. The opposite applies for $\Delta' < 0$. As already visible from Eq. 2.2.17, the mode stability is highly related to the equilibrium current profile j_0 . A steep current gradient destabilizes the mode and also in case of $d_r j_{0,z}(r > r_s) > d_r j_{0,z}(r < r_s)$ the mode tends to be unstable. [21, 66].

From that, we can state at least two mechanisms, how a TM could be excited experimentally. [67]

1. The modification of the sign of stability parameter Δ' , which is related to the shape of j_0 . This is an axisymmetric effect which could be triggered for example by extensive cooling of the edge regions.
2. A more localized cooling at a rational surface could produce the helical, i.e., non-axisymmetric, current perturbation j_1 directly, which drives the island.

From linear theory to magnetic islands The linear theory described above is strictly speaking only valid for the determination of the mode stability. When the mode grows and reconnection sets in, the magnetic topology also changes outside the finite resistive layer. This eventually leads to macroscopic magnetic islands, with a periodicity determined by m and n of the corresponding tearing mode (see Fig. 2.6). The island size, i.e., maximum radial expansion at the O-Point, is given in an approximation for a circular, cylindrical plasma, i.e., by neglecting shaping and toroidicity:

$$W = 4 \sqrt{\frac{\bar{\Psi}_1}{\Psi_0''}} = 4 \sqrt{\frac{B_{1,r} r_s q}{B_{0,\theta} m q'}}. \quad (2.2.19)$$

After reaching a critical W , the temperature and pressure profiles within the island become flattened as mentioned before. [68, 27]

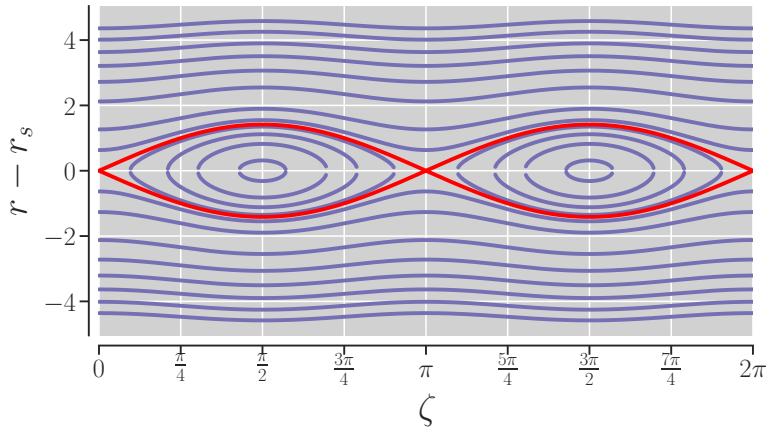


Figure 2.6: Schematic sketch of a (2/1) island. The surface in red is called the island separatrix. $\zeta \equiv \theta - \frac{n}{m}\phi$ is called the magnetic coordinate. O-Points at $\zeta = \frac{\pi}{2}$ and $\zeta = \frac{3\pi}{2}$; X-Points at $\zeta = 0$ and $\zeta = \pi$.

2.2.4 Extension of the MHD equations

Classical and turbulent transport The MHD equations as discussed before do not describe small-scale transport processes. *Transport* summarizes processes on a microscopic level, where turbulence and Coulomb-collisions between particles become non-negligible. These microscopic processes lead on sufficient time scales to a modification of the macroscopic quantities. The classical transport of particles can for example approximated by a diffusion term:[5, p. 285]

$$\left(\frac{\partial \rho}{\partial t}\right)_{\text{Diff}} \approx \nabla \bar{D}_{\text{classic}} \nabla \rho, \quad (2.2.20)$$

which is added to Eq. 2.2.2 and analogously to Eq. 2.2.4. The diffusion coefficient here is given as a tensor, as in particular the heat diffusion perpendicular to magnetic field lines is orders of magnitudes smaller compared to the parallel transport. Note, that also resistivity or viscosity are the result of collision processes and the regarding quantities σ and μ can be derived accordingly like in [69]. In a hot fusion plasma with strong logarithmic temperature gradients $\Delta T/T$, the turbulent transport is the dominating the Coulomb-collisions, which only have a small contribution.

Neoclassical effects In toroidal geometry, neoclassical effects become an additional feature. The inhomogeneity of $B_{\text{tor}} \propto 1/R$, leads to a gradient drift, such that a particle with $v_{\parallel} < v_{\perp}$ gets reflected on the magnetic field and can not complete full poloidal turns, but is trapped to so called “banana-orbits”. The trapped particles also have a distinct effect on the transport, which dominates over the classical one in toroidal geometry. [5, p. 438] In most regions of the plasma, collective turbulent processes actually dominate perpendicular transport.

2 Background

Bootstrap current The interaction of trapped and passing particles leads in a high β plasma (i.e., a plasma with large $\nabla_r p$) to an additional current, which has mainly a toroidal component. In regions of strong pressure gradients, the currents of trapped particles at different banana orbits do not cancel and produce a net current, referred to as bootstrap current. It is given in general by:

$$j_{bs} \propto -\sqrt{\eta} \frac{1}{B_\theta} \frac{\partial p}{\partial r}, \quad (2.2.21)$$

where $\sqrt{\eta}$ incorporates the fraction of trapped particles. A more distinct calculation for Bootstrap current fraction parallel to field lines is for example given by [70]. The bootstrap current fraction in today's experiments is large and enough to replace a fraction of the inductive current. [71]

Neoclassical tearing modes The flattening of the pressure profile within an island reduces j_{bs} . This reduction effectively represents a helical current perturbation, which has a consequence for the tearing mode: its stability becomes a function of the pressure profile and especially in H-modes discharges with large pressure gradients, the tearing mode can become non-linearly unstable even for positive Δ' provided a large enough seed island is produced by other mechanisms (for example caused by error fields[72] or traces of impurities[10]). This mode is referred to as a neoclassical tearing mode (NTM). The stability of an NTM is quantified by the modified Rutherford equation[73], which determines the meta-stability (see Section 2.2.3). A large 2/1 NTM can “lock” to the conducting structures surrounding the plasma, grow further, couple to other rational surfaces and trigger major disruptions. With increasing, β the minimum seed island size decreases. Consequently, the risk of NTMs limits the plasma performance and is of particular interest in disruption avoidance and mitigation.

2.2.5 The non-linear extended MHD code JOREK

The JOREK code resolves the non-linear extended MHD equations in realistic X-point geometries and is applied for a wide range of questions related to disruptions and edge localized modes. [74, 75, 76] The base physics model relies on reduced MHD, which eliminates fast magnetosonic waves while retaining the relevant physics for most applications in order to reduce the computational requirements. Available extensions cover for instance neoclassical effects, runaway electrons neutrals and impurities represented as fluids as well as particles or a dedicated SPI-model. Comparable codes are NIMROD[77], M3D[78] or M3D-C1[79]. This subsection describes the code version v2.20.07.0, on which most of the results are based on. Changes to the code made specifically for this work are mentioned later.

Base physics model JOREK follows an ansatz-based approach, for the formulation of reduced MHD with a toroidal coordinate system (R, Z, ϕ) . The toroidal magnetic field

B_ϕ is assumed to be dominating the poloidal part B_ψ such that:

$$B_\phi \gg B_\psi, \quad \frac{\partial B_\phi}{\partial t} = 0. \quad (2.2.22)$$

This allows to define the ansatz for magnetic fields by

$$B_\phi = \frac{F_0}{R} \vec{e}_\phi, \quad B_\psi = \frac{1}{R} \nabla \psi \times \nabla \vec{e}_\phi, \quad (2.2.23)$$

where F_0 is constant in time and space (contrary to $F(\psi)$ in Eq. 2.2.10) and the poloidal magnetic flux ψ is one of the quantities evolved in time. The electric field is in turn described by the velocity stream function u :

$$E = F_0 \nabla u \quad (2.2.24)$$

From that ansatz, it follows to express the velocity caused by $\vec{E} \times \vec{B}$ effects by:

$$v_\perp = v_{\vec{E} \times \vec{B}} = -R \nabla u \times \vec{e}_\phi, \quad (2.2.25)$$

Both u and ψ are evolved by the partial differential equations derived from Eq. 2.2.5, Eq. 2.2.6 and Eq. 2.2.7 resp. Eq. 2.2.3 and the projection operator $\vec{e}_\phi \times (R^2 \dots)$:

$$\frac{\partial \psi}{\partial t} = \eta j - R[u, \psi] - F_0 \frac{\partial u}{\partial \phi} \quad (2.2.26)$$

$$\begin{aligned} R \nabla \times \left(R^2 \rho \nabla_{\text{pol}} \frac{\partial u}{\partial t} \right) &= \frac{1}{2} [R^2 |\nabla_{\text{pol}} u|^2, R^2 \rho] + [R^4 \rho \omega, u] \\ &+ [\psi, j] - \frac{F_0}{R} \frac{\partial j}{\partial \phi} + [\rho T, R^2] + R \mu \nabla^2 \omega \end{aligned} \quad (2.2.27)$$

With the Poisson brackets defined by $[f, g] = \partial_R f \partial_Z g - \partial_Z f \partial_R g$.

The toroidal vorticity ω and toroidal current density j are linked to ψ and u by definition equations solved simultaneously to the time evolution equations for numerical reasons:

$$j = R^2 \cdot \left(\frac{1}{R^2} \nabla_{\text{pol}} \psi \right) \quad (2.2.28)$$

$$\omega = \nabla \cdot \nabla_{\text{pol}} u, \quad (2.2.29)$$

The ion mass density ρ and the ‘‘total temperature’’ $T = T_e + T_i$ are evolved according to continuity equations, with distinct parallel and perpendicular diffusion coefficients, derived from Eq. 2.2.2 resp. Eq. 2.2.4:

$$\frac{\partial \rho}{\partial t} = -v \times \nabla \rho - \rho \nabla \times v + \nabla \times D \nabla_\perp \rho, \quad (2.2.30)$$

$$\frac{\partial \rho T}{\partial t} = -v \times \nabla (\rho T) - \gamma \rho T \nabla \times v + \nabla \times (\kappa_\perp \nabla_\perp T + \kappa_\parallel \nabla_\parallel T). \quad (2.2.31)$$

2 Background

Here, the velocity is given by $v = \vec{v}_\perp + v_\parallel$. The parallel velocity v_\parallel is evolved by

$$\rho B^2 \frac{\partial v_\parallel}{\partial t} = -\rho \frac{F_0}{2R^2} \frac{\partial(B^2 v_\parallel^2)}{\partial \phi} - \frac{\rho}{2R} [B^2 v_\parallel^2, \psi] - \frac{F_0}{R^2} \frac{\partial(\rho T)}{\partial \phi} + \frac{1}{R} [\psi, \rho T] + B^2 \mu_\parallel(T) \nabla_{\text{pol}}^2 v_\parallel, \quad (2.2.32)$$

that is derived from Eq. 2.2.3 and the projection operator $B \times (\dots)$.

The Spitzer resistivity $\eta \propto T^{-3/2}$ [69], as well as the parallel heat conductivity $\kappa_\parallel \propto T^{-5/2}$ and the viscosity, $\mu \propto T^{-3/2}$ are temperature dependent coefficients. Eqs. 2.2.26 – 2.2.32 form the basic reduced MHD model in JOREK. A more detailed discussion can be found in [74, Chapter: 2.3].

Neoclassical extensions Several more neoclassical effects are covered by further extensions, which can be used optionally. Here, the bootstrap current is simulated consistently according to the density and temperature evolution using the Sauter formula [70] and included in Eq. 2.2.26. In a steady state limit, the Sauter bootstrap current density would be reached. This allows simulation of the neoclassical drive inside an island due to pressure flattening. [70, 74] The Sauter formula is being used outside its original validity limits during a disruption simulation, which assume axisymmetry and a steady state. Background flows could be evolved as well and for this purpose covered by Eq. 2.2.27. They are neglected for the simulations in this project, corresponding to the assumption of an MHD mode being already locked to the vessel, as worst case limit for disruptions [80, 12].

Background impurity model A temporally and spatially constant concentration of one or more selected impurities can be set, from which radiation losses are calculated. This yields – for each impurity – a power density term, which is added to Eq. 2.2.4:

$$\dots - L_{\text{rad}}(T_e, n_e) n_{\text{imp}} n_e \quad (2.2.33)$$

The background impurity density is given by n_{imp} . L_{rad} is a radiation coefficient for impurities in the equilibrium state and considers the losses caused by Bremsstrahlung as well as line radiation. Especially during a TQ, the coronal equilibrium assumption is not strictly justified, such that a more advanced model was created recently that is not used here for simplicity. [81] However, the assumption of equally distributed impurities is already a strong and outweighing assumption. Nevertheless, this simple model is sufficient to qualitatively investigate the effect of background impurities. L_{rad} is eventually calculated based on interpolated coefficients from the OPEN-ADAS database [31, 82], which covers a large set of data of atomic physics relevant for fusion and astrophysics. This provides coefficients in the collisional–radiative picture for line radiation, Bremsstrahlung, but also for the recombination and ionization of every charge state. Atomic data for relevant impurity species and hydrogen have been implemented into JOREK (see Fig. 2.7).

In the presence of sufficiently high impurity densities, low temperatures in the order of 10 eV may be reached, where Ohmic reheating strongly increases. This is represented

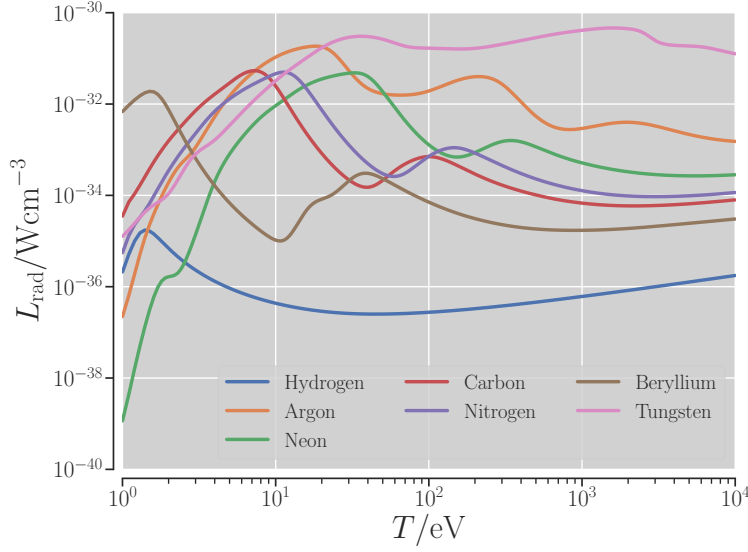


Figure 2.7: Equilibrium radiation coefficients of relevant elements at $n_e = 1 \times 10^{20}$ and varying T_e . The coefficients are calculated from OPEN-ADAS data.

by the optional term in Eq. 2.2.4:

$$\dots + \frac{2}{3R^2} \eta(T) j^2 \quad (2.2.34)$$

Neutrals and SPI-model Neutrals can be described by JOREK as an additional fluid; hence, the neutral density ρ_n is introduced as an additional variable and its evolution is given by,

$$\frac{\partial \rho_n}{\partial t} = \nabla \cdot D_n \nabla \rho_n + \alpha_{\text{rec}} \rho^2 - S_{\text{ion}} \rho_n \rho + S_{\text{SPI}}. \quad (2.2.35)$$

Here, an isotropic diffusion is assumed and the ionization and recombination terms are covered. Corresponding terms $-\alpha_{\text{rec}} \rho^2 + S_{\text{ion}} \rho_n \rho$ are added to Eq. 2.2.30. The ionization and recombination coefficients are taken from the OPEN-ADAS database, as well. The source term S_{SPI} describes the contributions to ρ_n by individual shards. In more detail, SPI is modelled as follows:

1. We assume the pellet to be shattered into shards, that are initialized at the beginning of the simulation.
2. Shards have initially virtually the same position, which are set by the user and is usually close but outside the computational domain – the shattering point. Each shard i is equipped with an individual, temporally constant velocity vector, which is varied randomly both in magnitude and the direction around a reference velocity

2 Background

\vec{v}_{ref} , By this, the shards travel in a cone with adjustable aperture α around the reference velocity vector.

3. For each shard, the ablation is calculated using a neutral gas shielding model[83]. In this model, a given heat flux along the field lines crossed by the shards must be depleted by a certain line integrated neutral density along the field line, in order to keep the heat flux at the shard's position close to zero. From this, the ablation rate, that is proportional to the neutral source term for a deuterium pellet, can be estimated by:

$$\left(\frac{\partial N}{\partial t}/\text{s}^{-1}\right) = 4.12 \times 10^{16} (r_i/\text{m})^{4/3} \cdot (n_e/\text{m}^{-3})^{1/3} \cdot (T_e/\text{eV})^{1.64}. \quad (2.2.36)$$

Here, r_i is the shard radius and T_e and n_e are the electron temperature and density.

4. The exact source term of each shard is assumed to be quasi Gaussian shaped in poloidal and toroidal direction and eventually, the contribution of each shard is modelled by:

$$S_n(R, Z, \phi) \propto \left(0.5 - 0.5 \tanh \frac{(R - R_i)^2 + (Z - Z_i)^2}{\delta r_c}\right) \cdot \left(0.5 - 0.5 \tanh \frac{\phi - \phi_i}{\delta \phi_c}\right), \quad (2.2.37)$$

where (R_i, Z_i, ϕ_i) are the coordinates of shard i and δr_c and $\delta \phi_c$ determine the poloidal and toroidal expansion assumed for the shard.

Numerical methods The poloidal plane is discretized using bi-cubic Bézier finite elements, involving third order Bernstein Polynomials. For the toroidal expansion, a real Fourier series is applied. The basis function of the zeroth harmonic equals 1. The n^{th} harmonic ($n > 0$) is given by the pair of basis functions $\cos(n\phi)$ and $\sin(n\phi)$. The harmonics to be included in a simulation are selected by parameters. Time evolution is performed using the fully implicit Gears scheme [84]. Thanks to implicit time schemes, large time steps in order of the physical time scales of interest are allowed, which are usually anywhere between one and 10,000 Alfvén times. At each step and for each toroidal harmonic, a weak form of the reduced MHD equations introduced above is constructed and solved with the iterative scheme GMRES and using a physics based preconditioning involving the PaStiX [85] sparse matrix library. Further details about the discretization and time evolution in JOREK are given in [74].

Equilibrium calculation On an initial polar poloidal grid, the Grad-Shafranov-equation 2.2.11 is solved. The pressure profile, as well as $(F\partial_\psi F)(\psi)$ are needed as input along with the Ψ values on the boundary of the computational grid. All this typically comes from experimental equilibrium reconstruction by the CLISTE code[86]. Once the equilibrium has been solved in JOREK, a flux aligned grid is calculated, that yields computational advantages to handle the strongly differing magnitudes of parallel and perpendicular gradients.

2.3 Scientific questions

The focus of this work is to investigate theoretically the behavior of deuterium massive material injection for plasma dilution in a plasma with pre-existing island structures – a situation that is comparable to the pre-TQ phase.

Of interest are in particular injection parameters that are marginal for triggering a TQ shortly (within ~ 1 ms) after plasma dilution has happened. These cases can be seen as a worst-case, where the TQ occurs just after the plasma density has been increased. A possible worsening effect of pre-existing islands is most critical in this scenario. Due to the impact of the islands on the local temperatures around the shard cloud, they may have a direct impact onto the ablation. If it leads to too low temperatures in inner regions, full ablation may be not guaranteed anymore, which would lower the effectiveness of plasma dilution. In turn, higher initial perturbation amplitudes may increase the risk of an early TQ, when they superpose with the perturbations triggered by SPI. This could shorten the cooling time to values not sufficient for plasma dilution. The involuntary generation of RE, especially by the hot tail, when n_e has not yet increased much, could be the consequence of a too short cooling time. Further, longer cooling time, i.e a late TQ, are advantageous, as this gives the DMS more time to trigger for example impurity-SPI as a second step of mitigation. Hence, the central questions addressed in this thesis are:

- What are the effects of pre-existing islands for the TQ formation?
- Is plasma dilution prior to the TQ viable using deuterium injection also in MHD active plasmas?
- Which role do background impurities play for this mitigation strategy?

The aim is to deduce predictions from these examinations, whether the aforementioned strategy of plasma dilution for RE suppression is still applicable in a pre-TQ phase.

3 Massive deuterium injection into an ASDEX Upgrade equilibrium

Motivated by the scientific questions stated above, several series of non-linear simulations of massive deuterium injection into an MHD active plasma were performed. All simulations are based on ASDEX Upgrade L-mode equilibria. The basic physical mechanisms are of interest throughout the whole thesis, where detailed experimental comparisons are left for further work. This allows to avoid the more challenging dynamics with a steep H-Mode pedestal or the H-to-L transition. In this chapter, parameter scans are performed regarding three parameters:

- the initial island size w_i ,
- number of injected atoms N_{SPI}
- and the relative phase between island O-point and injection location ϕ_{O} .

In Subsection 3.1, the setup is briefly presented. This includes descriptions of the plasma equilibrium and the generation of the magnetic perturbations. The code used for this series of simulations has been presented in Subsection 2.2.5.

The results are discussed in detail, beginning with Section 3.2: we study the injection into an unperturbed plasma, varying the amount of injected material. This is done to establish a baseline to which we can compare later on and to determine the amount of injected deuterium needed for triggering a TQ shortly after core dilution. We expect the influence by pre-existing MHD activity to be most critical in a scenario close to this threshold. In this first results section, we also characterize the MHD activity triggered by the injection itself. Injections into the island O-point of a pre-existing magnetic island are then studied in Section 3.3 for different initial island sizes. The dependency onto the injection phase with respect to the pre-existing island is studied in detail in Section 3.4, where the injection location relative to the island is varied systematically. Here, we highlight in particular, that an injection into the immediate vicinity of the island X-point leads to a different plasma response and earlier TQ than the injection into other phases.

Simulations involving background impurities are presented in Chapter 4.

3.1 Simulation setup

The model used for these simulations is as explained in Subsection 2.2.5, including neutrals and the SPI-model and the consistent evolution of the bootstrap current fraction.

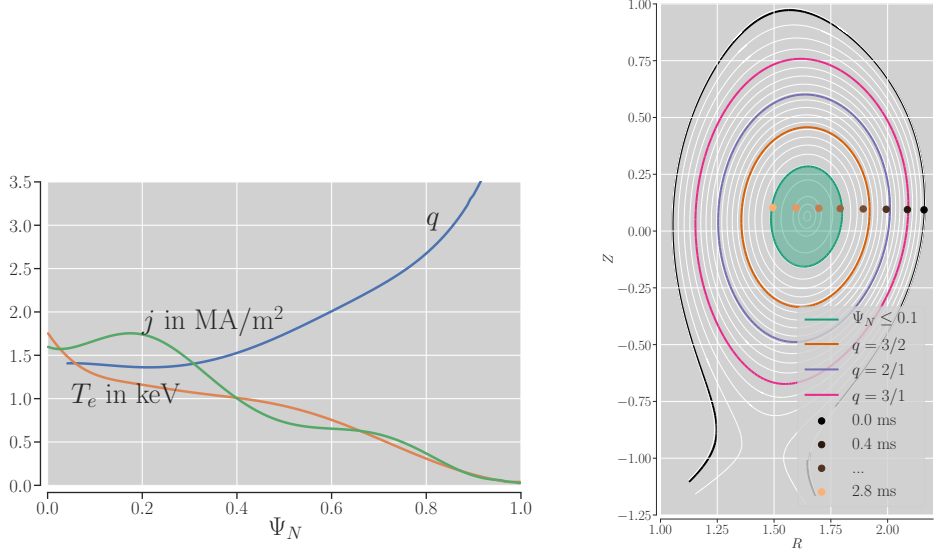


Figure 3.1: Left: Profiles of the ASDEX Upgrade L-mode-like equilibrium considered in the present study. Right: poloidal cut of the initial flux surfaces with some relevant resonant surfaces marked as well as the average shard cloud position every 0.4 milliseconds. The core region ($\Psi_N \leq 0.1$) is shaded green.

The background impurity model as well as thermal energy gains from Ohmic reheating are ignored. Since this project addresses the dynamics between mode locking up to the TQ only, background flows, RE or free boundary extensions are not taken into account. The poloidal plane is discretized by 8200 elements, while the Fourier decomposition of the toroidal direction includes all modes from the axisymmetric part $n = 0$ up to $n_{\max} = 6$.

The initial ASDEX Upgrade equilibrium The L-mode ASDEX Upgrade equilibrium, on which these simulations are based on, exhibits an electron temperature on the magnetic axis of $T_{e,0} = 1.7 \text{ keV}$ and a density of $n_{e,0} = 2.1 \times 10^{19} \text{ m}^{-3}$, respectively. Profiles of temperature, current density and q profiles are presented in Fig. 3.1.

To guarantee the avoidance of intrinsic core instabilities, that would need a more complex model for realistic simulations [87], an initial safety factor of $q_0 = 1.4$ is taken well above unity. With a rational surface $q = 2$ at $\Psi_N = 0.59$ initially, the equilibrium is also stable against any tearing modes. The resistivity is modelled as given in Subsection 2.2.5, where we assume a value on the magnetic axis of $\eta_0 = 1 \times 10^{-7} \Omega \text{ m}$. This modelling however neglects neoclassical effect of electron trapping. Because of this, a realistic value around the $q = 2$ surface, would be smaller by a factor of 2.5 according to Ref. [9, Chapter 14.10].

We emphasize here again, that the focus of these studies is in the dynamics during the disruption onset, i.e., just up to the occurrence of the TQ. The work does not require analyzing details of the TQ. Hence, we do not simulate the actual TQ to save

computational costs, even though a continuation of the simulations was possible in most of the cases from a numerical point of view. A fully realistic TQ modelling would need additional extensions, like the inclusion of Ohmic heating, background impurity radiation or separate electron and ion temperatures, however. To have a more accurate and objective definition, we define the occurrence of the TQ as the point in time of full stochastization (t_{FS}). Furthermore, at t_{FS} the temperature and density profile should flatten out completely. This event is expected to be triggered by a violent crash. We will look for every case, if full stochastization (FS) is reached, and may define t_{FS} . Hence, an objective analyses of the duration of the whole disruption onset is possible.

3.1.1 Generation of the initial perturbation

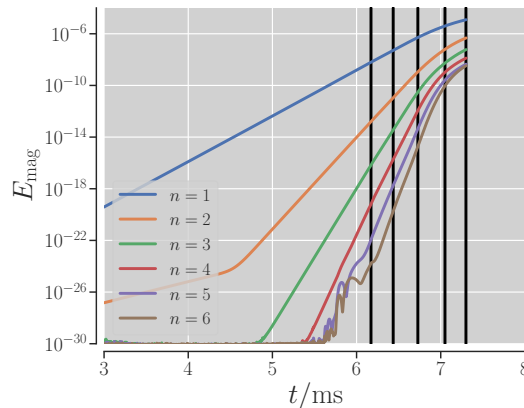


Figure 3.2: Growth phase of the 2/1 island in the classically unstable equilibrium. Mode coupling is observable as described in [6]. Vertical lines mark the time points, from where the perturbations were taken and important into the classical stable equilibrium.

In these studies, we are only interested in pre-existing islands of different sizes themselves without exactly knowing their origins and growth, i.e., the sequence during the disruption onset just before the SPI triggering. Since we thus do not have to reproduce the true experimental triggering mechanisms for seed islands, the following approach is made: in a separate simulation, the current gradient around the $q = 2$ surface is increased. This renders the 2/1 tearing mode classically unstable (see Fig. 3.2). From different time points within this separate simulation, the obtained magnetic islands are exported into the original classically stable equilibrium. This leads to initial island sizes of 0.8 cm, 1.5 cm, 2.5 cm, 4.5 cm and 6 cm respectively. They evolve after initialization fully self-consistently as a neoclassical tearing mode. Due to the bootstrap current drive, their sizes stay virtually constant, at least within a time frame of ≈ 10 ms, which is relevant for these disruption studies. A dedicated extension of JOREK for importing of magnetic perturbations was implemented as part of this project.

3.1.2 Setup of the shattered pellet injection

A pure deuterium pellet would produce a cloud of very small pieces and gas if truly shattered, which would lead to much worse penetration properties. Instead, we propose in these simulations the approach of an only “weakly-shattered” pellet, which constitutes as a pellet broken into ten shards of equal size allowing for deep penetration of the material. Shortly after the imported islands have established, the SPI is activated at $t = 0.1$ ms from the outer midplane. Neutral gas shielding [83] is applied for the ablation modelling. For numerical reasons, the poloidal radius of each shard cloud is set to 8 cm, which is for itself an unrealistically large value, however. In general, the cloud expansion is modelled here only in very simple way. Important mechanisms, that are not taken into account are: first, the fast so-called ambipolar expansion in parallel direction, which is caused by strong local pressure gradients, as well as the transparency of the plasmoid in respect to the ambient field lines. [88] Second, a strong drift of the plasmoid towards the low field side, which results into a stretching in perpendicular direction of a few centimeters. [89]. The assumption of a relative large cloud tries to compensate for the neglect of these mechanisms. For each shard, an initial velocity vector is selected randomly around a reference velocity of $250 \text{ m/s} \pm 40 \text{ m/s}$ pointing in major-radial direction. To enable direct comparisons, these shard velocity vectors are identical in all simulations. Averaged positions of the shards at some time points are given in the poloidal cut in Fig. 3.1. In cases with pre-existing island, we choose the toroidal injection phase ϕ_O in most simulations such that the shards directly hit the island O-point, $\phi_O = 0^\circ$. This is varied and discussed later in this chapter (Section 3.4), where we assess the effects of different injection phases. Here, $\phi_O = 180^\circ$ corresponds to X-point injection.

Five different values for the amount of injected atoms N_{SPI} are considered: 3×10^{20} , 6×10^{20} , 1×10^{21} , 3×10^{21} , 6×10^{21} . They are injected into the plasma with an initial total particle content of 1.9×10^{20} . All together, including simulations without pre-existing island, more than 70 non-linear simulations are performed and analyzed.

In the following discussions, two mechanisms for plasma cooling are of interest: only dilution and hence adiabatic cooling or heat losses by degraded confinement. To distinguish between both mechanisms, the evolution of the total thermal energy E_{total} content and the total particle content N_{total} are compared. N_{total} increases and E_{total} remains constant in case of pure dilution. In contrast, a degradation of the energy confinement results in a drop in E_{total} . Additional understanding of the local dynamics in the vicinity of the magnetic axis is given by analyzing “core particle content” N_{core} and “core thermal energy” E_{core} . This core region is defined as the volume inside the initial $\Psi_N = 0.1$ surface.

To analyze the magnetic dynamics, we make use of a continuous description of the island width evolution, which even remains applicable during stochastization, where the Poincaré plots do not allow measuring the island sizes anymore. Therefore, an analytic

estimation of island widths is given based on Eq. 2.2.19:

$$w_{m/n} = c \cdot 4 \sqrt{\frac{\Psi_{m,n} q^2}{B_\theta q' m}}, \quad (3.1.1)$$

The prefactor $c = 0.7$ is determined empirically by comparing the analytical expression with Poincaré plots at several time points. $\Psi_{m,n}$ denotes the m/n component of the poloidal magnetic flux in straight field line coordinates on the rational surface. This approach has been applied previously, e.g., in Ref. [90].

In the following sections, the results are represented. We begin with cases where only the massive material injection is activated without a pre-existing island.

3.2 Injection into an unperturbed plasma

3.2.1 Dynamics with varying amounts of injected material

Initially, the plasma of interest contains a thermal energy of $E_{\text{total},0} = 71$ kJ and $N_{\text{total},0} = 1.9 \times 10^{20}$ deuterium ions. The core region, which was previously defined by the region of $\Psi_N \leq 0.1$, contains a thermal energy of $E_{\text{core},0} = 14.5$ kJ and $N_{\text{core},0} = 0.2 \times 10^{20}$ deuterium ions initially. As sources and diffusion are not perfectly in balance, 9.5% of the thermal energy and 5% of total particle content are lost within 4 milliseconds in the absence of an injection by diffusive cross-field transport. Compared to the changes induced by the material injection and the MHD modes, this is negligible.

An overview of the dynamics in the various cases with different amounts of material injected is given in Fig. 3.3 where the time evolution of the particle content and thermal energy content in the complete plasma and in the core region are shown. The shards are injected at $t = 0.1$ ms and begin to affect the plasma dynamics at a simulation time of $t = 0.3$ ms by increasing the total particle content as well as by decreasing the total thermal energy content. The dynamics obtained with different amounts of material injected are discussed in the following.

- For the smallest amount of injected material, $N_{\text{SPI}} = 3 \times 10^{20}$, the shards are fully ablated 1 ms after they have started to affect the plasma. The ablation leads to a relative increase of the total particle content by about, 150% and around 93% of the injected material is assimilated. The material assimilation is strongly enhanced in our case, compared to previous deuterium SPI studies for AUG Ref. [47]. This is given by the fact, that an L-mode plasma is studied here, that is less prone to violent ELM-like edge instabilities. The total thermal energy decreases by 10% during ablation as a result of losses induced by edge MHD activity, but is decaying only slightly afterward, indicating, that the edge confinement restores. Only from $t = 1.7$ ms, which is several hundred microseconds after full ablation, the core thermal confinement reduces significantly. The decay of E_{core} abates successively after $t = 1.9$ ms. Eventually, N_{core} has increased by 120% around $t = 2.5$ ms. During the simulated time, a FS is not reached. Hence, the plasma would either recover or exhibit TQ at a fairly late point in time.

3 Massive deuterium injection into an ASDEX Upgrade equilibrium

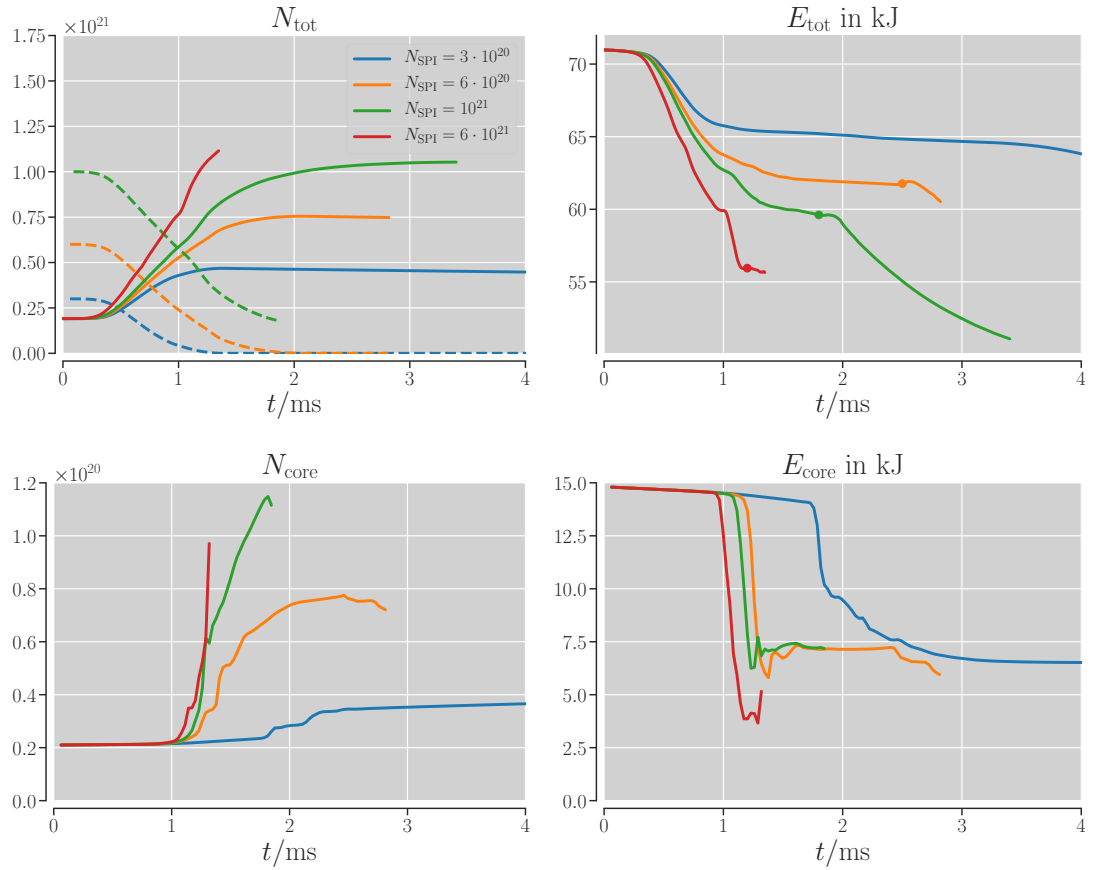


Figure 3.3: Evolution of total (top row) and core (bottom row) particle content (left column) and thermal energy content (right column) for runs without a pre-existing island. Dashed lines show the total particle content of the remaining shards of the corresponding run. The case of $N_{\text{SPI}} = 6 \times 10^{20}$ leads to a delayed FS about 1.5 ms after the shards started to dilute the core region and about 0.5 ms after full ablation. Simulations are usually stopped after reaching t_{FS} (marked by circles in the right upper plot), i.e., when FS is reached and the temperature in the whole plasma flattens.

- For $N_{\text{SPI}} = 6 \times 10^{20}$, the particle content increases by nearly 300% when full ablation is reached, which happens only at $t = 1.9$ ms. Again, a high fraction of material of around 93% is assimilated. At around $t = 1.2$ ms, the core energy drops rapidly by more than 50% within about $100\mu\text{s}$. The core particle content increases gentler due to different time scales for the radial transport of heat and particles. After this drop in E_{core} , the total and core thermal energies stay rather constant for 1.4 ms, while N_{core} increases monotonously by up to 400%, what corresponds to a maximum value of about 0.8×10^{20} . As expected, the larger amount of injected material dilutes the core more efficiently. FS sets in at $t_{\text{FS}} = 2.5$ ms, which is

followed by drops of total and core thermal energy, as well as core particle content. As explained before, we do not continue the simulations beyond FS.

- For further increased amounts of injected material, the dynamics are qualitatively similar to the $N_{\text{SPI}} = 6 \times 10^{20}$ case. The $N_{\text{SPI}} = 1 \times 10^{21}$ case exhibits $t_{\text{FS}} = 1.8$ ms. This case can be compared to case C in Ref. [47] (to distinguish it from the L-mode case studied here, this case C is called “H-mode” case in this paragraph). The SPI setup in that case is very similar. Only the number of shards is different, where 30 shards are initialized in contrast to 10 here. In the H-mode case, a TQ was also observed shortly after injection. The core temperature behaves qualitatively similar: it crashes about one millisecond after injection and within three hundred microseconds. The evolution of the core density differs, where it stays virtually unaffected in the H-mode case, contrary to the L-mode case, which can be explained by reduced penetration depth because of the larger number of shards and the higher temperatures in the H-mode case.
- Already at $t = 0.9$ ms a rapid drop of E_{core} sets in for $N_{\text{SPI}} = 6 \cdot 10^{21}$, i.e., the largest amount of material. 300 ms later, 1/6 of the injected material has been ablated, but N_{tot} is already six times larger than the initial value. The thermal confinement is lost globally after $t = 1$ ms and local temperature around the shards fluctuate, leading to varying ablation rates. Around $t_{\text{FS}} = 1.2$ ms, full stochastization is reached.

The dynamics with the different amounts of injected material can be summarized into three different regimes:

- for $N_{\text{SPI}} = 3 \times 10^{20}$, the heat confinement is degraded temporarily and the core particle content increases. A prompt TQ is not triggered, however, as the MHD activity is not sufficiently excited.
- With the doubled amount of material, the first impact onto N_{core} sets in around $t = 1.2$ ms. A first burst of MHD activity follows. After that, plasma stabilization sets in, which leads to a delay of FS, which only occurs after further 1.3 ms. The shards have already fully ablated after that time.
- If injecting even more material, FS is triggered immediately, when shards are still far outside the plasma core and are only partly shattered.

3.2.2 Detailed analysis for 6×10^{20} atoms injected

As the aim of this thesis is to assess the impact of pre-existing islands onto the strategy of plasma dilution prior to the TQ, the case with a delayed FS shortly after plasma dilution ($N_{\text{SPI}} = 6 \times 10^{20}$ atoms) is of particular interest. This scenario can be considered as a limiting case between the other two regimes of reaching or not reaching FS discussed before, and may be expected to display a high sensitivity to pre-existing MHD modes.

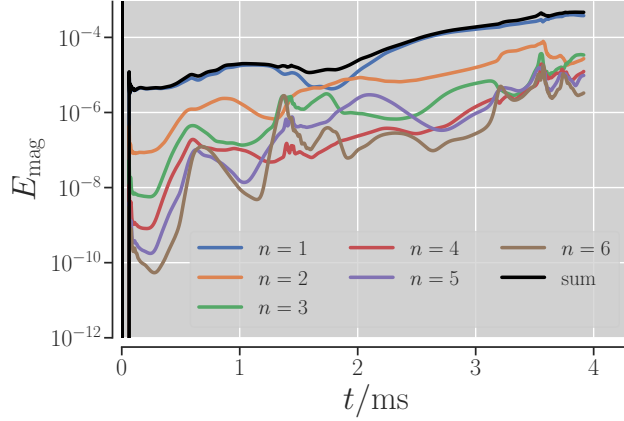


Figure 3.4: Case with $N_{\text{SPI}} = 6 \times 10^{20}$. Magnetic energies show a strong coupling during the first MHD burst at $t = 1.2$ ms and successively a partial decay of the higher modes while $n = 1$ keeps growing continuously. The TQ onset is again correlated to strong mode coupling (around $t = 2.5$ ms).

Therefore, the rest of the section will focus on the analysis of the $N_{\text{SPI}} = 6 \times 10^{20}$ case, to which the cases with pre-existing islands can be compared in the following sections.

Fig. 3.4 shows the time evolution of the magnetic perturbation spectrum excited by the material injection. All toroidal $n \neq 0$ modes included in the simulation ($n = 1 \dots 6$) become excited, when the shards enter the separatrix. This is usually observed in MMI-simulations. The dominant $n = 1$ mode is dominant throughout most of the simulation. This is a usual feature of the single toroidal injection, which is investigated here. The situation would be different in case of multiple injection ports. When the shards arrive at the $q = 2$ surface, around $t = 0.8$ ms, this situation changes transiently: for a few hundred microseconds, the $n = 1$ magnetic perturbation is decreasing, and the $n = 2$ mode becomes dominant as a consequence. This behavior indicates a phase transition of the 2/1 perturbation, which is covered later in this section. After $t = 1$ ms, i.e., when the core particle content begins to increase, modes of higher order become excited due to strong non-linear mode coupling. This begins with the fifth harmonic starting from low amplitude, followed by other $n > 1$ modes and eventually leads to a burst of MHD activity around $t = 1.2$ ms. The consequence is the first crash and a decrease of core confinement – a partial loss of E_{core} , as described before. The shards are located around the $q = 1.5$ surface during that crash and now lead to a strong increase in N_{core} . In contrast, the global values E_{tot} and N_{tot} are only weakly affected by this first crash, which indicates, that it corresponds largely to a re-distribution inside the plasma.

After this crash, the amplitudes of all $n > 1$ modes drop transiently and the core is successively diluted. The full ablation is given at $t = 1.9$ ms and at this point, the last shards have even reached the $\Psi_N = 0.1$ surface. From $t = 2.3$ ms, we can identify the onset of a second crash, which eventually ends up in FS: modes of higher order begin to grow again, and strong mode coupling is visible at around $t = 2.5$ ms. This crash is

3.2 Injection into an unperturbed plasma

more violent, as larger amplitudes for all modes are reached. After FS – from $t = 2.6$ ms – the total energy starts to drop which was expected due to the strong degradation of the confinement. The simulation is not continued further, as the dynamics after FS are out of scope for this study.

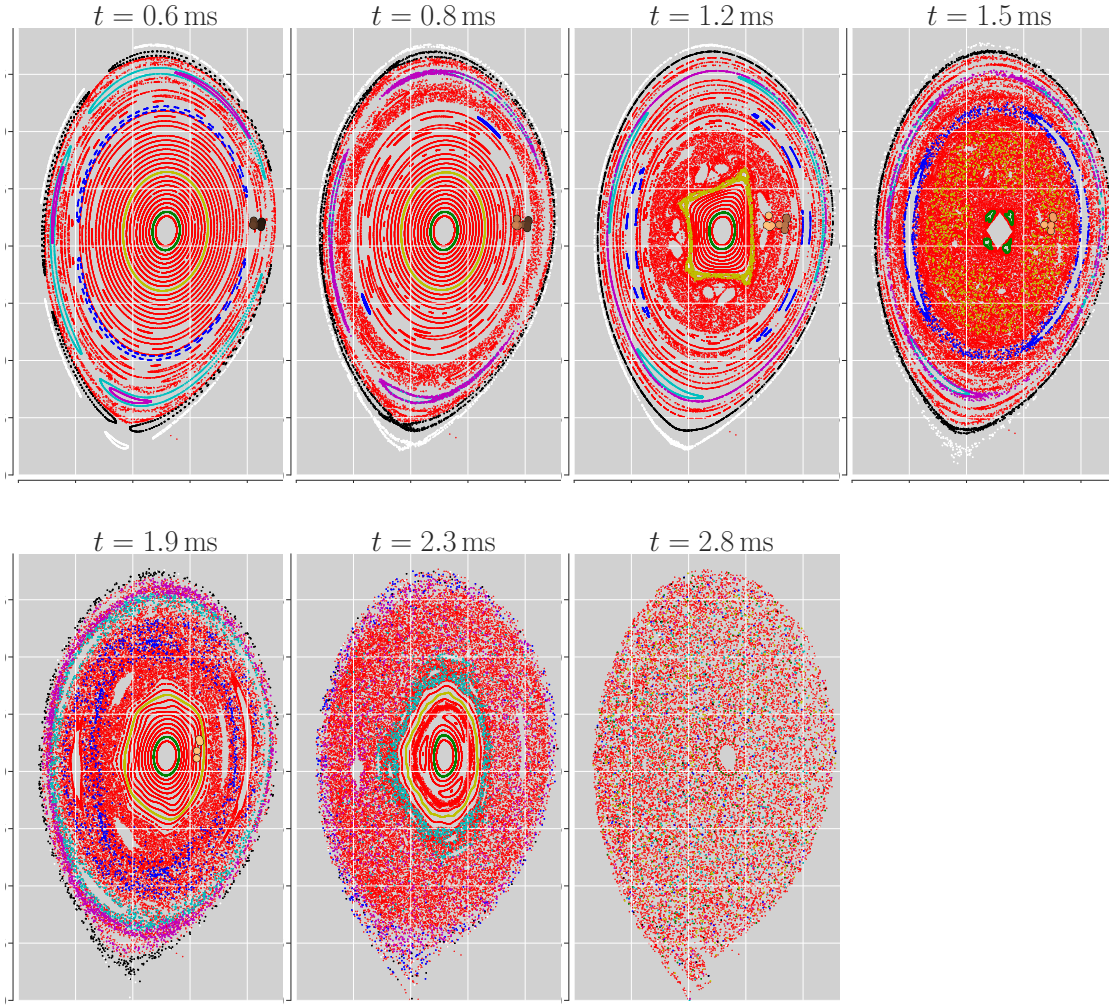


Figure 3.5: Case with $N_{\text{SPI}} = 6 \times 10^{20}$. Poincaré plots are shown at various time points during the simulation, from an early stage where only small islands have formed up to the point of FS.

In the following, the dynamics described in the previous paragraphs are validated against a series of Poincaré plots in Fig. 3.5. The 2/1, the 3/2 and the 4/3 modes are in particular present shortly before the first crash, at $t = 1.2$ ms. When they continue to grow during the first crash ($t = 1.2 \dots 55$ ms), the full region inside the $q = 2$ surface stochastizes, while edge regions remain stable. During the crash, the (virtual) size of the 2/1 island increases from $w_{2/1} = 60$ mm by one centimeter by the end of the first crash.

3 Massive deuterium injection into an ASDEX Upgrade equilibrium

Shortly after, a reformation of flux surfaces in the central region ($\Psi_N < 0.3$) is following from $t = 1.7$ ms to $t = 2.2$ ms. Simultaneously, the outer regions are now breaking up, which is driven by a continuous growth of the 2/1 and 3/1 modes. Eventually, just prior to the second crash, the 2/1 island has reached a width of $w_{2/1} \approx 170$ mm. During the second crash, the flux surfaces in the center stochastize again. The dynamics in the outer and inner regions lead together to FS at $t_{\text{FS}} = 2.5$ ms.

An interesting feature of the magnetic dynamics are the island phases, which is discussed later: at an early time, when the shards have not entered yet the $q = 2$ surface, $m = 1 \dots 5/n = 1$ modes are excited, that have their X -points in toroidal phase with the injection nozzle. This changes, when the shards pass the $q = 2$ surface and the modes exhibit a phase shift of $\Delta\theta = -90^\circ$ in poloidal direction. Subsequently, the 2/1 island continues to growth, having the O -point now in phase with the injection nozzle.

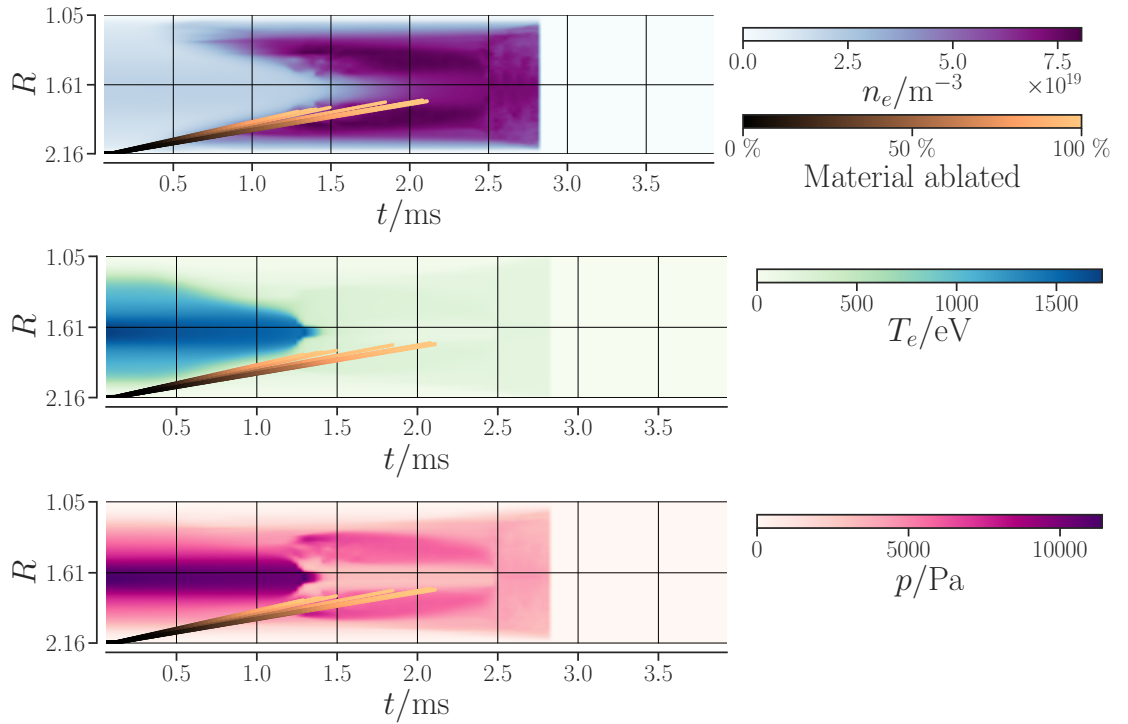


Figure 3.6: Midplane profiles of density (top), temperature (middle) and pressure (bottom) are shown for the case with $N_{\text{SPI}} = 6 \times 10^{20}$. A rapid drop of central temperature as well as central pressure occurs, when the first shards pass the $q = 3/2$ surface at $t = 1.2$ ms. The pressure profile becomes hollow after this first crash while the core gets continuously diluted (see density at the top). Only during the second crash corresponding to full stochastization (around $t = 2.5$ ms), pressure, temperature and density profiles flatten across the whole plasma domain. The trajectories of each shard are shown by black-orange lines, where the color represents the respective fraction of the material ablated.

However, in the following we will first discuss the time evolution of the (toroidally averaged) density, temperature and pressure profiles across the midplane based on Fig. 3.6 of this case ($N_{\text{SPI}} = 6 \times 10^{20}$ and no pre-existing island): adiabatic cooling is the primary effect of the injection up to the first core crash: because of that, the temperature profile of the outer regions up to the $q = 1.5$ surface decreases, while the pressure profile remains largely unchanged. Since temperature and density in the core remain constant meanwhile, a hollow density profile establishes. This changes during the first crash, around $t = 1.2$ ms: the core stochastizes and radial heat transport along field lines enhances. Consequently, the temperature becomes fairly uniform across that domain by dropping from 1400 eV to below 250 eV within $300 \mu\text{s}$. The timescales of particle transport along the field line are much longer and are around the ion sound speed, so that the density profile changes much less in that time interval. This leads to a hollow pressure profile from now on. Flux surfaces in the center reform after the first crash, which reduces once again the radial transport coefficients: the profiles of pressure, density and temperature remain qualitatively constant in its shape up to the second crash. Between both crashes and up to $t = 2.1$ ms, the remaining small shards provide a continuous core fueling and hence an adiabatic cooling of the core. This effect is much less compared to the adiabatic processes in the beginning of penetration, due to reduced ablation at lower temperatures. Increasing field stochasticity of outer regions let the pressure profile relax at $t = 1.8 \dots 2.4$ ms. The second crash happens at during $t = 2.5 \dots 2.7$ ms, where the entire pressure flattens. The effect of the second crash on the already flattened temperature is moderate.

As already presented in Subsection 2.2.3, two ways of excitation a NTM are conceivable. Both can be reproduced in these simulations, and we want to assess in the following, which one of both mechanisms plays the dominant role here. This requires an additional test: The simulation is performed, where the Spitzer-like resistivity $\eta = \eta_0 (T_{e,\text{axi}}/T_{e,0})^{-3/2}$ is only calculated from the axisymmetric $n = 0$ component of the temperature $T_{e,\text{axi}}$. The non-axisymmetric drive of the island by the helical cooling is removed by this, and only the axisymmetric change of the current profile can drive the island size. A similar behavior compared to the original case in terms of the evolution of the island widths (see Fig. 3.7) can be seen at first. This changes after $t = 0.6$ ms, when the island size does not exceed $w_{2/1} = 18$ mm and no islands with higher n are excited. From this, we can conclude, that in our simulations helical cooling dominates the dynamics leading to the TQ.

3.2.3 Change of the island phase during the injection

In the beginning of this section, the unexpected feature is described, that the shards trigger a $n = 1$ islands of small widths with X-point in phase with the injection location initially. In this subsection, that behavior is analyzed more in depth based on the 2/1 mode, where we look on the 2D-Fourier decomposition of the poloidal flux Ψ : the component associated to the 2/1 mode ($\Psi_{2/1}$) exhibits a phase jump of π at the rational surface around $t = 0.6$ ms (Fig. 3.8). An amplitude close to zero is detected on the rational surface $q = 2$, which corresponds to a very small island size and local minimum

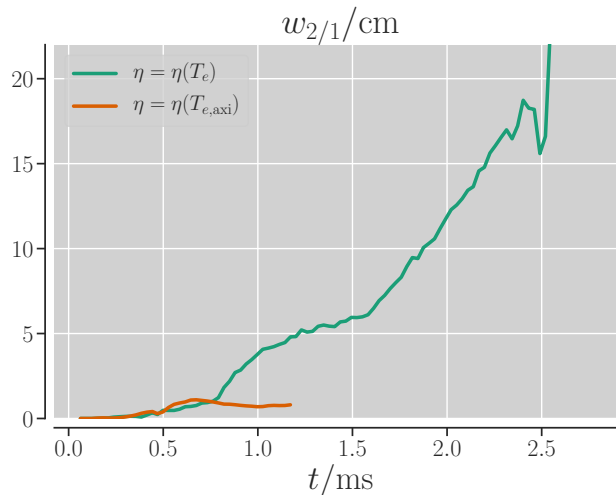


Figure 3.7: Evolution of the 2/1 island width for two approaches of calculating the Spitzer-resistivity η . When it is calculated from the axisymmetric part of the temperature $T_{e,\text{axi}}$ (orange curve), the perturbation energy monotonously decays after $t = 0.6$ ms. The strongly increasing mode activity eventually leading to the TQ is only observed, when taking the helical temperature perturbations into account for the resistivity calculation (green curve). This confirms the important role of helical cooling, in particular on the $q = 2$ surface, for the plasma dynamics.

inwards respectively a local minimum outwards from the surface refers to as a kink parity dominated response. Only when the shards have reached the rational surface ($q = 0.8$ ms), a growing tearing structure becomes visible, which interferes with the kink structure and dominates it after around $t = 1$ ms. The phase jump disappears then, we eventually just see the structure of a tearing mode Eigenfunction in $\Psi_{2/1}$ and the 2/1 island with O-point in phase with the shards appears. In other words, we see the behavior as expected for a magnetic island driven by helical cooling by then.

The behavior of the plasma prior to the occurrence of the TM is not fully understand, yet it is likely to be the result of a strong deformation of the equilibrium: In the first hundred microseconds after injection, a strong pressure perturbation in particular around the rational surface is the result of the material deposition. This yields to a quintupling of the radial pressure gradient on the low field side, which is now at $|\nabla p_r| \approx 180 \text{ kN/m}^3$ (see Fig. 3.9). The response to this is a perturbed flux $\Psi_{2/1}$ of kink parity. This leads to a flux surface deformation in the region of the strong pressure gradient and finally to reconnection, i.e., the generation of an X-point. The amplitudes of $\Psi_{2/1}$ and ∇p_r around $q = 2$ at the relevant time interval ($t \approx 0.5$ ms) scale proportionally, a scan through N_{SPI} shows. The temperature perturbation T_e^* is however much less established up to then. It is very asymmetric between high and low field side. Therefore, the tearing parity can not yet establish well. Later, the material distributes, when the shards move further

3.3 Injection into the O-point of a pre-existing 2/1 magnetic island

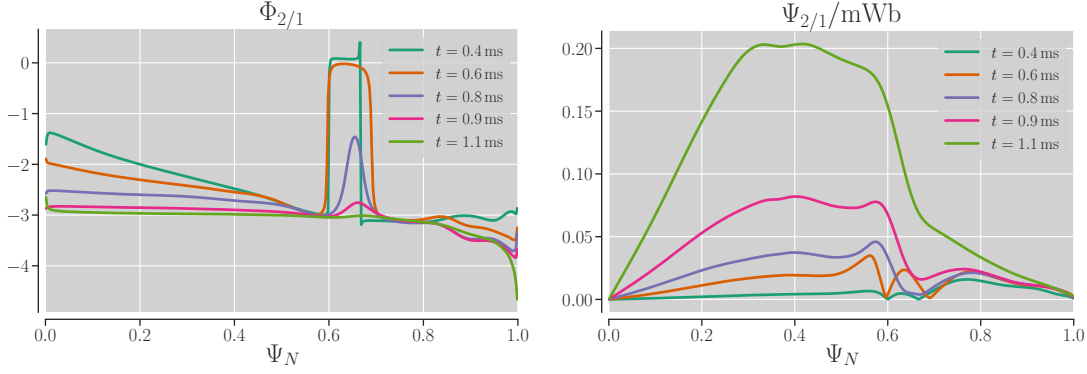


Figure 3.8: Complex phase (left) and amplitude (right) of the perturbed flux component $\Psi_{2/1}$ are shown in the early stage after injection. First (0.4 and 0.6 ms), a strongly kink dominated structure (phase shift at the $q = 2$ surface at $\Psi_N = 0.59$) is observed such that the small 2/1 island can be seen as a resistive MHD consequence of the strongly dominating ideal kink response. In this phase, the 2/1 island has the X-point in phase with the injection location. Later ($t \geq 0.8$ ms), the tearing structure starts to strongly dominate over the kink component, which coincides with the time at which helical cooling starts to take over as the main driver of the magnetic perturbation evolution. Here, the island O-Point is in phase with the shards, as expected for helical cooling ($\Psi_{2/1} \approx -\pi$).

into the plasma. Hence, the strong local pressure gradient decreases, while T_e^* begins to dominate from $t = 0.9$ ms, which drives the kink parity eventually.

We conclude from these observations, that the mode excitation comes possibly from an interplay of the pressure perturbation driven from the local density increase in the vicinity of the shards and the resistivity perturbation driven by helical cooling. The pressure perturbation is very peaked in the beginning and a kink mode is excited from that. This leads to reconnection in the region of the shards. After some time, the pressure profile relaxes and the localized, helical cooling of the rational surface dominates. Then, a tearing mode is excited, which produces a magnetic island with the typical O-point in phase with the shards.

Next, simulations will be repeated with the same setup and parameters, but including pre-existing islands of different widths w_i . Section 3.3 investigates cases of injections into the O-point region of the island. Again, we give at first an overview for different amounts of injection material and then focus the investigation on the case with $N_{\text{SPI}} = 6 \times 10^{20}$. After that, simulations with different injection phases are analyzed in Section 3.4.

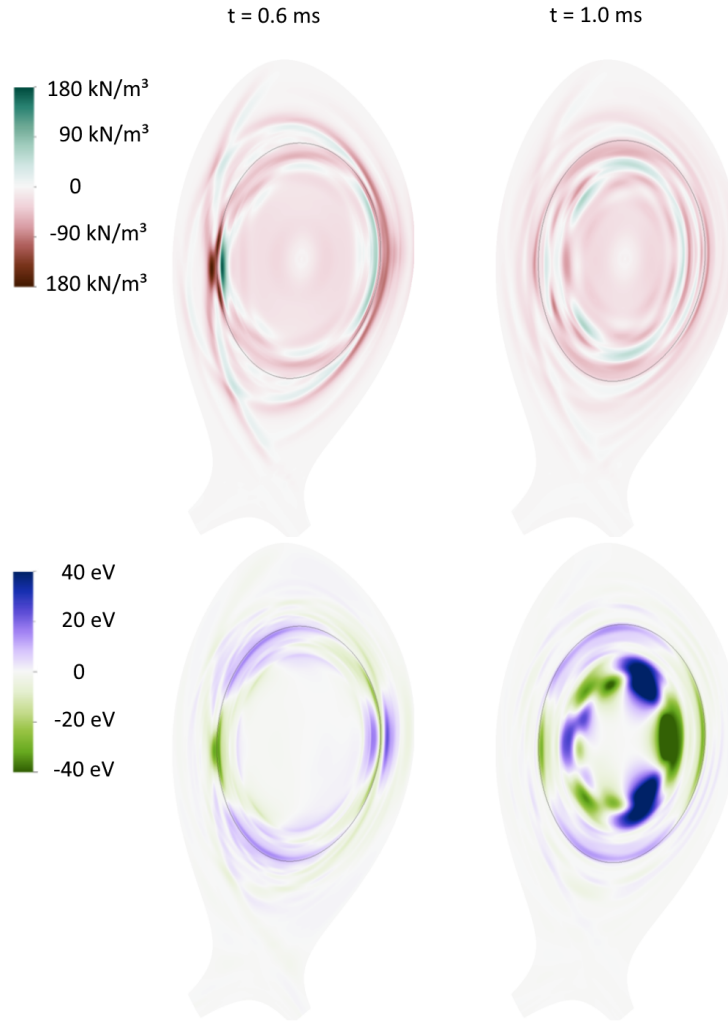


Figure 3.9: Poloidal cuts for $N_{\text{SPI}} = 6 \times 10^{20}$ at $t = 0.6$ ms (left column) and $t = 1.0$ ms (right column), taken at the toroidal position of injection. The enhanced radial pressure gradient ∇p_r (top row) induces a kink parity plasma response. It relaxes and at $t = 1.0$ ms, the temperature perturbation T_e^* (bottom row) dominates, forming a tearing mode by helical cooling.

3.3 Injection into the O-point of a pre-existing 2/1 magnetic island

3.3.1 Impact of a pre-existing island onto MHD dynamics and TQ onset

The comparison in terms of particle and energy content of selected simulations is given in Fig. 3.10. A first sign of the impact of the pre-existing island on the ablation can be detected from the evolution of N_{tot} : after $t = 0.6$ ms, shards penetrate the O-point, in

3.3 Injection into the O-point of a pre-existing 2/1 magnetic island

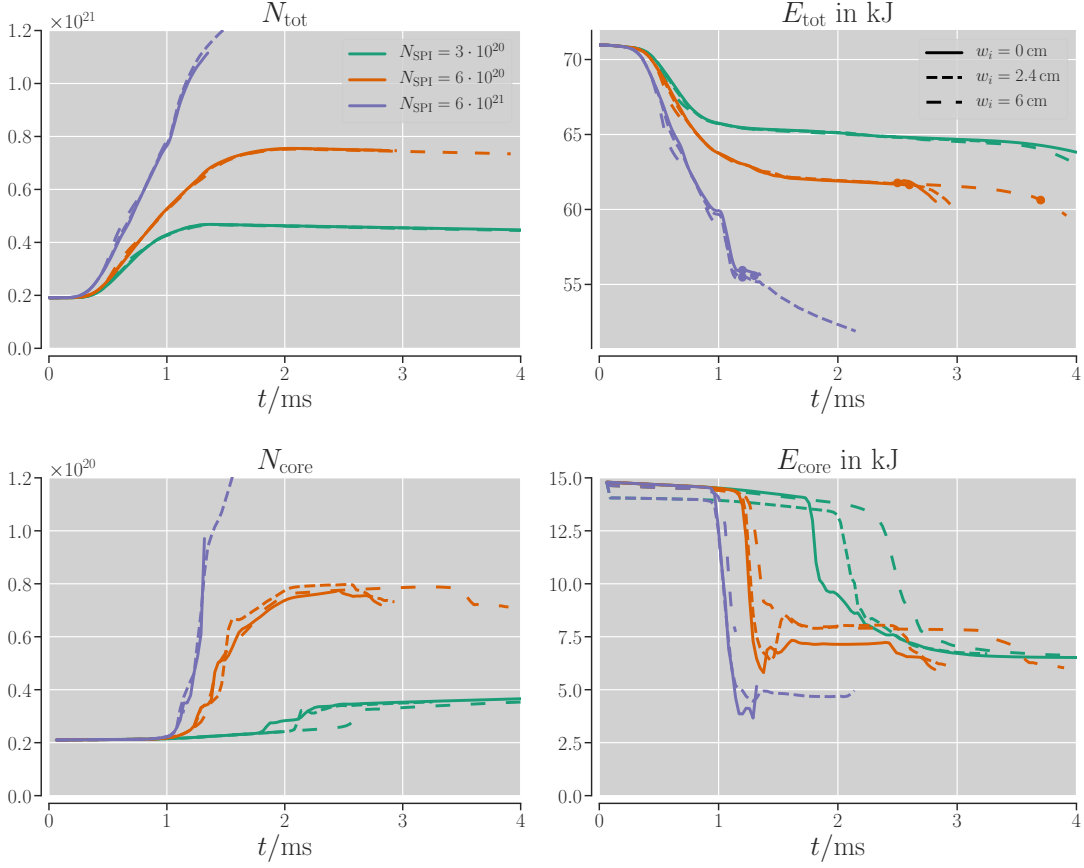


Figure 3.10: Evolution of total (top row) and core (bottom row) particle content (left column) and thermal energy content (right column) for injection without a pre-existing island (solid lines), an initial island width of $w_i = 2.4$ cm (tightly dashed) and $w_i = 6$ cm (loosely dashed). Time points of full stochasticization are marked by circles.

which the temperature is flattened. Because of this, the ablation is enhanced outside the $q = 2$ surface and decreased inside, and consequently, N_{tot} increases faster or slower. This has also an effect on the destabilization of edge instabilities, which can be seen in a different behavior of E_{tot} . We can state, however, that the effect of the pre-existing island is rather small in the first phase of the simulation, as the evolution of N_{tot} and E_{tot} remains in general very similar compared to the cases without pre-existing island, which we call “no pre-existing island cases” from now on (abbreviated as “NI-cases”).

There is a strong effect onto the evolution of the core region, however, except for the case provoking an immediate TQ ($N_{\text{SPI}} = 6 \times 10^{21}$). For $N_{\text{SPI}} = 3 \times 10^{20}$, where the shards do not cause a TQ within the first milliseconds after injection, the onset of the core crash shifts to a later time by 0.3 ms for an island of medium width $w_i = 2.4$ cm and 0.8 ms for the largest considered island with $w_i = 6$ cm. The further evolution of

3 Massive deuterium injection into an ASDEX Upgrade equilibrium

E_{core} is similar again and E_{core} relaxes to 7 kJ after about $t = 3$ ms. This behavior is an indication that injection parameters, that are not sufficient to trigger a TQ, would still not trigger it even under the presence of a big pre-existing island in case of O-point injection.

For the case of a delayed TQ ($N_{\text{SPI}} = 6 \times 10^{20}$), the onset of the first core crash is only delayed by 0.1 ms for the largest island. Again, E_{core} becomes constant after $t = 1.5$ ms, but at a slightly larger value of 8 kJ independently of w_i . The timing of the FS is however heavily influenced by the pre-existing island. For the case with $w_i = 6$ cm, it occurs eventually with a delay of 1.1 ms at $t = 3.6$ ms. The effect of the smaller island ($w_i = 2.4$ cm) onto the TQ onset time is rather marginal, in contrast.

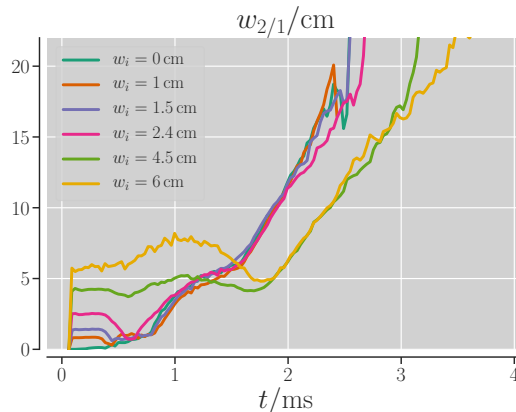


Figure 3.11: Case of $N_{\text{SPI}} = 6 \times 10^{20}$. The evolution of the 2/1 island is hardly affected for small initial island sizes. For larger $w_i > 4$ cm, however, a transient decrease of the island sizes is observed, and the further growth is delayed by about 0.5 ms compared to the no-island case. This delay directly affects the time at which full stochastization is reached. Smaller fluctuation of each line are a non-physical artifact from the calculation of q' .

We want to look now deeper into the dynamics of the island growth for pre-existing islands of different sizes for the setup with $N_{\text{SPI}} = 6 \times 10^{20}$. For this, the evolution of the island sizes of these cases are shown in Fig. 3.11. In every case, the island size stays almost constant in the first phase, up to $t = 0.6$ ms. When shards reach the pre-existing island, a short interplay of the pre-existing island and the pressure-driven kink mode may lead to a transient slight shrinking of the island. After that, all islands begin to grow significantly after $t = 0.8$ ms. The smaller pre-existing islands grow faster than the larger ones and consequently, at $t = 1.2$ ms, all islands with $w_i \leq 4.5$ ms exhibit similar sizes. Immediately after that situation, the first crash sets in all cases: it starts with a highly dynamic $n = 5$ harmonic and, later on, non-linear coupling between all modes of higher order $n = 3 \dots 6$ (see Fig. 3.12). This behavior is rather independent of the initial amplitudes of the $n = 1 \dots 2$ modes, i.e., from w_i .

The cases with smaller initial island widths ($w_i \leq 2.4$ cm) do not differ much from the NI-case after the first crash. They have similar growth rates, show strong mode

3.3 Injection into the O-point of a pre-existing 2/1 magnetic island

coupling in the later phase (see Fig. 3.12, left) and the FS sets in for each case around $t = (2.6 \pm 0.2)$ ms. This is just ≈ 0.1 ms later than in the NI-case. In contrast, the large islands ($w_i = 4.5$ cm and $w_i = 6$ cm) provide a large deviation from the NI-case. There, the $n = 1$ energy (see Fig. 3.12, right) and the island sizes decrease transiently during and shortly after the first core crash ($1.2 \text{ ms} < t < 1.8 \text{ ms}$), i.e., during a first burst of MHD activity in the core region. Even though the growth starts again after that, the preceding impact has an impact on the latter course of the dynamics: Due to the decrease of the $n = 1$ amplitude itself and the associated delay, only at 3.2 ms, the second crash occurs. The mode coupling is fairly weaker than in the NI-case and consequently, modes of higher n reach only much smaller amplitudes. Because of this, this crash does not trigger a FS, which only happens at $t = 3.6$ ms as a third crash. We find, that for all cases, a critical island width of ≥ 17 cm is reached at the time point of FS. We remark, that this island width can not be determined from Poincaré to this point anymore, due to strong stochastization. Hence, we refer to the estimation of the island width based 2/1 component of the poloidal magnetic flux at the $q = 2$ surface (see Eq. 3.1.1).

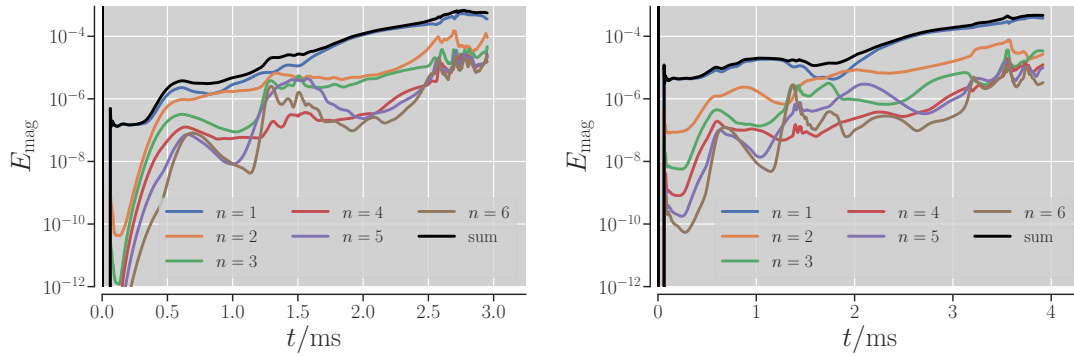


Figure 3.12: Magnetic energy perturbations are plotted for the case with $w_i = 2.4$ cm (left) and $w_i = 6$ cm (right). The evolution of the energies is only weakly affected by small initial islands compared to the case without pre-existing island discussed in Section 3.2 and the non-linear coupling during the first crash is still very pronounced. For $w_i = 6$ cm, however, the $n = 1$ harmonic decays during and shortly after the first crash, which delays the growth of the $n = 1$ perturbation to the amplitude needed for the TQ onset.

The main reason of the delay of FS is the decay of the $n = 1$ mode after the first crash, which is reflected by the evolution of $E_{\text{mag},1}$, as well as in $w_{2/1}$. Therefore, it needs a deeper analysis, which is documented in Section 3.4, where comparisons with other important cases are given as well. In the following Subsection, we will investigate the O-point injection cases with $w_i = 2.4$ cm or $w_i = 6$ cm and $N_{\text{SPI}} = 6 \times 10^{20}$ further. From now on, “O-point injection cases” are abbreviated as “OI-cases”.

3.3.2 Detailed analysis of the dynamics

After examining the overall differences between OI- and NI- cases, we dive now deeper into the details of the OI-cases. Again, we look into a time series of Poincaré plots to study the evolution of the magnetic topology (Fig. 3.13). The general dynamics after the first crash in an OI-case with small $w_i = 2.4$ cm do not differ significantly from the NI-case and the timing of FS remains unaffected. Nevertheless, it is worth to look at the deviating behavior in the early phase ($t < 1$ ms) of the simulation. When the shards are close to the $q = 2$ surface (around $t = 0.5 \dots 0.8$ ms) in the case with $w_i = 2.4$ cm, an interplay between the pre-existing island and the pressure perturbation kink mode occurs. Consequently, the pre-existing 2/1 island breaks up, and a 4/2 mode is formed. One X-point is in phase with the shards and probably generated by the kink mode, just like the X-point of the 2/1 mode in the early phase of the NI-case. After the shards have entered the $q = 2$ surface at $t = 1.2$ ms, the 4/2 mode disappears and the 2/1 mode reforms with a toroidal phase as before: the O-point is again in phase with the injection location. In a former simulation of neon MGI, which was applied to a plasma with a pre-existing 2/1 island (Ref. [91]), a similar observation of a transient 4/2 island was made. As pointed out before, the further evolution remains similar: flux surfaces in the core reform after the first crash, and outer regions become more stochastic ($t = 1.7$ ms). At $t = 2.6$ ms, FS is reached. We conclude, that the small island $w_i = 2.4$ cm, has only an impact on the magnetic topology in an early phase and the further evolution remains virtually unaffected. As a result of the interplay of the shard induced-pressure perturbation and the pre-existing tearing mode, the 2/1 disappears transiently, which makes the underlying 4/2 structure visible. When shards enter the $q = 2$ surface and helical cooling by the shards becomes the dominant island drive, the 2/1 is regained with O-point in phase with the shards (see also Section 3.2).

3.3 Injection into the O-point of a pre-existing 2/1 magnetic island

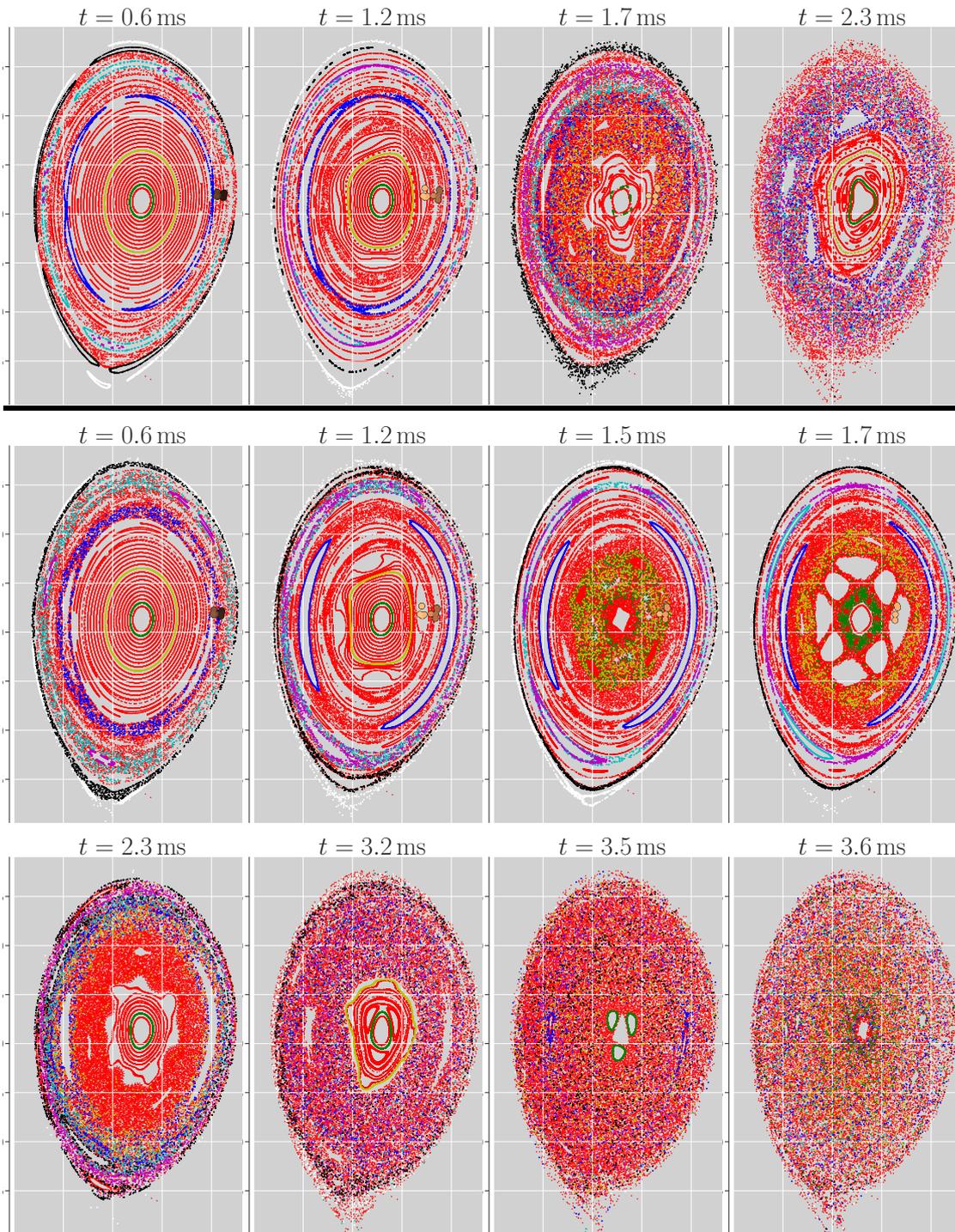


Figure 3.13: Cases with $N_{\text{SPI}} = 6 \times 10^{20}$. Poincaré plots at several time points for $w_i = 2.4$ cm (top) and $w_i = 6$ cm (middle and bottom).

3 Massive deuterium injection into an ASDEX Upgrade equilibrium

The far larger effect of a large pre-existing island ($w_i = 6$ cm) on the plasma dynamics is also reflected in the regarding time series of Poincaré plots, given by Fig. 3.13. The distinct mode structure from the pre-existing island disappears, when the shards approach the $q = 2$ surface and instead, we see a stochastization region in its vicinity ($t = 0.6$ ms). In the following, the island re-establishes and increases in size up to $t = 1.2$ ms. The topology in the inner region ($\Psi_N < 0.3$) is still not affected by the island at this point and similar to the NI-case: It becomes nearly fully stochastic at $t = 1.5$ ms, which is in line with the observation, that the growth rates of the magnetic energies of higher order ($n > 3$) is similar in all OI-cases during the first crash. These modes driver the stochastization of the core. Hence, with decay of these modes, after the crash, the flux surfaces in the inner region reform. In parallel, the 2/1 island decreases and falls back to its initial size $w_{2/1} \approx 6$ cm at $t = 1.8$ ms. Similar to the NI-case, the plasma stochastizes from outer to inner layers from now on, and only remnants of the 2/1 and 3/1 islands are identifiable at $t = 3.2$ ms. However, flux surfaces for $\Psi_N < 0.1$ remain intact in the second crash and FS is not yet reached. They fully vanish only at $t = 3.6$ ms in a third crash. The prolongation of the final phase of the dynamics up to the FS seems to be a feature of the OI-case with a large pre-existing island. Due to its softening effect on the whole dynamics, it is harder to reach FS, which now only happens more than 1 ms later than in the NI-case.

Turning away from the discussion of the change in the magnetic topology of OI-cases, we now discuss the effect of the injection on the density, temperature and pressure profiles as shown in Fig. 3.14 for the case with $w_i = 6$ cm (we will only discuss this case in the following), which can be compared to Fig. 3.6 of the NI-case. In the initial state, a pronounced flattening of temperature and pressure profiles due to the pre-existing 2/1 island is visible. The $q = 2$ surface is located on the midplane at $R = 1.25$ m and $R = 2.01$ m. When that surface stochastizes temporarily at $t = 0.6$ ms, this flattening degrades. Because of this, the situation of the temperature and density profiles shortly before the first crash ($t = 1.2$ ms) is very similar across NI- and OI-cases. The first crash itself is qualitatively similar, as well: the temperature in the center drops rapidly and a hollow pressure profile occurs. However, also this core crash is less violent in the OI-case with $w_i = 6$ cm, discussed here. The temperature and the pressure in the core does not drop as hard as in the NI-case. This is in line with the observation, that, after the first crash, E_{core} in the OI-case is larger than in the NI-case (see Fig. 3.10). Also, the T_e inside $q = 2$ flattens around 250 eV only at $t = 1.8$ ms, which shows that the first crash also takes longer (about 300 μ s) in the OI-case. After the crash, when the magnetic dynamics begin to differ strongly between the NI and the OI-case we so also a bifurcation of the pressure evolution: it remains hollow for a quite longer time, while for the NI-case (or OI-case with small w_i), it starts to relax from $t = 1.8$ ms, until it flattens at FS after 0.7 ms. However, in the OI-case with large w_i , flattening only starts around $t = 2.3$ ms. This is clearly the result of the delayed stochastization of the outer region, as driven from the delayed $n = 1$ mode growth. Indeed, the second crash leads to a nearly completed flattening after $t = 3.3$ ms, except for the core region ($\Psi_N \leq 0.1$), which still shows closed flux surfaces to this point. This small maximum only vanishes at FS ($t = 3.6$ ms).

3.3 Injection into the O-point of a pre-existing 2/1 magnetic island

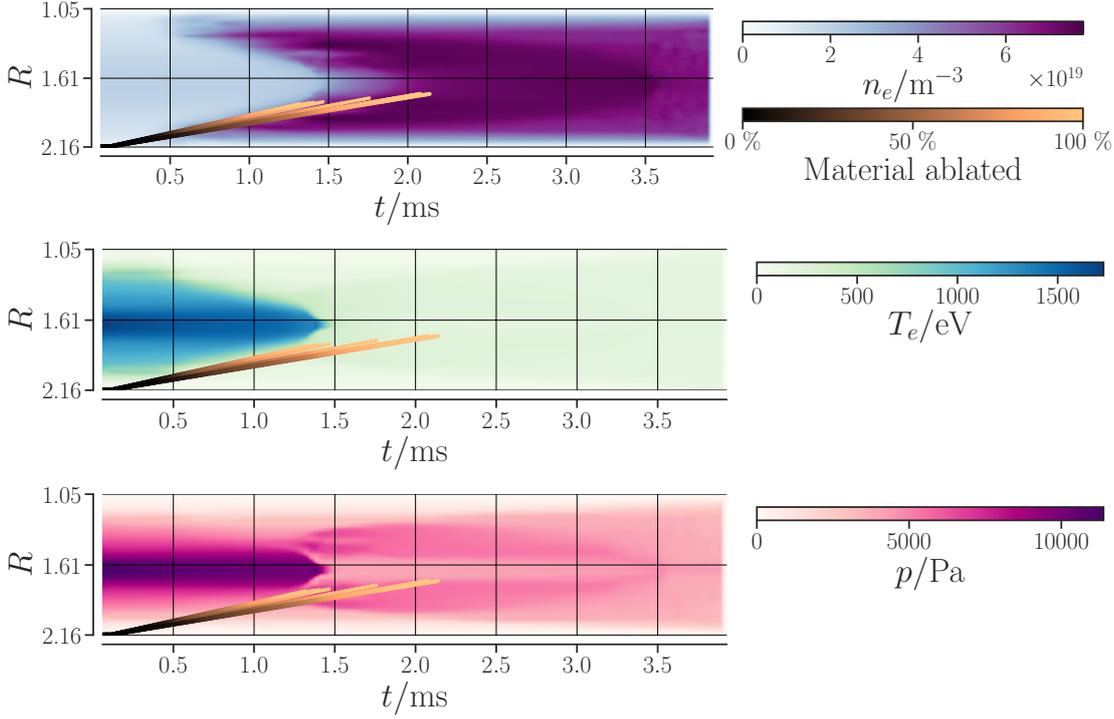


Figure 3.14: Case with $N_{\text{SPI}} = 6 \times 10^{20}$ and $w_i = 6$ cm. Up to the first crash ($t = 1.3$ ms), the evolution of temperature and pressure are very similar compared to cases without pre-existing island (Fig. 3.6) or with a small one. As a result of the delayed mode growth later on, the density profile remains hollow for a longer time and only flattens completely around $t = 3.6$ ms, when full stochasticization is reached.

Before moving over to simulations with injections into the X-point of a pre-existing island in Section 3.4, we discuss the observed behavior of the plasma before the shards enter the $q = 2$ surface: we have seen in the early stage, different dynamics including a 2/1 mode with X-Point in phase of the shards (NI-case), a 4/2 mode (OI-case with small w_i), or a largely stochastic layer around $q = 2$ (OI-case with large w_i). It depends on the amplitudes of initial perturbation $\Psi_{2/1,0}$ and the perturbation $\Psi_{2/1,s}$, which determine the exact behavior of the plasma. $\Psi_{2/1,s}$ is extracted from the NI-cases (with $N_{\text{SPI}} = 6 \times 10^{20}$) and shown in Fig. 3.8. We remark that it is of opposite phase around $q = 2$ relative to the initial perturbation of an OI-case. We assume, that the real perturbation measured in OI-cases in the early is the result of a superposition $\Psi_{2/1}(t) \approx \Psi_{2/1,0} + \Psi_{2/1,s}(t)$.

From this assumption, we can explain the observations: as discussed above, in that early phase, $\Psi_{2/1,s}$ dominantly represents a 2/1 kink with a small tearing component. Its amplitude (at $\Psi_N = 0.65$) is $\approx 2.5 \times 10^{-5}$ Wb at $t = 0.6$ ms with local phase $\phi_{2/1} \approx 0$. The initial $\Psi_{2/1,0}$ of $w_i = 2.4$ cm has a similar amplitude at that radial position (see Fig. 3.15, $t = 0.2$ ms) without a phase jump. As a consequence, both perturbations cancel at $t \approx 0.6$ ms on the $q = 2$ surface and the previously subdominant $\Psi_{4/2}$ component becomes dominant and visible as a 4/2 island structure (see Poincaré plots of Fig. 3.13).

3 Massive deuterium injection into an ASDEX Upgrade equilibrium

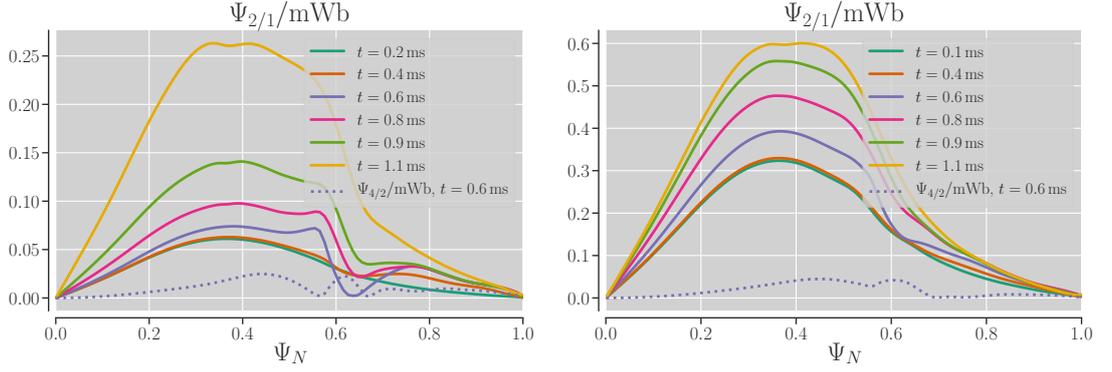


Figure 3.15: Amplitude of the perturbed poloidal flux $\Psi_{2/1}$ of the cases with $w_i = 2.4$ cm (left) and $w_i = 6$ cm (right). When the initial amplitude ($t = 0.2$ ms) close to the $q = 2$ surface matches with the amplitude triggered by only the shards (perturbation of opposite phase), $\Psi_{2/1}$ cancels around $t = 0.6$ ms in the vicinity of $q = 2$ ($\Psi_N = 0.63$), which makes the otherwise sub-dominant 4/2 structure visible for $w_i = 2.4$ cm (see Poincaré plots of Fig. 3.13). Dotted lines show the $\Psi_{4/2}$ component at $t = 0.6$ ms. For $w_i = 6$ cm, the initial $\Psi_{2/1}$ at $q = 2$ is much larger, such that a cancellation is not possible.

For the largest island, $\Psi_{2/1,0} \approx 1.3 \times 10^{-4}$ Wb at $\Psi_N = 0.65$ is five times larger compared to $\Psi_{2/1,s}(0.6$ ms). Consequently, the small tearing component associated with the kink response impairs the initial tearing mode slightly, only. These makes a cancellation impossible. In both cases, helical cooling dominates in the later evolution. Because of this, the tearing mode reestablishes, which leads to the reformation of a 2/1 island with O-point in phase with the shards.

In the next subsection, cases with injections into the X-point and at other phases with respect to the pre-existing island are described first. Second, the mechanisms, how a large pre-existing island affects the timing of FS – hence, the timing of the whole TQ – are discussed.

3.4 Injection in different phases with respect to the island

3.4.1 Observed dynamics and impact onto the TQ

In consistency with the OI-cases, the evolution of total thermal energy and total particle content prior to FS is only weakly affected by the pre-existing island, if we inject into the region of the X-point or other injection phases, too (these “X-point injection cases” are denoted as “XI-cases” from now on). However, an effect on the core quantities (E_{core} and N_{core}) by the X-point injection can be detected. An overview for XI-cases is at different values of N_{SPI} and w_i is given in Fig. 3.16. The following analysis will mainly focus on XI-cases, and later on also deal with other injection angles. In general, we observe a strengthening of the destabilization: For $N_{\text{SPI}} = 3 \times 10^{20}$, E_{core} drops already

3.4 Injection in different phases with respect to the island

at $t = 1.4$ ms in the XI-case with $w_i = 6$ cm, which is 0.3 ms earlier compared to the corresponding NI-case. After that, the dynamics bifurcate from the NI-case: the plasma reaches FS at $t = 2.2$ ms and consequently, also both thermal energies drop at this point. We can derive from this, that a pre-existing island can lower the threshold in the amount of material needed to trigger FS (and the TQ later on), if the material is injected into the vicinity of the island X-point

For $N_{\text{SPI}} = 6 \times 10^{20}$, a clear difference in the dynamics of the first crash between NI- and XI-cases is not visible. However, in the XI-cases, the timing of the FS tends to become earlier with increasing island size: We identify $t = 1.8$ ms for $w_i = 6$ cm from the evolution of E_{tot} . Hence, the FS sets in only 0.6 ms after the first crash, during which the shards are not yet fully ablated. Also, E_{core} reduces much more than in other cases, which implies that the material acts more violent on the core confinement.

A simultaneous strong growth of modes of higher order in the core as well as a strong growth destabilization already in an early phase of the simulation is the reason for the early FS at 2 ms in the XI-case. This can be seen again from several Poincaré plots (Fig. 3.18). Already during the first crash at $t = 1.2$ ms, the outer region ($q > 2$) is much more stochastic compared to that time in the OI-case (compare with Fig. 3.13). $n = 2, 3$ modes inside $q = 2$ get excited from now on, and already at $t = 1.5$ ms, the plasma is almost fully stochastic. Within the next three hundred μs , remaining island remnants disappear. It can be summarized, that for the XI-cases, the first core crash already turns into a FS $t_{\text{FS}} = 1.8$ ms. At this point in time, flux surfaces in the core already reappeared in the OI-case.

The effect of the strong stochastization on temperature and density can be summarized as follows (see Fig. 3.19):

- The electron temperature flattens over a wider radial range, which spans from the core to the $q = 2$ surface, during the first crash ($t = 1.2 \dots 1.5$ ms). It falls down to 180 eV, which is significantly lower than in the NI- or OI-case.
- A monotonous density profile can establish afterward (around $t = 1.8$ ms), as chaotic transport is very efficient in the still stochastic core.
- A hollow pressure profile does only build up shortly, consequently, and E_{core} remains at smaller value.

After discussing, how the plasma is affected by injecting into the X-point of the pre-existing island, we will now also include different injections angles *between* O-point ($\phi_0 = 0^\circ$) and X-point ($\phi_0 = 180^\circ$). Again, the focus is only on cases with $N_{\text{SPI}} = 6 \times 10^{20}$ and $w_i = 6$ cm: the island growth for all considered phases is presented in Fig. 3.17. We see the enhanced island growth of the XI-case, which is rapid from $t = 0.85$ ms to $t = 2$ ms and ends up at above the critical island width of > 17 cm, which leads to FS. The situation is different, when the shards are close to the $q = 2$ surface ($t = 0.6 \dots 0.8$ ms): the island width decreases then, which is in contrast to the dynamics of the OI-case, where the island grows immediately. We can identify two phases from that: in the early phase, the island is larger in the OI-case, than in the XI-case – possibly caused by

enhanced respective reduced helical cooling drive. After a turning point at $t = 1.0$ ms, the island of the XI-case becomes the larger one. The injections at other angles show a consistent picture: the closer the injection is located to the O-point, the later FS sets in. For $\phi_0 = 90^\circ$ the island decreases shortly after the first crash as well ($t \approx 1.1 \dots 1.7$ ms), but not as intense as in the OI-case. An island decrease is not observed for angles closer to the X-point $\phi_O > 90^\circ$.

3.4.2 Mechanisms affecting the TQ time

To close this chapter, the origin of the different behavior of the mode dynamics in the OI- XI- and NI-cases, are discussed with a focus on the different FS times. We remind, that the initial equilibrium is stable against tearing modes and that we have shown on the basis of a test (Fig. 3.7), that the island growth prior to the first crash is mainly driven by helical cooling. If we look on the OI-case for example, we see a strong cooling of the O-point for $t < 1.1$ ms, which triggers the strong island growth by an increase of the helical temperature perturbation (see Fig. 3.21, upper row). While that perturbation is decays in particular during the first crash in all cases, the current profile is modified with growing island size as well, resulting into stabilization or destabilization of the further island evolution. This might explain the differences between these three cases: in the OI-case, a positive current gradient at the $q = 2$ surface stabilizes the mode and is leading, together with the simultaneous decay of $j_{2/1}$, to a decrease of the island size during the first crash (see Fig. 3.20). Around $t = 1.9$ ms, the current gradients changes sign, which leads to a destabilization subsequently. In contrast, in the NI-case, the current density gradient slightly inside the $q = 2$ surface remains negative, hence destabilizing, during the whole first crash.

In the XI-case, a slight decrease of the island is observed initially ($t = 0.6 \dots 1.0$ ms), which can be explained by a reduction of the pre-existing island temperature perturbation through cooling of the X-point (see Fig. 3.21, bottom row). Only after $t = 1$ ms a clear temperature perturbation is visible again. It drives the island growth, as well as its position, when the temperature perturbation rotates clockwise in the poloidal plane and the island follows this. An additional destabilization of the mode is given by the now negative current gradient.

A consistent behavior is observed for other injection angles: in the case with $\phi_0 = 90^\circ$, the current gradient flattens during the first crash, too and gets negative only around $t = 1.7$ ms, i.e., at that time, when the island continues to grow.

Before ending this chapter and turning to simulations involving impurities, a few additional simulations are shown, which shed light on specific details. A detailed discussion is not given here to avoid extending the length of this chapter too much. to verify the effect of different current density evolution on the island dynamics in each case after the first crash, the three runs were restarted from $t = 1$ ms with the configuration of $\eta = \eta_0(T_{e,axi}/T_{e,0})^{-3/2}$, like in Subsection 3.2.2. This isolates again the mode's linear from the helical cooling drive, and it is possible to assume, of the different current profiles really determine the island dynamics. The test shows, that the qualitative trends remain the same indeed: In the NI- and XI-case, the 2/1 island continues to grow –

3.4 Injection in different phases with respect to the island

however, the growth rate is reduced. In the OI-case, the island width remains constant at first and slightly decreases after the first crash. This implies, that the helical drive still plays a significant role for the reduction of the island width in the OI-case.

Also, the sensitivity on the parallel heat conductivity as tested by performing a run with reduced values: a small reduction by a factor of 1.6 does only little affect the dynamics. However, they are distinctly affected by a reduction by a factor of 16. The overall effect of the pre-existing island becomes smaller and the delay of FS in the OI-case is only at 0.2 ms compared to the NI-case. Further, the island decay of the island size during the first crash is reduced.

In summary, it can be said that, depending on the injection phase, the sign of the current gradient around the rational surface changes shortly after the injection in a way that either stabilizes or destabilizes the 2/1 mode during the first crash. In all cases, the gradient finally gets negative some time after the first crash, which causes further mode destabilization and consequently leads to the TQ. The exact origin of the different current profile evolution observed between the cases will require future work.

3 Massive deuterium injection into an ASDEX Upgrade equilibrium

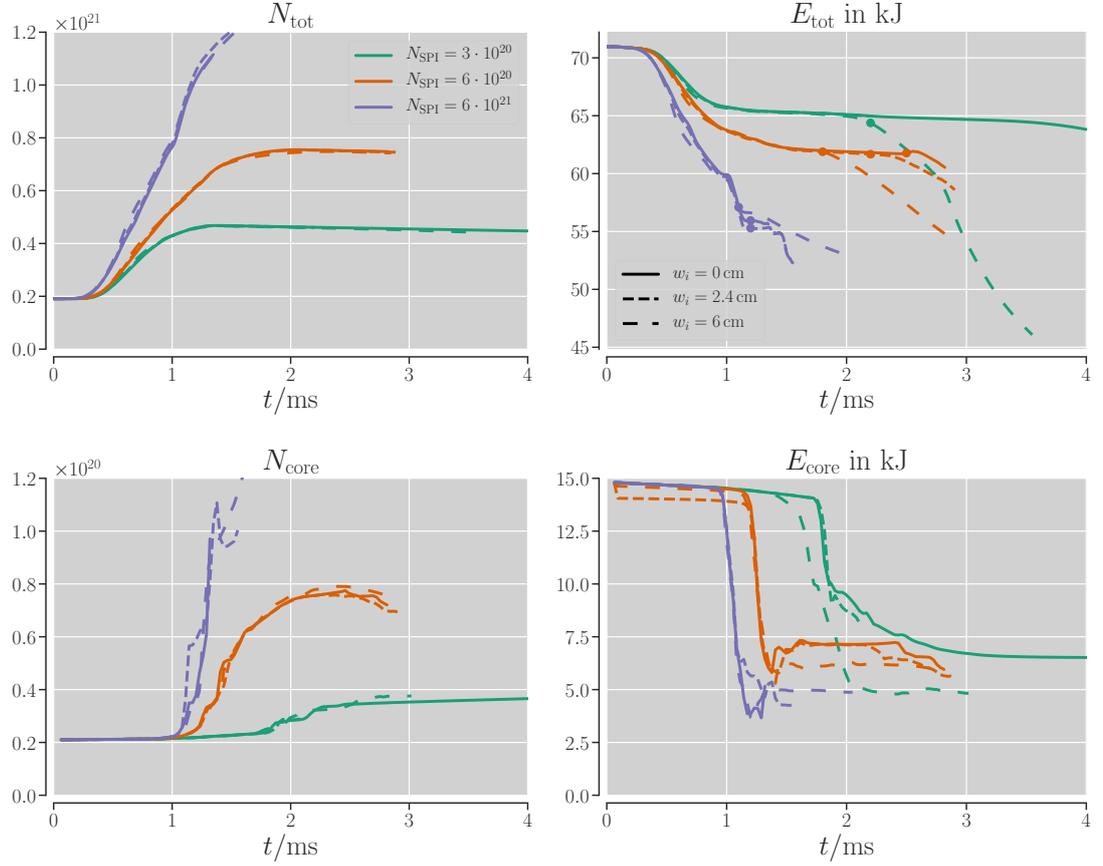


Figure 3.16: Injections into the X-point for different N_{SPI} and w_i . Evolution of total (top row) and core (bottom row) particle content (left column) and thermal energy content (right column) for injection without a pre-existing island (solid lines) and initial island with $w_i = 2.4$ cm (tightly dashed) and $w_i = 6$ cm (loosely dashed). Time points of full stochastization are marked by circles in the right upper plot. In contrast to the injection into the O-point, the core crash (of cases with $N_{\text{SPI}} = 3 \times 10^{20}$) respectively the full TQ (of cases with $N_{\text{SPI}} = 6 \times 10^{20}$) sets in earlier, which becomes in particular visible in the evolution of E_{tot} .

3.4 Injection in different phases with respect to the island

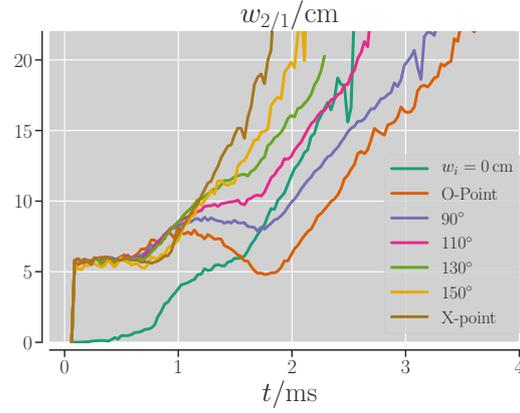


Figure 3.17: Island widths in the cases with $N_{\text{SPI}} = 6 \times 10^{20}$, $w_i = 6$ cm and different injection phase. Injecting into the X-point ($\phi_0 = 180^\circ$) leads to a small island decrease, when shards pass the $q = 2$ surface ($t = 0.8$ ms). After $t = 1.0$ ms, the island growth is clearly enhanced for the XI-case, leading to the TQ occurring earlier than in the other cases.

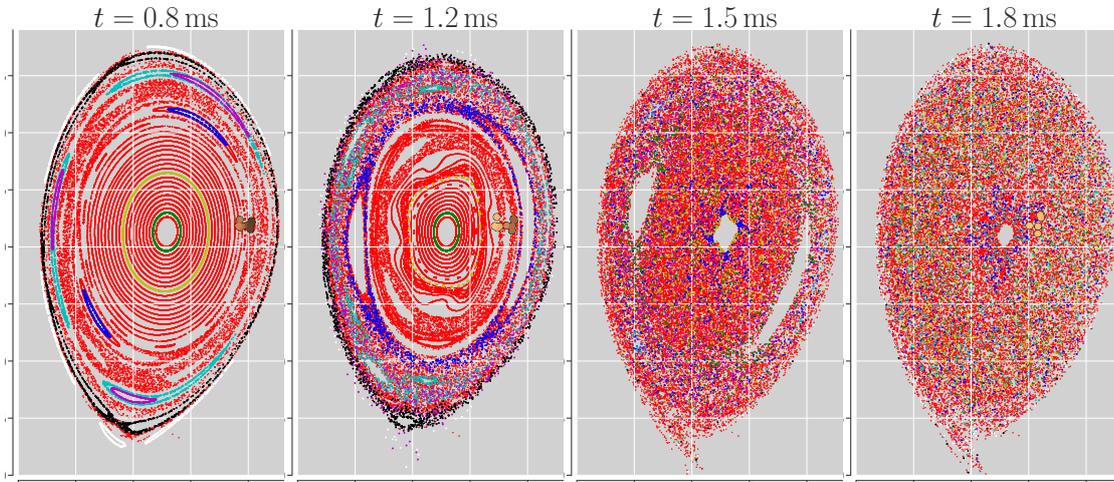


Figure 3.18: Case with $N_{\text{SPI}} = 6 \times 10^{20}$, $w_i = 6$ cm and X-point injection. When shards reach the $q = 2$ surface, the island gets suppressed transiently ($t = 0.8$ ms). Hereafter, its O-point aligns with the shards and begins to grow rapidly. After the first crash at $t = 1.2$ ms, flux surfaces are not reforming ($t = 1.5$ ms) and the plasma becomes fully stochastic around $t = 1.8$ ms.

3 Massive deuterium injection into an ASDEX Upgrade equilibrium

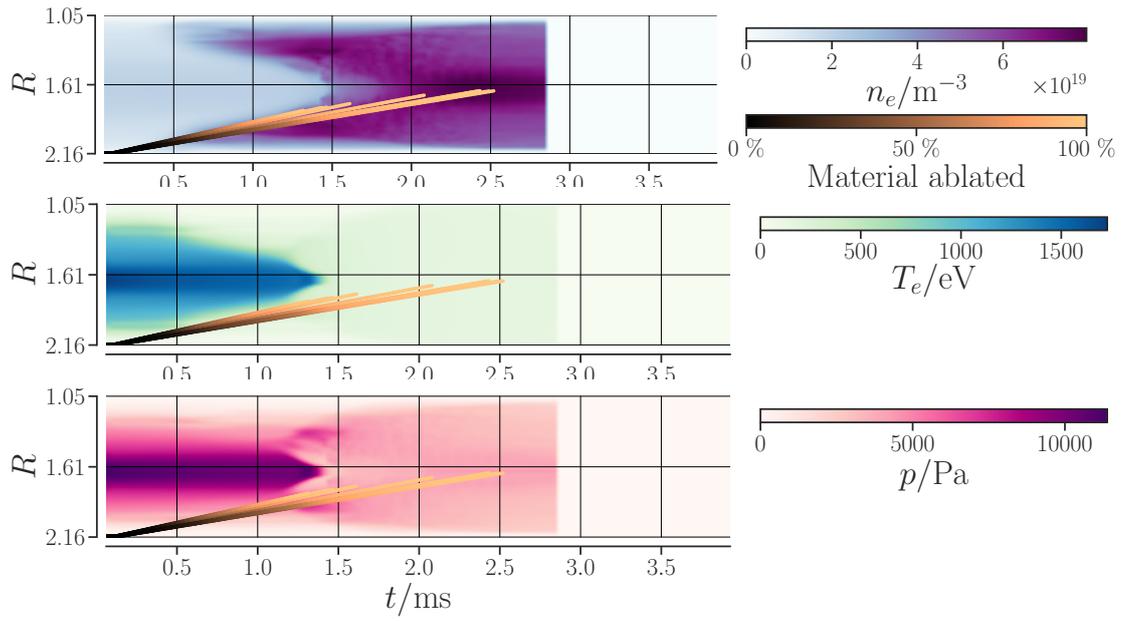


Figure 3.19: Case with $N_{SPI} = 6 \times 10^{20}$, $w_i = 6$ cm and X-point injection. Up to the first core crash, temperature and density behave similarly compared to the runs with other injection phases. However, due to the strong stochasticization after $t = 1.5$ ms related to the rapid 2/1 island growth, the hollow pressure profile is quickly lost as temperature and density profiles flatten already $t = 0.5$ ms after the onset of the first crash.

3.4 Injection in different phases with respect to the island

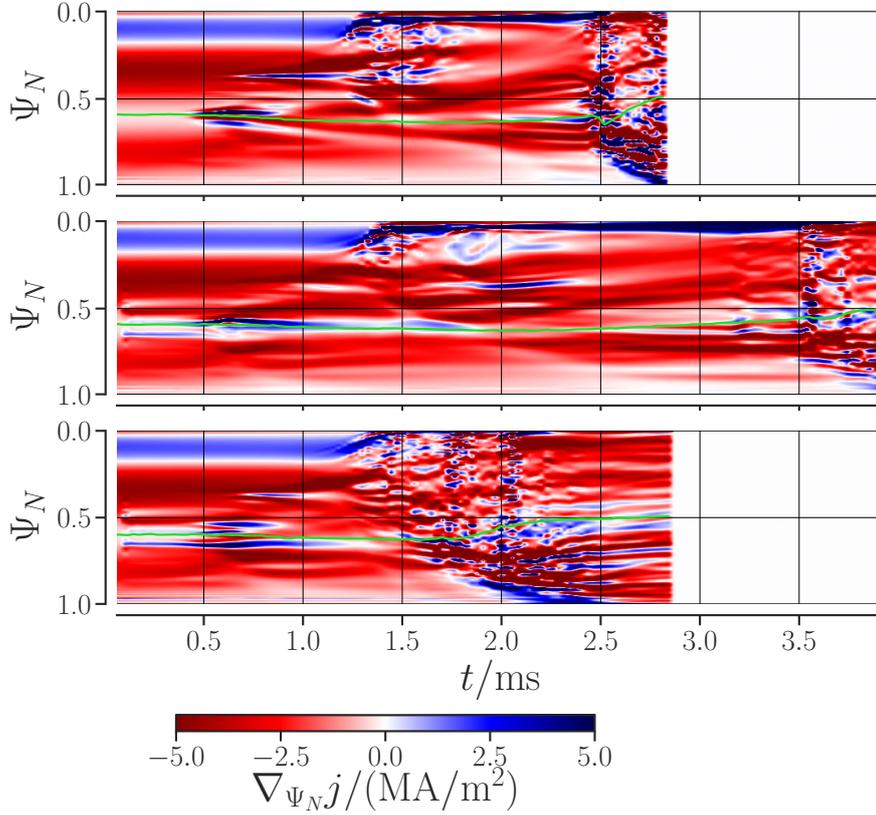


Figure 3.20: Evolution of the radial current density gradient for the NI- (top), OI- case (middle) and XI-case (bottom) with $w_i = 6$ cm. The radial position of the $q = 2$ surface is given in green. In the NI- and XI-cases, $\nabla_{\Psi_N} j$ is always negative (red) slightly inside the $q = 2$ surface after $t = 0.9$ ms (and also positive slightly outside of the $q = 2$ surface in the XI-case), which acts destabilizing. In the OI-case, however, it is flat (white) or positive (blue) at $q = 2$, which stabilizes the mode up to $t = 1.9$ ms.

3 Massive deuterium injection into an ASDEX Upgrade equilibrium

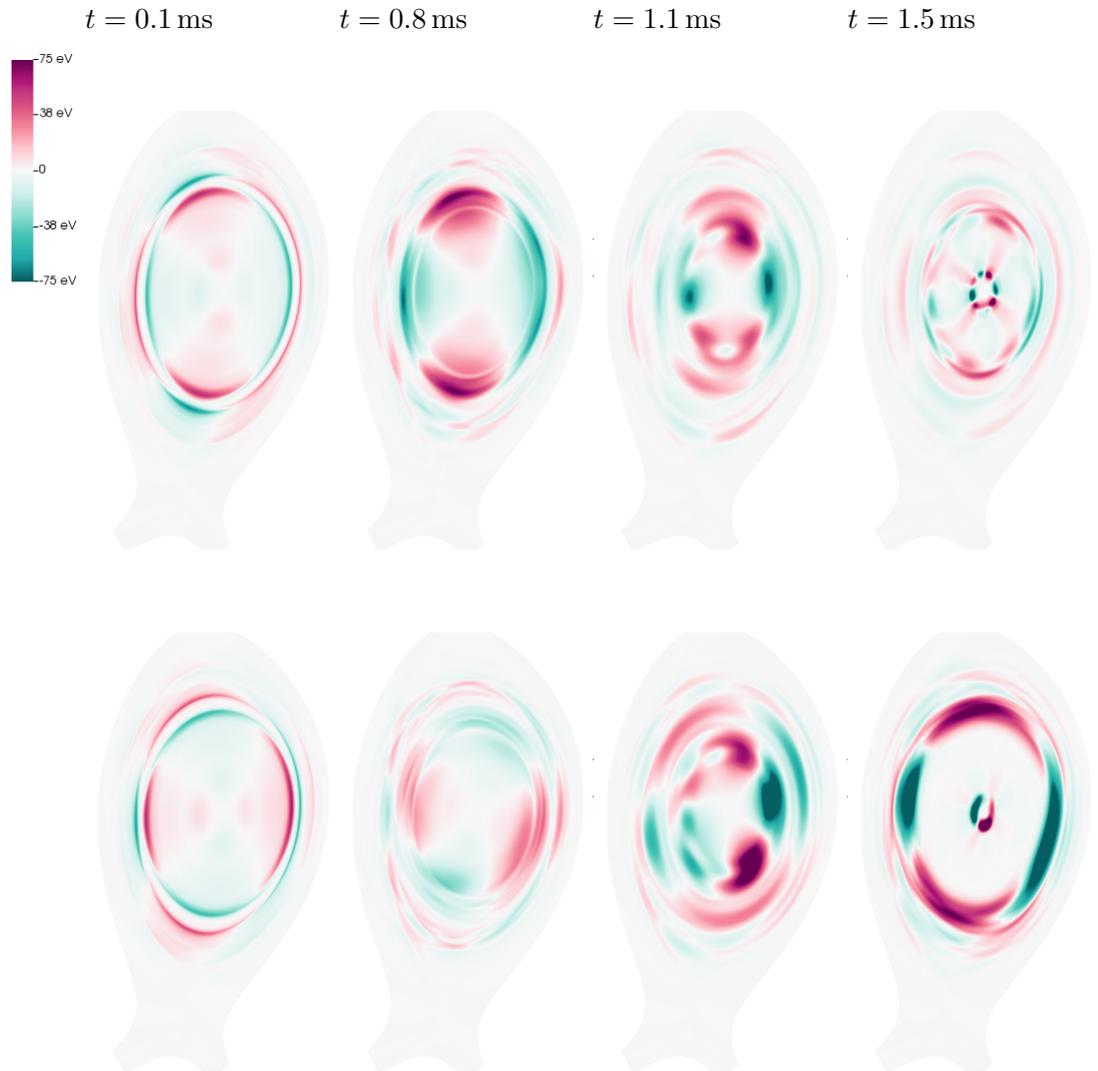


Figure 3.21: Poloidal cuts of the temperature perturbation in the OI-case (top row) and the XI-case (bottom row), taken at the respective toroidal position of injection. As a response to the injection into the O-Point, the 2/1 perturbation at $q = 2$ is amplified, which causes the observed island growth beginning from $t = 0.8$ ms. It decays after $t = 1.0$ ms which is one cause for the island decay up to $t = 1.8$ ms. Injecting into the X-point reduces the initial perturbation in the early phase ($t < 1.0$ ms). Later on ($t = 1.5$ ms), a strong perturbation establishes, which drives the growth and position of the 2/1 island.

4 Role of background impurities in an MHD-active ASDEX Upgrade equilibrium

In the following, the studies will be extended by including background impurity radiation as well as Ohmic heating. Both aspects may play an important role during disruption scenarios, as previously introduced in Subsection 2.1.2. We may expect that with increasing concentration of impurities, the amount of material required to trigger a prompt thermal quench (TQ) decreases. On the other hand, taking Ohmic heating into account will make the plasma more stable against a full thermal quench: after lowering the temperature in the first crash, which we observed in Chapter 3, Ohmic heating is expected to become a significant source for reheating. This might compensate the thermal energy losses and makes it harder to trigger full stochastization and eventually a TQ. We emphasize, here again, that simulations are only performed up to the point of “full stochastization” (FS), where the plasma gets fully stochastic, and the electron temperature flattens below 100 eV. In a real disruptive scenario, impurities may drive the plasma into a thermal collapse later on, where temperatures drop to the range of 1 eV. Thermal collapse and the successive current quench are not studied in this thesis. We are interested, in this chapter, how impurities (and Ohmic heating) affect the dynamics during the disruption onset.

In this chapter, we investigate both cases without a pre-existing island and with $w_i = 6$ cm. The amount of injected material is set to $N_{\text{SPI}} = 6 \times 10^{20}$ for all simulations. These configurations have been rendered in Chapter 3 as being the most relevant cases.

To study the effect of the Ohmic heating itself, we will perform a series of simulations without any impurities. After that, two different concentrations of argon ($n_{\text{bg,Ar}} = 5\%$ and $n_{\text{bg,Ar}} = 7\%$), as well as two different concentrations of tungsten ($n_{\text{bg,W}} = 0.05\%$ and $n_{\text{bg,W}} = 0.5\%$) are selected. The concentration here refers to as the ratio between the volume averaged deuterium ion density and the background impurity density $n_{\text{bg,Z}}$.

The radiative power P_{rad} (calculated by assuming the volume averaged $n_e = 1.35 \times 10^{20} \text{ m}^{-3}$) for each impurity concentration is given in Fig. 4.1. The larger tungsten concentration of 0.5% was chosen to yield a radiative power in the same order of magnitude compared to 5% or 7% argon (i.e., $\max(P_{\text{rad}}) \sim 0.4 \text{ MW/m}^{-3}$). Argon concentrations of a few percent are usually observable during plasma discharges[92]. We are aware, that this large tungsten concentration is not to be expected during normal operation[93]. However, the realistic values of $\leq 0.05\%$ show nearly no impact onto the dynamics, as discussed later in Subsection 4.2. Selecting the far larger value of 0.5% is not only more interesting from an academic point of view, but it could also represent an extreme case, i.e., a disruption, during which a first wall damage leads to tungsten accumulation.

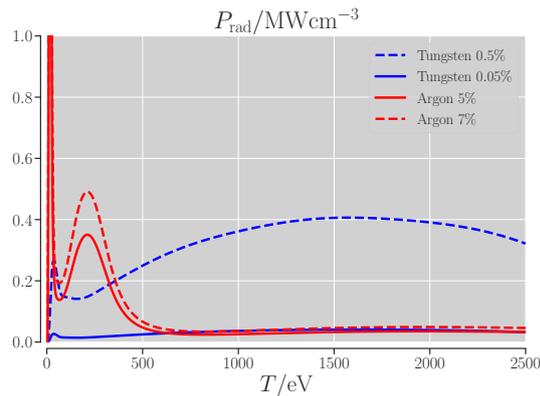


Figure 4.1: Radiative power of tungsten or argon for the concentrations selected in this study. While argon becomes strongly radiating at low temperatures (18 eV and 200 eV), which are reached within the core only during disruptions, tungsten may significantly reduce E_{th} even during normal operation due to a maximum around 1500 eV.

In Subsection 4.1, the role of argon impurities is described intensively. We begin again with a discussion of no pre-existing island cases (NI-cases) and then compare with injections into the O-point (OI-cases) in Subsection 4.1.1: due to Ohmic heating, the threshold in N_{SPI} for triggering a full TQ is increased and the concentration of impurities becomes the critical parameter for TQ triggering. These findings are compared to injections around the X-point (XI-cases) (Subsection 4.1.2). The impurities play a less significant role there.

4.1 Injections with argon impurities

4.1.1 No pre-existing island compared to O-point injection

Including Ohmic heating already affects the simulation prior to the injection. The initial thermal energy content E_{tot} of 71 kJ (compare with Section 3.2) increases slowly by heating of edge regions and converges after around ~ 10 ms at 77 kJ in the case without impurities, if no injection is triggered. The SPI is activated only at $t = 0.6$ ms. This is 0.5 ms later compared to the previous cases from Chapter 3 (in the following, the term “previous cases” always refers to this series of simulations from Chapter 3. Besides, if previous cases are discussed in this chapter, the past tense is used). However, the exact point in time of SPI activation affects the overall dynamics only marginally, as tests have shown.

An overview of NI-cases with different concentrations of argon is given in Fig. 4.2 by solid lines. The evolution of N_{tot} and N_{core} behaves fairly similar compared to the previous sets of simulations: the total particle content starts to increase from $t = 0.8$ ms, i.e., when first shards enter the plasma, and saturates at 7.7×10^{20} after $t = 2.2$ ms. The core particle content increases after $t = 1.5$ ms and in this first sequence, an effect of

4.1 Injections with argon impurities

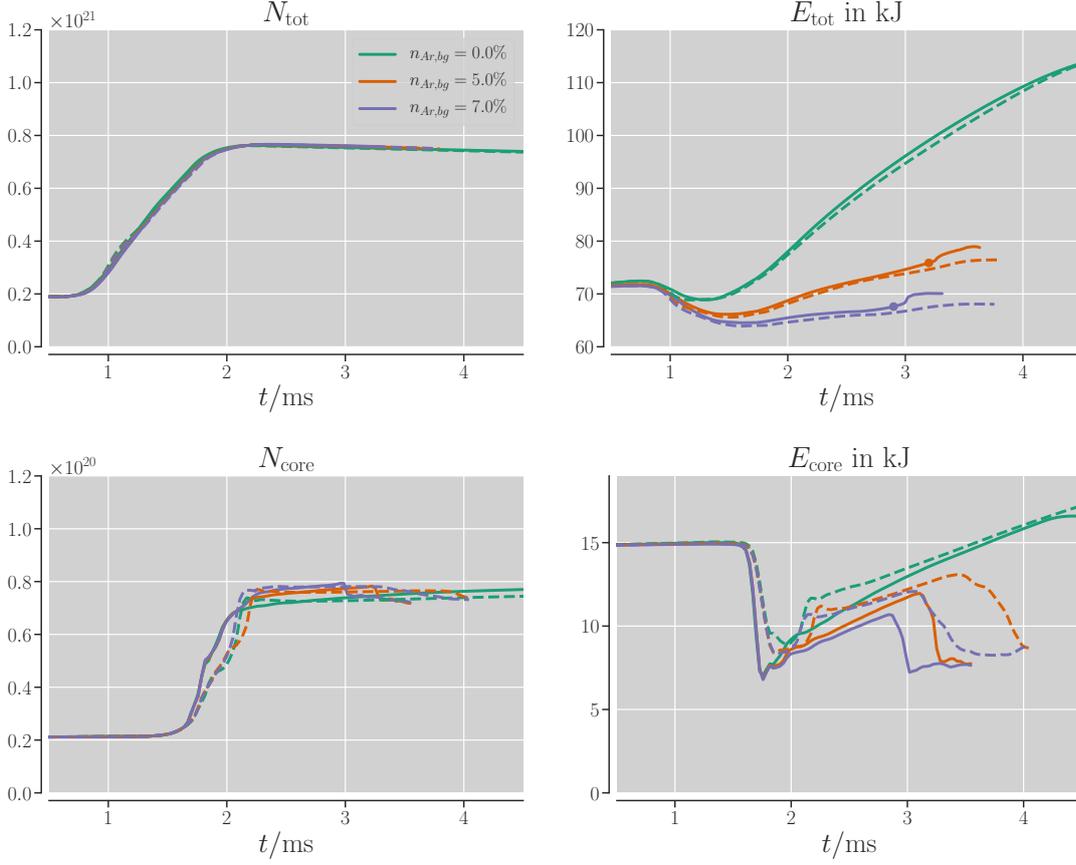


Figure 4.2: Evolution of total (top row) and core (bottom row) particle content (left column) and thermal energy content (right column) for injection without a pre-existing island (solid lines) or large initial island (dashed) and different concentrations of background argon. Time points of full stochasticization are marked by circles. Due to enhanced Ohmic heating after dilution, the whole plasma reheats. In cases without impurities, this reheating prevents the full TQ. In cases with a full TQ, the injection into the O-point continues to have a retarding effect of about ≈ 0.3 ms.

impurities is not visible. Only after saturation around $> 0.7 \times 10^{20}$, we see an apparent bifurcating behavior ($t > 3$ ms): in cases with impurities ($n_{\text{bg,Ar}} = 7\%$ or 5%), full TQs are triggered. These TQs become visible by drops in N_{core} , each caused by the loss of confinement in the core region. The earlier the TQ occurs, the more severe this drop.

The evolution of thermal energies, E_{tot} and E_{core} , are heavily influenced by Ohmic heating. Up to $t = 0.9$ ms, E_{tot} increases only gently, as discussed before. After shards penetrate the plasma and degrade the edge confinement, it decreases by nearly 10 kJ only, which is much less compared to cases of Section 3.3. The reason is the strongly enhanced Ohmic heating due to the drop of the plasma temperatures, that overcompensates the thermal energy losses. In case without impurities, E_{tot} exceeds 100 kJ after two ms,

which is an increase by 40% compared to the initial value. Only for $n_{\text{bg,Ar}} = 7\%$, the gains by Ohmic heating are merely radiated immediately and E_{tot} does not reach its initial value again. In both cases with impurities, there is a sudden, but small increase in E_{tot} around $t = 3$ ms, each coinciding with the point of full TQ. The reason is the further drop of the average temperature due to full stochastization, causing Ohmic reheating. Similar mechanisms are visible for E_{core} : the “first crash” (compare with Section 3.3) sets in at $t = 1.7$ ms, causing a rapid drop in E_{core} , but strong Ohmic reheating of the core region as well. If a TQ sets in, E_{core} breaks down again, in contrast to E_{tot} . This implies, that possible additional Ohmic heating is still clearly dominated by confinement losses or enhanced radiated cooling. This will be investigated further.

From that, we can conclude, that the exact dynamics of the thermal energy content is an interplay between energy losses from confinement degradation, radiative losses and gains from Ohmic heating. Also, we find that the presence of background impurities is a critical condition for the TQ triggering in this setup.

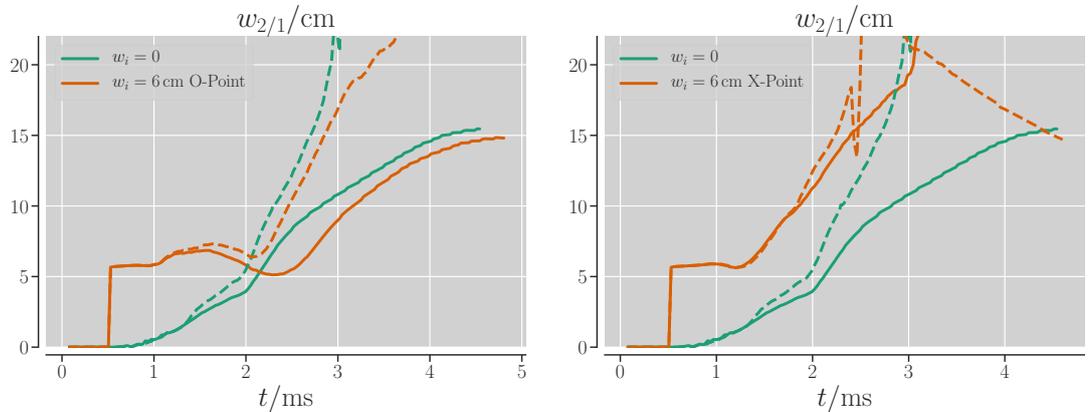


Figure 4.3: Evolution of the 2/1 island width without impurities (solid) or 7% argon (dashed), O-point injection (oher, left), X-point injection (oher, right) or no pre-existing island (black). In cases without full TQ, the island saturates at about 15 cm. The sequence of decreasing island size for O-point injection after $t = 1.5$ ms is clearly reduced by impurities. For X-point injection, the island growth is marginally affected by impurities, which is related to the effect, that only for X-point injection, a TQ can be triggered independently of impurities under the conditions of this setup.

The effect of Ohmic heating Next, we will describe the island size evolution in some selected simulations. To understand the effect of Ohmic heating better, we will at first focus only on those simulations with $n_{\text{bg,Ar}} = 0\%$. The relevant sequences are given in Fig. 4.3 (left, solid lines). By comparing to the respective cases from the previous chapter (see Fig. 3.11), a similar behavior of the 2/1 island can be identified in the first section of the dynamics – apart from the time shift mentioned before: in the NI-case, it is continuously growing during the first crash, and shortly after it ($t = 2$ ms) the growth

rate enhances. For O-point injection, the local maximum is reached at $t = 1.5$ ms and the characteristic transient island decay during and shortly after the first crash sets in. Further dynamics after the first crash are significantly retarded as well. In the further course, the growth rates in both simulations decrease continuously, leading to a saturation of the islands at about ~ 15 cm in each case around $t = 4$ ms. Hence, the critical island size of > 18 cm is not reached, and a full TQ is not triggered. The saturated width in the OI-case is slightly smaller compared to the NI-case. This observation is found in a qualitative sense in all simulations, where no full TQ is reached and seems to be a feature of the O-point injection: it implies, that the pre-existing island has a stabilizing effect even in a configuration, where no full TQ occurs. We conclude, that the evolution of the island width becomes significantly affected by Ohmic heating in both cases – (OI-case and NI-case), but only after the first crash. We now discuss this further on the basis of midplane profiles.

Similarly to the previous simulations, the pressure profile collapses (see Fig. 4.5 and Fig. 4.6) during the first crash and low temperatures of less than 200 eV are reached even within the core. As a consequence, Ohmic heating is heavily enhanced from that point in time, with values of initially more than $P_{\Omega} > 1 \times 10^7$ W/m³ on the inner midplane. Consequently, the pressure within the core but also outer regions (in particular at the $q = 2$ surface) re-establishes. We clearly see, that the crash is more violent in the NI-case, as the core pressure drops temporarily to values of ~ 1000 Pa at $t = 2.2$ ms, which is about seven times smaller compared to that point in the OI-case. The difference is much larger compared to the respective previous cases, and seems to be the result of the following mechanism: first, the first crash is less violent in the OI-case, hence the $q \geq 2$ regions are less ergodized. Therefore, radial thermal transport is reduced compared to the NI-case. Second, ablated material accumulates around the $q = 2$ surfaces and reheats. This results in a very non-monotonous pressure profile from $t = 2.2$ ms to $t = 3.5$ ms with peaks in the core and at both radial positions of the island. A similar effect was also observed in the previous OI-case, for a much shorter time, just before the pressure profile flattened ($t > 1.7$ ms). The Ohmic heating, however, acts strongly onto the regions around $q = 2$, which stabilizes $n = 1$ modes of higher m . This is evident from a series of Poincaré plots (see Fig. 4.4). Around $t = 2.2$ ms, the flux surfaces outside $q = 2$ are fully healed and only for $q < 2$, the plasma is stochastic. This is a huge difference compared to the previous simulations, where the plasma became continuously more stochastic from the edge towards the core in time. Further, for the rest of the simulation, flux surfaces in the core also remain intact, as no high n modes are excited in the core. This is another crucial difference compared to the previous simulations, where these modes played an important role during the onset of full stochastization.

We see, that the pre-existing island reduces the island growth rates (in case of O-point injection) and makes the core crash less violent overall. These effects were also visible in the previous cases, but the difference between the OI- and NI-case is enhanced by the Ohmic heating.

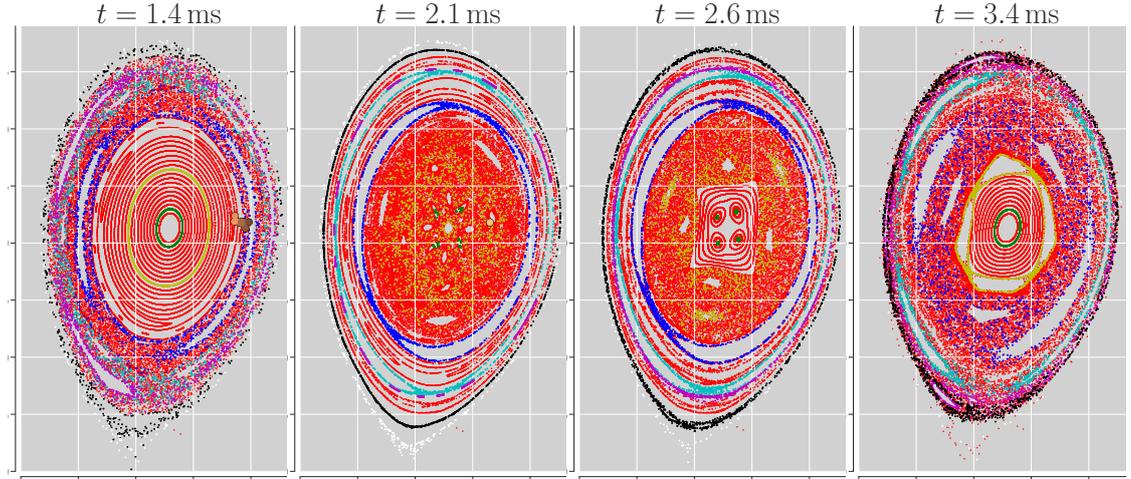


Figure 4.4: O-point injection and no impurities. During the first crash, only the region $q < 2$ becomes stochastic, while flux surfaces in the outer region establish, leading to a regain of thermal insulation. In the further course, due to Ohmic heating, high m/n modes in the core and the 2/1 mode are not as excited enough to trigger a full TQ: flux surfaces in the center remain intact.

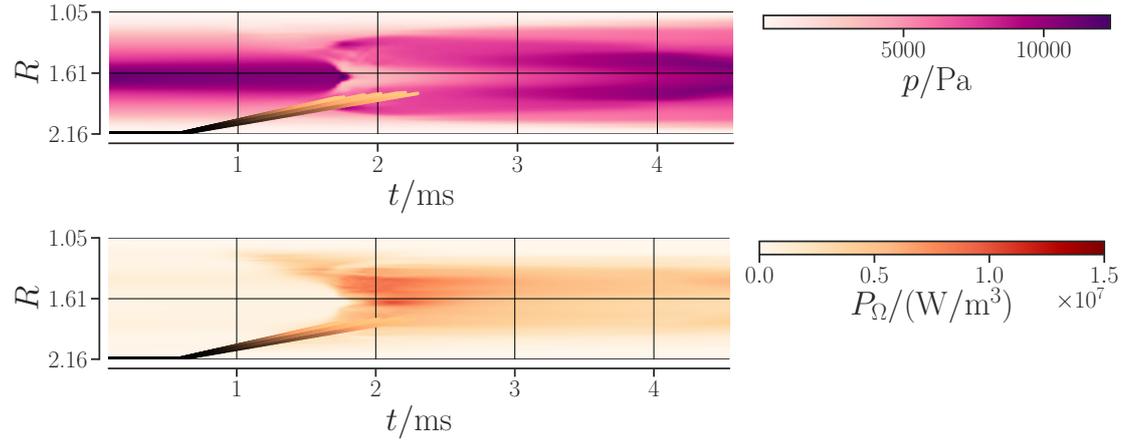


Figure 4.5: Midplane profiles of pressure (top) and Ohmic heating (bottom) are shown for NI-case and no background impurities. During the first crash, Ohmic heating becomes significant. This leads to a heating of the $q = 2$ surface, as well as the core region. As a consequence, pressure in the core is fully regained after $t > 4$ ms.

The effect of 7% argon Having discussed the effects of Ohmic heating alone, we now turn to cases with $n_{\text{bg,Arg}} = 7\%$. In the NI-case, the simulation first behaves similar as without background impurities (see Fig. 4.3), but bifurcates from $t = 1.3$ ms, i.e., when the $q = 2$ surface begins to cool down. Starting from the end of the first crash ($t = 2$ ms), the presence of impurities result in a highly changed dynamics: the island

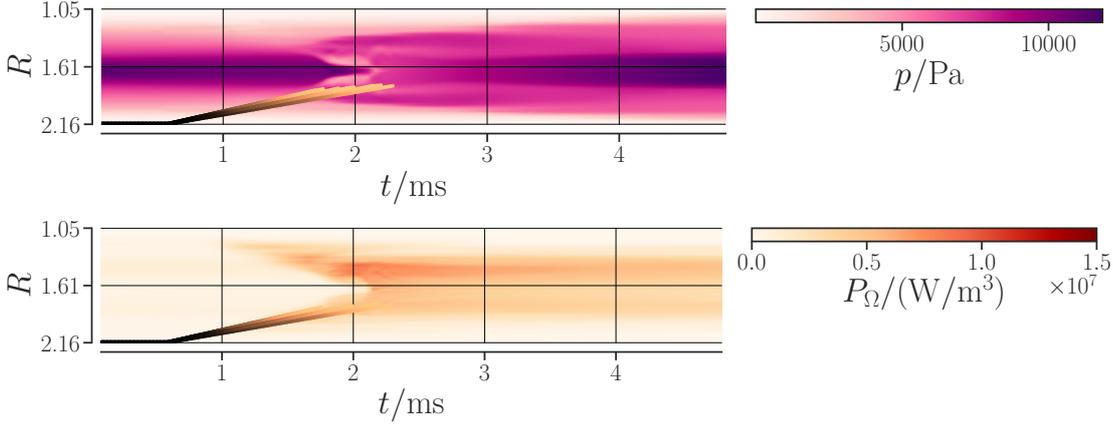


Figure 4.6: Midplane profiles of pressure (top) and Ohmic heating (bottom) are shown for the OI-case and no background impurities. The first crash around $t = 1.8$ ms is less violent, which keeps the pressure in the core at a larger value than in the NI-case. Also, material accumulates within the pre-existing islands, which reheats. This effect is more prone here compared to the cases without Ohmic heating (see Fig. 3.14).

grows with a larger rate and exceeds the width of 18 cm at $t = 2.9$ ms, which is about one millisecond after the first crash. The FS is then reached at a similar time period after injection, as in the previous NI-case, without impurities and Ohmic heating. Also, in case of O-point injection, island growth is enhanced. The case runs into a second crash as well, which is “softer”, however: just prior to reaching the critical island width, the growth rate slows down significantly. The overall properties, that were identified previously – delayed island dynamics and a smaller final island size – are still conserved.

The evolution of the midplane pressure profile of the NI-case (Fig. 4.7) depicts a situation, which is very similar compared to the previous case: a hollow pressure profile establishes at $t = 1.7$ ms, which slowly collapses during more than one millisecond and gets flattened at $t = 3$ ms. Radiative cooling becomes a very active contribution around and outside the $q = 2$ surface from $t = 1.2$ ms on up to about $t = 2.8$ ms, reaching values of about 2×10^7 W/m³. We can assume, that radiative cooling is the main driver for the island growth to reach a critical width and counterbalances the Ohmic heating, which acts in the same order of magnitude. Due to radiative cooling, temperatures below 10 eV for $\Psi_N \geq 0.85$ are found around $t = 2.1$ ms. In the previous simulations, the lowest temperatures were still above 50 eV. A fully radiative collapse – a flattening of the whole temperature profile at a few eV – does not establish also in this setup: radial heat transport from the core to the edge cause reheating and consequently an increase of the temperature back to $T_e = 180$ eV. The temperature might fall back to these low values after the $t = 3.5$ ms, where the simulation ends, and produce a full TQ with temperatures of a few eV. However, as the focus of this work is only the interaction of impurities during the disruption onset up to FS, this is not investigated further.

4 Role of background impurities in an MHD-active ASDEX Upgrade equilibrium

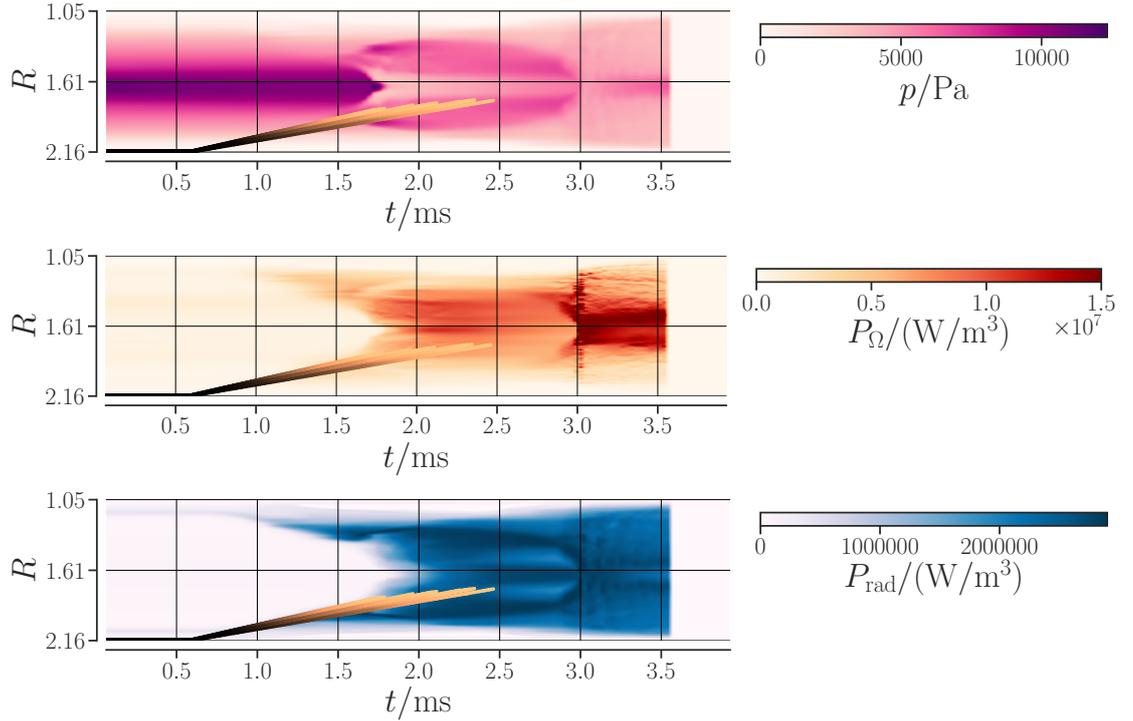


Figure 4.7: Midplane profiles of pressure (top) and Ohmic heating (middle) and radiative cooling (bottom) are shown for NI-case and 7% argon impurities. The Ohmic heating is merely compensated by the radiative cooling. As a consequence, the dynamics are fairly similar as in the case without P_{Ω} or P_{rad} and a full TQ is reached at $t = 3$ ms.

The situation differs, if a pre-existing island is involved: also in this case, the pressure profile decays after the first crash. However, a full flattening of the pressure is not reached, as a peak in p still remains in the core even at $t = 3.5$ ms. Comparing Poincaré plots (Fig. 4.9) of this case with the regarding case without impurities (Fig. 4.4), shows much larger stochastization occurring at the edge after $t = 2.2$ ms. Also, the $q = 2$ region becomes more stochastic. Due to this enhanced radial transport, the pressure drops more intense in the outer region. However, the hot core still remains, which is a large difference after $t = 2.8$ ms the NI-case described in the last paragraphs. We remind that the hot core is a result of a less aggressive first crash, in which the plasma stochastizes less rigidly. The hot core makes full stochastization difficult: the stochastic region penetrates the hot core region from $t = 3.2$ ms. The core begins to cool down rapidly, but this activates a strong burst of Ohmic heating, which counteracts against the cooling, and thus the 2/1 island growth as well: its growth rate reduces as pointed out before. Accordingly, the pressure profile flattens very slowly after that point.

4.1 Injections with argon impurities

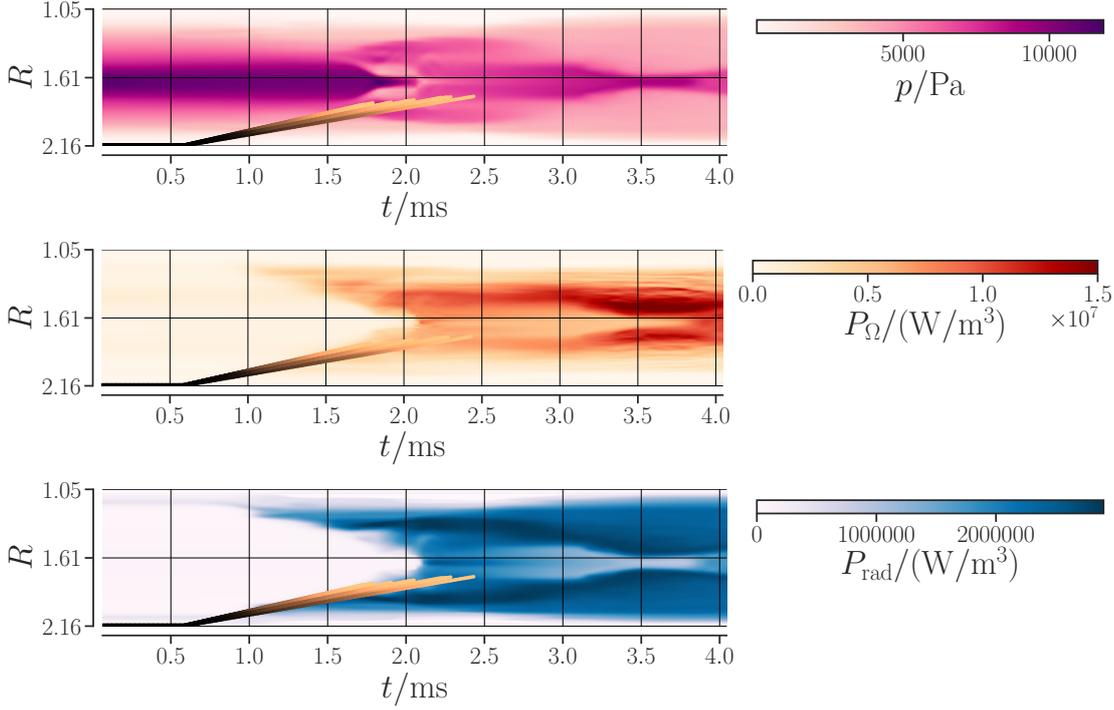


Figure 4.8: Midplane profiles of pressure (top) and Ohmic heating (middle) and radiative cooling (bottom) are shown for the OI-case and with 7% argon impurities. Even though lots of Ohmic heating is radiated away also in this case, it is still dominating in the final phase of the simulation ($t > 3.3$ ms and a full collapse of the pressure profile is not reached).

4.1.2 Injection with different injection angles

After discussing injections into the O-point, we now turn to a comparison of different injection angles. Again, the evolution of particle content is not affected in a relevant sense by the pre-existing island and the evolution of the thermal energies is given in Fig. 4.10. In the absence of impurities, the injection with $\phi_O = 90^\circ$ results in a fairly similar behavior like in the OI-case. The XI-case without impurities however shows a fairly distinct behavior: full stochasticization sets in at $t = 3.1$ ms, i.e., at a similar time like in the NI-case with impurities. The total thermal energy is still increasing at this point, but with a declined growth rate, as Ohmic heating is still dominating stochastic losses. The impact of X-point injection becomes even more distinct in the evolution of E_{core} : it increases after the first crash ($t > 1.7$ ms) but starts dropping after $t = 2.7$ ms. After the full TQ, it stagnates – a behavior seen in most of the cases with full TQ in this series of simulations. From this subgroup of simulations, we see that injecting into the X-point might be a necessary condition for triggering a full TQ. This behavior has also been observed in the previous cases with $N_{\text{SPI}} = 3 \times 10^{20}$ (see Section 3.4).

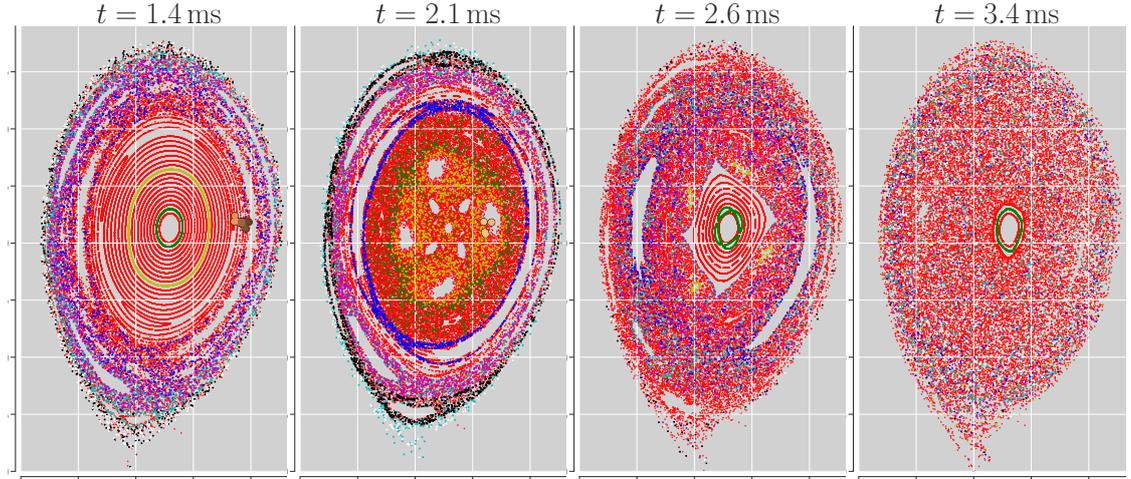


Figure 4.9: O-point injection with $n_{\text{bg,Arg}} = 7\%$. Due to the radiative cooling of the edge, it stays stochastic during the whole simulation sequence, causing a degradation of the heat confinement. Because of this, growth rates of 2/1 mode and other modes of higher order is enhanced and nearly FS is detected during the seconds crash ($t = 3.4$ ms).

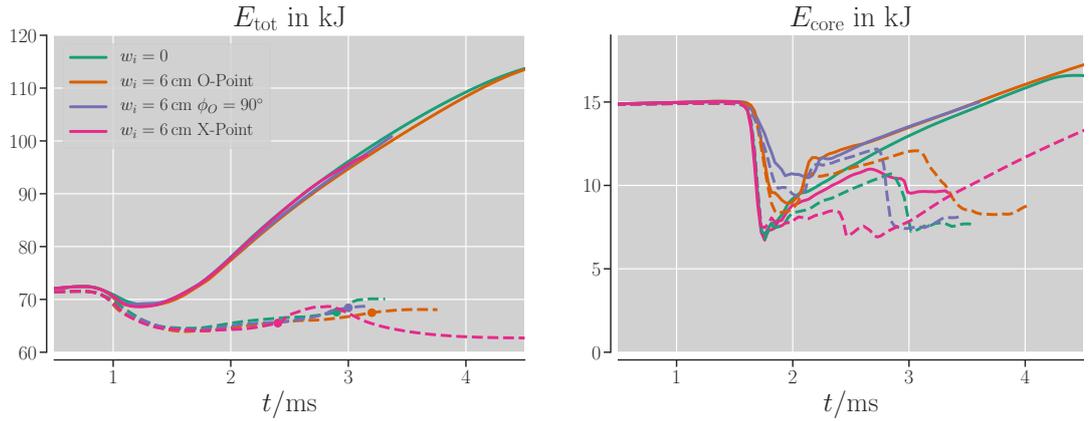


Figure 4.10: Evolution of total (left) and core (right) thermal energy content for injection without impurities (solid lines) and 7% argon (dashed) for different configurations of a pre-existing island. Time points of FS are marked by circles. In cases without impurities, Ohmic reheating prevents the FS. Injection with $\phi_0 = 90^\circ$ (injection between X- and O-point) leads to FS at a similar time point compared to the no-island case. The XI-case clearly accelerates the FS by ≈ 0.5 ms.

The injection in presence of 7% argon background impurities leads to FS in all cases, with an earlier and more violent onset the closer the injection is to the X-point. This is in agreement with the observations from the previous simulations. For injection exactly

between X-point and O-point, FS happens at $t_{\text{FS}} = 2.9$ ms. E_{core} is larger than in the NI-case during $t = 1.7 \dots 2.7$ ms, which indicates, that the first crash is less violent. After FS, the core thermal energies behave similarly in both cases. In the previous case, we have seen a strong premature effect of the X-point injection. This is represented here as well: in the XI-case, FS is observed at $t_{\text{FS}} = 2.4$ ms, which is 0.5 ms earlier than in the NI-case. The first crash is already more violent and leads to a longer lasting collapse of the thermal confinement in the core. Because of this, E_{core} stays at a lower value after the first crash and Ohmic heating has a marginal effect here only. Only, after $t = 2.8$ ms $> t_{\text{FS}}$ it starts to dominate again in the core, when flux surfaces reestablish.

The evolution of the 2/1 island width for X-point injections – with and without background argon – is shown in Fig. 4.3 (right). Impurities have a visible effect on the island size only from $t = 1.9$ ms, which is later than in the other cases. The island has already grown to nearly 10 cm at this point. With impurities, the growth rate is increased and a critical island size of 18 cm is reached in total 1.9 ms after SPI triggering. This is 0.5 ms earlier, than in the case without impurities. We can conclude, that the qualitative dynamics for X-point injections is not heavily changed by Ohmic heating or radiative cooling. In the previous XI-case (see Fig. 3.17), the island showed the same evolution and a reached a size of $w_{2/1} = 18$ cm] about 1.7 ms after the start of the injection. A series of Poincaré plots (see Fig. 4.11) can underline this statement. A difference between these cases (with or without impurities) and the previous XI-case is given in the behavior in the center: previously, no flux surfaces reestablished transiently in the center – a feature, which we see if we include Ohmic heating. If impurities are included as well, this time period in which flux surfaces reestablish is very short (~ 0.3 ms) however, and the dynamics are very similar like in the previous case.

We can summarize, that argon background impurities have a negative impact on the plasma stability in every case and makes the plasma more prone to a TQ. Cases are possible, where the presence of impurities is a necessary condition to trigger the TQ. The stabilizing respective destabilizing effect of an injection into the O-point or X-point of a pre-existing island remains conserved in the presence of argon. Hereby, the “stabilizing effect” can lead to a shift in time of the TQ. Sometimes, the TQ itself is also weakened. If there is already no TQ in the respective NI-case, the island growth in the OI-case is even weaker and the island saturates at a lower width. In the XI-case, the impact of argon is marginal.

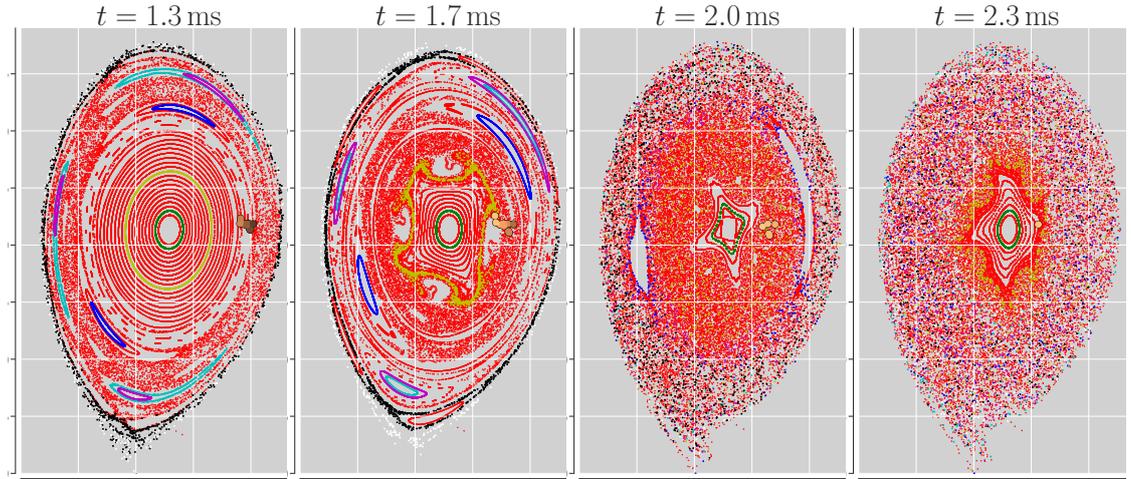


Figure 4.11: XI-case with argon impurities. After injection, the 2/1 island starts to grow, changes its phase and then region $q > 2$ stochastizes. When shards reach the $q = 2$ surface, also the core becomes stochastic gradually. For a short time period ($t = 2 \dots 2.3$ ms), flux surfaces in the center reestablish. Full TQ at $t = 2.5$ ms. For better comparison, the selected times corresponds to Fig. 3.18 with a shift of 0.5 ms.

4.2 The role of tungsten

Additional runs were performed with tungsten background impurities, which are analyzed in a similar approach like argon in the previous Subsection 4.1. Despite a much weaker impact of tungsten to the dynamics compared to argon, we see an overall, qualitative agreement in the observations. Characteristic features of these simulations are presented in the following.

Tungsten, which is never fully ionized at any point in ASDEX Upgrade, may impact the whole temperature profile – including the core – even before the first crash: because of this, a slight decrease not only of E_{tot} , but also of E_{core} just from initializing the simulation is visible for $n_{\text{bg,T}} = 0.5\%$ (see Fig. 4.12). Consequently, E_{core} is about 7% smaller compared to the case without impurities at the beginning of the first crash ($t = 1.7$ ms). The crash itself is more violent, which is visible from a more rapid drop of E_{core} . A large concentration of tungsten is a necessary condition for FS, similarly as observed in the cases with argon. The time of FS can be identified as $t_{\text{FS}} = 4$ ms from the evolution of E_{core} . The impact of smaller concentrations of tungsten is negligible throughout whole simulations, therefore those are not further discussed.

These dynamics are also reflected in the island growth (Fig. 4.13): for the NI-cases, a strong bifurcating evolution between the cases with $n_{\text{bg,T}} = 0\%$ and $n_{\text{bg,T}} = 0.5\%$ is visible after $t = 2$ ms, which is fairly ($\Delta t = 0.8$ ms) later compared to the regarding cases with argon ($n_{\text{bg,Ar}} = 5\%$ or $n_{\text{bg,Ar}} = 7\%$). This is in agreement with the observation, that a significant radiative cooling of the $q = 2$ surface only sets in during (and not

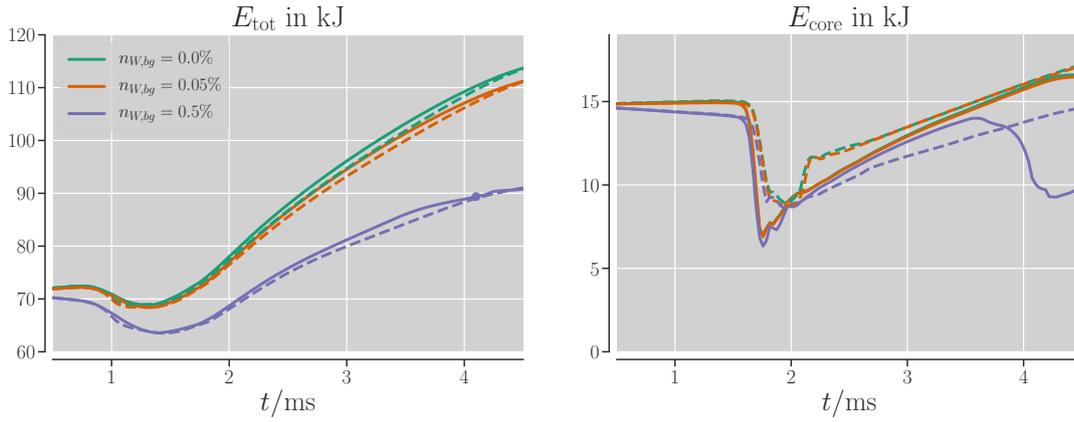


Figure 4.12: Evolution of total (left) and core (right) thermal energy content (right column) for injection without a pre-existing island (solid lines) or O-point injection into a large initial island (dashed) and different concentrations of background tungsten. Time points of full stochasticization are marked by circles. Tungsten only affects the dynamics for a large concentration of $n_{bg,T} = 0.5\%$. While a TQ sets in around $t = 3.6$ ms for this large concentration in the no-island case, the TQ is completely suppressed in the regarding OI-case.

already before) the first crash (see Fig. 4.14), due to an increase of n_e in its vicinity then. With tungsten, the island reaches a width of > 18 cm at $t = 4$ ms. Without, however, the island ends up into a saturation at 15 cm.

With the variant of an O-point injection, this FS is fully suppressed; independent of the concentration of background impurities. In both cases ($n_{bg,T} = 0.5\%$ and $n_{bg,T} = 0.0\%$), the island saturates just before $t = 5$ ms and the evolution are not significantly differing. Indeed, P_{rad} is fairly smaller and less peaked at $q = 2$ in the OI-case compared to the corresponding NI-case. This is rather caused by different densities and not temperatures.

If injecting into the X-point, similar observations can be made: the effect of tungsten on the island growth is nearly negligible, and the plasma runs into FS around $t_{FS} = 3$ ms. Also, evolution of the density and temperature profiles is weakly affected by the tungsten up to the point of FS. It can be summarized, that tungsten plays only a minimal role in case of X-point, but also of O-point injection.

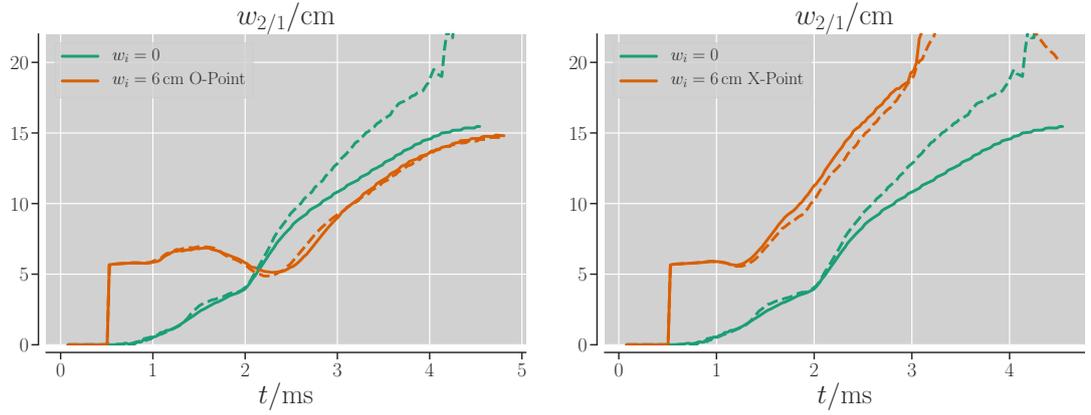


Figure 4.13: Evolution of the 2/1 island width without impurities (solid lines) or 0.5% tungsten (dashed), O-point injection (left) or X-point injection (right). In case of O-point or X-point injection, tungsten has virtually no effect, while it may trigger the FS in the NI-case.

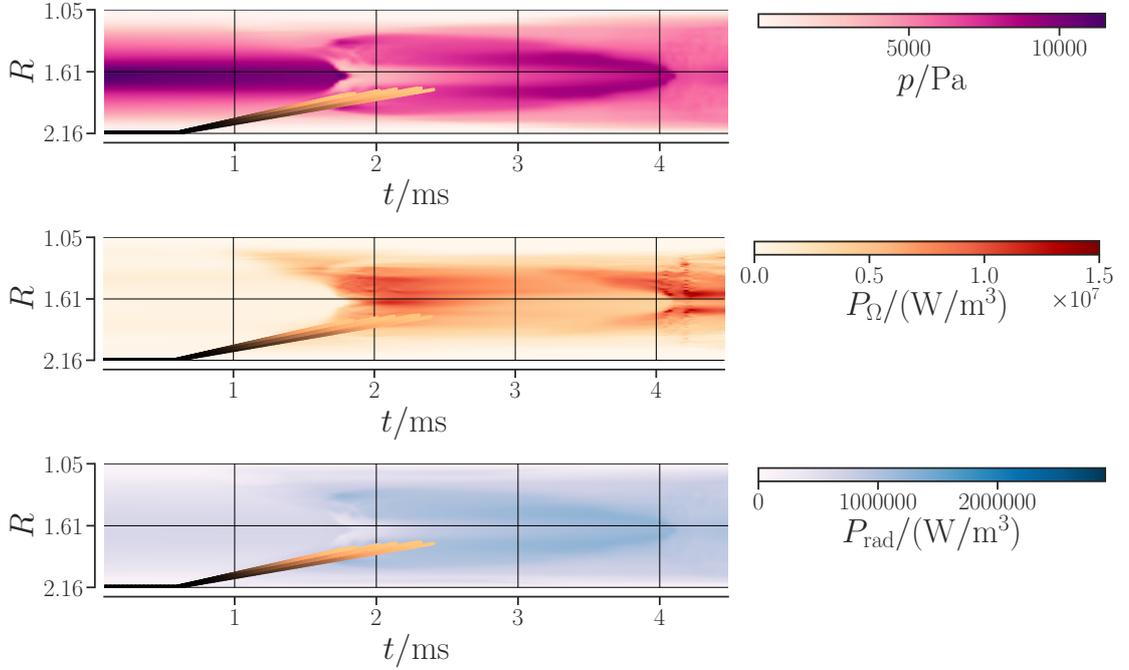


Figure 4.14: Midplane profiles of pressure (top) and Ohmic heating (middle) and radiative cooling (bottom) are shown for the NI-case and with 0.5% tungsten impurities. Tungsten radiates in the core even before the disruption onset, but only at small values. P_{rad} significantly increases around the $q = 2$ only during the first crash ($t = 1.7$ ms) and is still below the level of P_{rad} from argon. The island drive caused by this cooling is sufficient, nevertheless, to drive the plasma into FS at $t = 4$ ms.

5 Conclusion

The central aim of this work was to improve the understanding of the interaction of massive deuterium injection and pre-existing magnetic instabilities in a tokamak plasma. Massive deuterium injection in the form of shattered pellets is the foreseen approach for disruption mitigation in ITER – the last line of defense against the highly critical event of a disruption. During a disruption onset, the plasma usually exhibits magnetic instabilities in the form of tearing modes. The interaction of these instabilities, that pre-exist when the mitigation system is triggered, and the injected material, is a critical detail of disruption mitigation, which is important to understand deeper.

Motivated from this, the non-linear MHD code JOREK was selected to perform a series of simulations of deuterium massive material injection into an ASDEX Upgrade equilibrium. A special feature for most of these simulations was, that the initial plasma already exhibited MHD activity and namely the 2/1 neoclassical locked tearing mode. The exact questions to answer were: what are the effects of pre-existing islands for the TQ formation? Is plasma dilution prior to the TQ viable using deuterium injection also in MHD active plasmas? Which role do play background impurities for this mitigation strategy? To answer these questions in detail, three-dimensional parameter scans were performed, which varied over the amount of material injected, the size of the initial island and the toroidal phase between injection nozzle and island. In an additional study, also concentrations of background impurities – tungsten or argon – were scanned.

We have shown, that in the presence of a large island, the MHD activity triggered by the material injection, can get amplified or suppressed. In case of O-point injection, suppression takes place. In an SPI setup, where the amount of material injected is barely enough to trigger a TQ in the plasma without pre-existing MHD activity, this mechanism is the most prominent. Injecting into the O-point of a pre-existing island with this amount of material might completely suppress the TQ. If the plasma exhibits still a TQ, it will be delayed, these simulations suggest. Also, if the SPI alone does not trigger MHD activity with an amplitude, that would lead to a TQ, this activity is still decreased by the O-point injection. The situation changes, if injection takes place into the vicinity of an X-point. This can lower the threshold in the amount of material needed to trigger the TQ. If we inject with such an amount of material, which is sufficient to trigger a TQ also in the absence of a pre-existing island, the X-point injection makes the TQ more aggressive and it sets in earlier.

This suggests for disruption mitigation, that an injection into the O-point is favorable and should be applied, if possible: the time for dilution is then the longest and the risk is reduced that the mitigation system makes the natural disruption even more aggressive in terms of a rapid TQ and hence increased heat loads. In the best case, only the plasma gets diluted and stays relatively stable – the excitation of MHD activity triggered by

5 Conclusion

the deuterium injection at a certain degree will never be unavoidable. Then, for O-point injection, the time is maximized, in which a second SPI can be triggered for mitigation of heat loads via an impurity pellet.

Another important finding is, that the dilution itself is only hardly influenced by the presence of a pre-existing island. The evolution of the density in the whole plasma behaves similar in all cases (up to the point of the TQ) and the core can always be diluted by the same amount. Only in the vicinity of the 2/1 mode and at the point, when shards pass the O-point of the pre-existing island, small deviations are observable, which are negligible. In general, all these mechanisms stated above are only observable for a sufficiently large pre-existing island. In other words, they can be neglected if the island is observed earlier at a small size, where it is possibly also still rotating.

To summarize this: large pre-existing islands can affect the TQ dynamics and need to be taken into account. However, the general approach of RE mitigation via deuterium mitigation looks still as a viable option, which might be applicable to ITER. Additional studies are necessary, however, to quantify whether sufficient dilution is possible to achieve the goals of suppressing or reducing RE formation.

In the simulations presented here, some restrictions were made: only one specific shard cloud had been investigated in most of the simulations. Also, the neutral gas cloud was assumed to be relatively large, and modelled in simplistic way, which neglects the exact physics of expansion in parallel and perpendicular direction. Even though simple tests had shown, that the exact cloud expansion might not significantly impact the general result, fully resolving the small spatial scales of the shard cloud in non-linear MHD codes is presently not feasible. In future scans, a more precise model should be applied, and from that different scans of the exact shard distribution, size and number of shards should be performed. In light of preparations for ITER, one of the next steps would be to study the dynamics based on ITER equilibria. Here, the 15 MA L-Mode reference scenario, which had already been investigated in [94] could be relevant, as it represents a situation qualitatively comparable to these ASDEX Upgrade studies. All these steps proposed above will strengthen the confidence in the answers found for the scientific questions formulated initially.

Besides of that, the studies should be extended to further questions. For ITER, an SPI system consisting out of 27 injectors is being planned, which allows multiple injections for a more uniform plasma dilution with larger amounts of material. This raises the question, how a multiple SPI-system would react on pre-existing islands. Possibly, the injectors should be triggered intentionally with a small delay, where an O-point injection is triggered at first. This might determine the further plasma dynamics. However, it must also be noted that a certain tolerance in the trigger timing of a few ms must be taken into account. Triggering two injectors *exactly* at the same time would thus be practically impossible anyway. This motivates to investigate the sensitivity towards timing parameters systematically. Also, it needs to be taken into account, first, that the mode might not be locked entirely and still rotates with a few Hz, when the SPI is activated, and second, that magnetic diagnostic systems might not locate the island phase precisely. Because of both, a perfect O-point injection might not be possible practically and further investigations towards the real achievable tolerances are necessary.

Bibliography

- [1] G. Federici. Abstract. *Fusion Engineering and Design*, 178:113103, 2022. URL: <https://www.sciencedirect.com/science/article/pii/S092037962200103X>, doi:<https://doi.org/10.1016/j.fusengdes.2022.113103>.
- [2] A. H. Boozer. Theory of tokamak disruptions. *Physics of Plasmas*, 19(5):058101, 2012. URL: <https://doi.org/10.1063/1.3703327>, arXiv:<https://doi.org/10.1063/1.3703327>, doi:10.1063/1.3703327.
- [3] E. Strait, J. Barr, M. Baruzzo, J. Berkery, R. Buttery, P. de Vries, N. Eidi-etis, R. Granetz, J. Hanson, C. Holcomb, D. Humphreys, J. Kim, E. Kolemen, M. Kong, M. Lanctot, M. Lehnen, E. Lerche, N. Logan, M. Maraschek, M. Okabayashi, J. Park, A. Pau, G. Pautasso, F. Poli, C. Rea, S. Sabbagh, O. Sauter, E. Schuster, U. Sheikh, C. Sozzi, F. Turco, A. Turnbull, Z. Wang, W. Wehner, and L. Zeng. Progress in disruption prevention for ITER. *Nuclear Fusion*, 59(11):112012, jun 2019. URL: <https://doi.org/10.1088/1741-4326/ab15de>, doi:10.1088/1741-4326/ab15de.
- [4] A. H. Boozer. Stellarators as a fast path to fusion. *Nuclear Fusion*, 61(9):096024, aug 2021. URL: <https://dx.doi.org/10.1088/1741-4326/ac170f>, doi:10.1088/1741-4326/ac170f.
- [5] U. Stroth and et al. Overview of ASDEX Upgrade results. *Nuclear Fusion*, 53(10):104003, 2013. URL: <http://stacks.iop.org/0029-5515/53/i=10/a=104003>.
- [6] F. Wieschollek. Non-linear MHD simulation of mode locking and disruption onset. Master's thesis, Technische Universität München, 5 2019. URL: <http://www2.ipp.mpg.de/~mhoelzl/fwieschollek-master-thesis.pdf>.
- [7] A. Bock, E. Fable, R. Fischer, M. Reich, D. Rittich, J. Stober, M. Bernert, A. Burckhart, H. Doerk, M. Dunne, B. Geiger, L. Giannone, V. Igochine, A. Kappatou, R. McDermott, A. Mlynek, T. Odstrčil, G. Tardini, H. Zohm, and T. A. U. Team. Non-inductive improved h-mode operation at asdex upgrade. *Nuclear Fusion*, 57(12):126041, oct 2017. URL: <https://dx.doi.org/10.1088/1741-4326/aa8967>, doi:10.1088/1741-4326/aa8967.
- [8] A. Marinoni, O. Sauter, and S. Coda. A brief history of negative triangularity tokamak plasmas. *Reviews of Modern Plasma Physics*, 5(1):6, Oct 2021. URL: <https://doi.org/10.1007/s41614-021-00054-0>, doi:10.1007/s41614-021-00054-0.

BIBLIOGRAPHY

- [9] J. Wesson. Tokamaks. Clarendon Press, Oxford, 3 edition, 2004.
- [10] T. Hender, J. Wesley, J. Bialek, A. Bondeson, A. Boozer, R. Buttery, A. Garofalo, T. Goodman, R. Granetz, Y. Gribov, O. Gruber, M. Gryaznevich, G. Giruzzi, S. Günter, N. Hayashi, P. Helander, C. Hegna, D. Howell, D. Humphreys, G. Huysmans, A. Hyatt, A. Isayama, S. Jardin, Y. Kawano, A. Kellman, C. Kessel, H. Koslowski, R. L. Haye, E. Lazzaro, Y. Liu, V. Lukash, J. Manickam, S. Medvedev, V. Mertens, S. Mirnov, Y. Nakamura, G. Navratil, M. Okabayashi, T. Ozeki, R. Paccagnella, G. Pautasso, F. Porcelli, V. Pustovitov, V. Riccardo, M. Sato, O. Sauter, M. Schaffer, M. Shimada, P. Sonato, E. Strait, M. Sugihara, M. Takechi, A. Turnbull, E. Westerhof, D. Whyte, R. Yoshino, H. Zohm, D. the ITPA MHD, and M. C. T. Group. Chapter 3: Mhd stability, operational limits and disruptions. Nuclear Fusion, 47(6):S128, 2007. URL: <http://stacks.iop.org/0029-5515/47/i=6/a=S03>.
- [11] M. Lehnen, K. Aleynikova, P. Aleynikov, D. Campbell, P. Drewelow, N. Eidietis, Y. Gasparyan, R. Granetz, Y. Gribov, N. Hartmann, E. Hollmann, V. Izzo, S. Jachmich, S.-H. Kim, M. Kočan, H. Koslowski, D. Kovalenko, U. Kruezi, A. Loarte, S. Maruyama, G. Matthews, P. Parks, G. Pautasso, R. Pitts, C. Reux, V. Riccardo, R. Rocella, J. Snipes, A. Thornton, and P. de Vries. Disruptions in ITER and strategies for their control and mitigation. Journal of Nuclear Materials, 463:39 – 48, 2015. Plasma-surface interactions 21. doi:10.1016/j.jnucmat.2014.10.075.
- [12] P. de Vries, M. Johnson, B. Alper, P. Buratti, T. Hender, H. Koslowski, and V. R. and. Survey of disruption causes at JET. Nuclear Fusion, 51(5):053018, apr 2011. URL: <https://doi.org/10.1088/0029-5515/51/5/053018>, doi:10.1088/0029-5515/51/5/053018.
- [13] F. Turco, T. Luce, W. Solomon, G. Jackson, G. Navratil, and J. Hanson. The causes of the disruptive tearing instabilities of the ITER baseline scenario in DIII-d. Nuclear Fusion, 58(10):106043, sep 2018. URL: <https://doi.org/10.1088/1741-4326/aadbb5>, doi:10.1088/1741-4326/aadbb5.
- [14] V. Klevarová, H. Zohm, G. Pautasso, G. Tardini, R. McDermott, G. Verdoolaege, J. Snipes, P. C. de Vries, M. Lehnen, and and. Validation of a tearing mode locking model using a database of disruptive plasmas at ASDEX upgrade. Plasma Physics and Controlled Fusion, 62(2):025024, dec 2019. URL: <https://doi.org/10.1088/1361-6587/ab5c41>, doi:10.1088/1361-6587/ab5c41.
- [15] A. Bondeson, R. Parker, M. Hugon, and P. Smeulders. Mhd modelling of density limit disruptions in tokamaks. Nuclear Fusion, 31(9):1695, 1991. URL: <http://stacks.iop.org/0029-5515/31/i=9/a=008>.
- [16] R. L. Haye, C. Chrystal, E. Strait, J. Callen, C. Hegna, E. Howell, M. Okabayashi, and R. Wilcox. Disruptive neoclassical tearing mode seeding in DIII-d with implications for ITER. Nuclear Fusion, 62(5):056017, mar 2022. URL: <https://doi.org/10.1088/1741-4326/ac351f>, doi:10.1088/1741-4326/ac351f.

- [17] I. P. E. G. on Disrup MHD and I. P. B. Editors. Chapter 3: MHD stability, operational limits and disruptions. *Nuclear Fusion*, 39(12):2251–2389, dec 1999. URL: <https://doi.org/10.1088/0029-5515/39/12/303>, doi:10.1088/0029-5515/39/12/303.
- [18] R. Fitzpatrick, R. Hastie, T. Martin, and C. Roach. Stability of coupled tearing modes in tokamaks. *Nuclear Fusion*, 33(10):1533–1576, oct 1993. URL: <https://doi.org/10.1088/0029-5515/33/10/i11>, doi:10.1088/0029-5515/33/10/i11.
- [19] I. Krebs, M. Hölzl, K. Lackner, and S. Günter. Nonlinear excitation of low-n harmonics in reduced magnetohydrodynamic simulations of edge-localized modes. *Physics of Plasmas*, 20(8):082506, 2013. URL: <https://doi.org/10.1063/1.4817953>, arXiv:<https://doi.org/10.1063/1.4817953>, doi:10.1063/1.4817953.
- [20] E. Viezzer, T. Puetterich, C. Angioni, A. Bergmann, R. Dux, E. Fable, R. McDermott, U. Stroth, E. Wolfrum, and the ASDEX Upgrade Team. Evidence for the neoclassical nature of the radial electric field in the edge transport barrier of ASDEX Upgrade. *Nuclear Fusion*, 54(1):012003, 2014. URL: <http://stacks.iop.org/0029-5515/54/i=1/a=012003>.
- [21] H. Zohm. *Magnetohydrodynamic Stability of Tokamaks*. Wiley, 2014. doi:10.1002/9783527677375.
- [22] N. C. Logan, E. J. Strait, and H. Reimerdes. Measurement of the electromagnetic torque in rotating diii-d plasmas. *Plasma Physics and Controlled Fusion*, 52(4):045013, 2010. URL: <http://stacks.iop.org/0741-3335/52/i=4/a=045013>.
- [23] R. M. McDermott, C. Angioni, R. Dux, E. Fable, T. Pütterich, F. Ryter, A. Salmi, T. Tala, G. Tardini, E. Viezzer, and the ASDEX Upgrade Team. Core momentum and particle transport studies in the asdex upgrade tokamak. *Plasma Physics and Controlled Fusion*, 53(12):124013, nov 2011. URL: <https://dx.doi.org/10.1088/0741-3335/53/12/124013>, doi:10.1088/0741-3335/53/12/124013.
- [24] M. Nave and J. Wesson. Mode locking in tokamaks. *Nuclear Fusion*, 30(12):2575, 1990. URL: <http://stacks.iop.org/0029-5515/30/i=12/a=011>.
- [25] R. J. Buttery, R. J. La Haye, P. Gohil, G. L. Jackson, H. Reimerdes, and E. J. Strait. The influence of rotation on the betan threshold for the 2/1 neoclassical tearing mode in diii-d. *Physics of Plasmas*, 15(5):056115, 2008. URL: <https://doi.org/10.1063/1.2894215>, arXiv:<https://doi.org/10.1063/1.2894215>, doi:10.1063/1.2894215.
- [26] R. Fitzpatrick. Interaction of tearing modes with external structures in cylindrical geometry (plasma). *Nuclear Fusion*, 33(7):1049, 1993. URL: <http://stacks.iop.org/0029-5515/33/i=7/a=I08>.

BIBLIOGRAPHY

- [27] M. Hölzl. Diffuse Heat Transport across Magnetic Islands and Stochastic Layers in Tokamaks. PhD thesis, Technische Universität München, 2007.
- [28] B. V. Chirikov. A universal instability of many-dimensional oscillator systems. Physics Reports, 52(5):263 – 379, 1979. URL: <http://www.sciencedirect.com/science/article/pii/0370157379900231>, doi:[https://doi.org/10.1016/0370-1573\(79\)90023-1](https://doi.org/10.1016/0370-1573(79)90023-1).
- [29] R. Isler. Impurities in tokamaks. Nuclear Fusion, 24(12):1599, dec 1984. URL: <https://dx.doi.org/10.1088/0029-5515/24/12/008>, doi:10.1088/0029-5515/24/12/008.
- [30] G. Xu, Q. Yuan, K. Li, L. Wang, J. Xu, Q. Yang, Y. Duan, L. Meng, Z. Yang, F. Ding, J. Liu, H. Guo, H. Wang, D. Eldon, Y. Tao, K. Wu, N. Yan, R. Ding, Y. Wang, Y. Ye, L. Zhang, T. Zhang, Q. Zang, Y. Li, H. Liu, G. Jia, X. Liu, H. Si, E. Li, L. Zeng, J. Qian, S. Lin, L. Xu, H. Wang, X. Gong, and B. Wan. Divertor impurity seeding with a new feedback control scheme for maintaining good core confinement in grassy-ELM h-mode regime with tungsten monoblock divertor in EAST. Nuclear Fusion, 60(8):086001, jun 2020. URL: <https://doi.org/10.1088/1741-4326/ab91fa>, doi:10.1088/1741-4326/ab91fa.
- [31] H. P. Summers, W. J. Dickson, M. G. O'Mullane, N. R. Badnell, A. D. Whiteford, D. H. Brooks, J. Lang, S. D. Loch, and D. C. Griffin. Ionization state, excited populations and emission of impurities in dynamic finite density plasmas: I. the generalized collisional-radiative model for light elements. Plasma Physics and Controlled Fusion, 48(2):263–293, jan 2006. URL: <https://doi.org/10.1088/0741-3335/48/2/007>, doi:10.1088/0741-3335/48/2/007.
- [32] D. Hu, E. Nardon, M. Hoelzl, F. Wieschollek, M. Lehnen, G. Huijsmans, D. C. van Vugt, S.-H. Kim, JET contributors, and JOEKE Team. Radiation asymmetry and mhd destabilization during the thermal quench after impurity shattered pellet injection. Nuclear Fusion, submitted, 2020. preprint at <https://arxiv.org/abs/2009.02856>.
- [33] D. Ward and J. Wesson. Impurity influx model of fast tokamak disruptions. Nuclear Fusion, 32(7):1117–1123, jul 1992. URL: <https://doi.org/10.1088/0029-5515/32/7/i03>, doi:10.1088/0029-5515/32/7/i03.
- [34] P. Tamain, E. Tsitrone, P. Ghendrih, J. Gunn, F. Clairet, J. Bucalossi, and B. Pégourié. Thermal interaction of plasma with gas puffing. Journal of Nuclear Materials, 363-365:844–848, 2007. Plasma-Surface Interactions-17. URL: <https://www.sciencedirect.com/science/article/pii/S0022311507001651>, doi:<https://doi.org/10.1016/j.jnucmat.2007.01.235>.
- [35] E. Nardon, D. Hu, M. Hoelzl, D. Bonfiglio, and the JOEKE Team. Fast plasma dilution in ITER with pure deuterium shattered pellet injection. Nuclear Fusion, 60(12):126040, oct 2020. doi:10.1088/1741-4326/abb749.

- [36] B. N. Breizman, P. Aleynikov, E. M. Hollmann, and M. Lehnen. Physics of runaway electrons in tokamaks. *Nuclear Fusion*, 59(8):083001, jun 2019. doi:10.1088/1741-4326/ab1822.
- [37] A. Zappatore, A. Froio, G. A. Spagnuolo, and R. Zanino. 3d transient cfd simulation of an in-vessel loss-of-coolant accident in the eu demo fusion reactor. *Nuclear Fusion*, 60(12):126001, sep 2020. URL: <https://dx.doi.org/10.1088/1741-4326/abac6b>, doi:10.1088/1741-4326/abac6b.
- [38] C. T. R. Wilson. The acceleration of β -particles in strong electric fields such as those of thunderclouds. *Mathematical Proceedings of the Cambridge Philosophical Society*, 22(4):534–538, 1925. doi:10.1017/S0305004100003236.
- [39] M. Lehnen, D. J. Campbell, D. Hu, U. Kruezi, T. C. Luce, S. Maruyama, J. A. Snipes, and R. Sweeney. R&d for reliable disruption mitigation in iter. Technical report, International Atomic Energy Agency (IAEA), Oct 2018. IAEA-CN-258. URL: http://inis.iaea.org/search/search.aspx?orig_q=RN:50052430.
- [40] L. Baylor, S. Meitner, T. Gebhart, J. Caughman, J. Herfindal, D. Shiraki, and D. Youchison. Shattered pellet injection technology design and characterization for disruption mitigation experiments. *Nuclear Fusion*, 59(6):066008, apr 2019. URL: <https://dx.doi.org/10.1088/1741-4326/ab136c>, doi:10.1088/1741-4326/ab136c.
- [41] N. Schwarz, F. Artola, S. Gerasimov, F. Vannini, and M. Hoelzl. The mechanism behind the global wall force reduction in VDEs mitigated with massive material injection, 2023. (in preparation).
- [42] E. M. Hollmann, P. B. Aleynikov, T. Fülöp, D. A. Humphreys, V. A. Izzo, M. Lehnen, V. E. Lukash, G. Papp, G. Pautasso, F. Saint-Laurent, and J. A. Snipes. Status of research toward the iter disruption mitigation system. *Physics of Plasmas*, 22(2):021802, 2015. URL: <https://doi.org/10.1063/1.4901251>, arXiv:<https://doi.org/10.1063/1.4901251>, doi:10.1063/1.4901251.
- [43] E. Nardon, A. Fil, P. Chauveau, P. Tamain, R. Guirlet, H. Koslowski, M. Lehnen, C. Reux, F. Saint-Laurent, and J. Contributors. On the mechanisms governing gas penetration into a tokamak plasma during a massive gas injection. *Nuclear Fusion*, 57(1):016027, nov 2016. URL: <https://dx.doi.org/10.1088/0029-5515/57/1/016027>, doi:10.1088/0029-5515/57/1/016027.
- [44] J. Herfindal, D. Shiraki, L. Baylor, N. Eidietis, E. Hollmann, C. Lasnier, and R. Moyer. Injection of multiple shattered pellets for disruption mitigation in diii-d. *Nuclear Fusion*, 59(10):106034, sep 2019. URL: <https://dx.doi.org/10.1088/1741-4326/ab3693>, doi:10.1088/1741-4326/ab3693.
- [45] S. Jachmich, U. Kruezi, M. Lehnen, M. Baruzzo, L. Baylor, D. Carnevale, D. Craven, N. Eidietis, O. Ficker, T. Gebhart, S. Gerasimov, J. Herfindal, E. Hollmann, A. Huber, P. Lomas, J. Lovell, A. Manzanares, M. Maslov, J. Mlynar,

BIBLIOGRAPHY

- G. Pautasso, C. Paz-Soldan, A. Peacock, L. Piron, V. Plyusnin, M. Reinke, C. Reux, F. Rimini, U. Sheikh, D. Shiraki, S. Silburn, R. Sweeney, J. Wilson, P. Carvalho, and the JET Contributors. Shattered pellet injection experiments at jet in support of the iter disruption mitigation system design. *Nuclear Fusion*, 62(2):026012, dec 2021. URL: <https://dx.doi.org/10.1088/1741-4326/ac3c86>, doi:10.1088/1741-4326/ac3c86.
- [46] S. Park, K. Lee, H. Lee, J. Song, S. Yun, L. R. Baylor, S. J. Meitner, J. Kim, K. Kim, S. Maruyama, M. Lehnen, U. Kruezi, K. Park, and S. Yoon. Experimental results of multiple shattered pellet injection systems in kstar. *Fusion Engineering and Design*, 164:112200, 2021. URL: <https://www.sciencedirect.com/science/article/pii/S0920379620307481>, doi:<https://doi.org/10.1016/j.fusengdes.2020.112200>.
- [47] M. Hoelzl, D. Hu, E. Nardon, and G. T. A. Huijsmans. First predictive simulations for deuterium shattered pellet injection in asdex upgrade. *Physics of Plasmas*, 27(2):022510, 2020. doi:10.1063/1.5133099.
- [48] C. C. Kim, Y. Liu, P. B. Parks, L. L. Lao, M. Lehnen, and A. Loarte. Shattered pellet injection simulations with nimrod. *Physics of Plasmas*, 26(4):042510, 2019. URL: <https://doi.org/10.1063/1.5088814>, arXiv:<https://doi.org/10.1063/1.5088814>, doi:10.1063/1.5088814.
- [49] O. Vallhagen, I. Pusztai, M. Hoppe, S. Newton, and T. Fülöp. Effect of two-stage shattered pellet injection on tokamak disruptions. *Nuclear Fusion*, 62(11):112004, sep 2022. URL: <https://dx.doi.org/10.1088/1741-4326/ac667e>, doi:10.1088/1741-4326/ac667e.
- [50] E. Nardon, A. Matsuyama, D. Hu, and F. Wieschollek. Post-thermal-quench shattered pellet injection for runaway electron seed depletion in iter. *Nuclear Fusion*, 62(2):026003, dec 2021. URL: <https://dx.doi.org/10.1088/1741-4326/ac3ac6>, doi:10.1088/1741-4326/ac3ac6.
- [51] T. Gebhart, L. Baylor, M. Ericson, S. Meitner, A. Qualls, and D. Rasmussen. Recent progress in shattered pellet injection technology in support of the iter disruption mitigation system*. *Nuclear Fusion*, 61(10):106007, sep 2021. URL: <https://dx.doi.org/10.1088/1741-4326/ac1bc4>, doi:10.1088/1741-4326/ac1bc4.
- [52] I. Palermo, R. Garcia, M. Garcia, and J. Sanz. Radiological impact mitigation of waste coming from the european fusion reactor demo with dcll breeding blanket. *Fusion Engineering and Design*, 124:1257–1262, 2017. Proceedings of the 29th Symposium on Fusion Technology (SOFT-29) Prague, Czech Republic, September 5-9, 2016. URL: <https://www.sciencedirect.com/science/article/pii/S0920379617301734>, doi:<https://doi.org/10.1016/j.fusengdes.2017.02.080>.

- [53] L. Hesslow. Kinetic modeling of runaway-electron dynamics in partially ionized plasmas. URL: <https://research.chalmers.se/publication/518256>.
- [54] M. Dibon, P. de Marne, G. Papp, I. Vinyar, A. Lukin, S. Jachmich, U. Kruezi, A. Muir, V. Rohde, M. Lehnen, P. Heinrich, T. Peherstorfer, D. Podymskii, and A. U. Team. Design of the shattered pellet injection system for ASDEX Upgrade. Review of Scientific Instruments, 94(4):043504, 04 2023. URL: <https://doi.org/10.1063/5.0141799>, arXiv:https://pubs.aip.org/aip/rsi/article-pdf/doi/10.1063/5.0141799/16833711/043504_1_5.0141799.pdf, doi:10.1063/5.0141799.
- [55] T. Peherstorfer. Fragmentation analysis of cryogenic pellets for disruption mitigation. URL: https://pure.mpg.de/pubman/faces/ViewItemFullPage.jsp?itemId=item_3475652, doi:<https://doi.org/10.17617/2.3475652>.
- [56] S. Braginski. Transport processes in a plasma. Review of Plasma Physics, 1:205, 1965.
- [57] J. Wesson. Hydromagnetic stability of tokamaks. Nuclear Fusion, 18(1):87, 1978. URL: <http://stacks.iop.org/0029-5515/18/i=1/a=010>.
- [58] H. Grad and H. Rubin. Hydromagnetic equilibria and force-free fields. Technical report, United Nations (UN), 1958. PLASMA PHYSICS AND FUSION TECHNOLOGY. URL: http://inis.iaea.org/search/search.aspx?orig_q=RN:39082408.
- [59] V. D. Shafranov. The stability of a cylindrical gaseous conductor in a magnetic field. The Soviet Journal of Atomic Energy, 1(5):709–713, Oct 1956. URL: <https://doi.org/10.1007/BF01480907>, doi:10.1007/BF01480907.
- [60] V. Bandaru, M. Hoelzl, and K. Lackner. Tokamak plasma equilibrium with relativistic runaway electrons. unpublished, 2021.
- [61] Z. Yoshida. Numerical analysis of runaway tokamak equilibrium. Nuclear Fusion, 30(2):317, feb 1990. URL: <https://dx.doi.org/10.1088/0029-5515/30/2/010>, doi:10.1088/0029-5515/30/2/010.
- [62] F. Troyon, R. Gruber, H. Saurenmann, S. Semenzato, and S. Succi. Mhd-limits to plasma confinement. Plasma Physics and Controlled Fusion, 26(1A):209, 1984. URL: <http://stacks.iop.org/0741-3335/26/i=1A/a=319>.
- [63] F. Wagner, G. Becker, K. Behringer, D. Campbell, A. Eberhagen, W. Engelhardt, G. Fussmann, O. Gehre, J. Gernhardt, G. v. Gierke, G. Haas, M. Huang, F. Karger, M. Keilhacker, O. Klüber, M. Kornherr, K. Lackner, G. Lisitano, G. G. Lister, H. M. Mayer, D. Meisel, E. R. Müller, H. Murmann, H. Niedermeyer, W. Poschenrieder, H. Rapp, H. Röhr, F. Schneider, G. Siller, E. Speth, A. Stäbler, K. H. Steuer, G. Venus, O. Vollmer, and Z. Yü. Regime of improved confinement and high beta

BIBLIOGRAPHY

- in neutral-beam-heated divertor discharges of the ASDEX tokamak. Phys. Rev. Lett., 49:1408–1412, 1982. doi:10.1103/PhysRevLett.49.1408.
- [64] M. Maraschek, A. Gude, V. Igochine, H. Zohm, E. Alessi, M. Bernert, C. Cianfarani, S. Coda, B. Duval, B. Esposito, S. Fietz, M. Fontana, C. Galperti, L. Giannone, T. Goodman, G. Granucci, L. Marelli, S. Novak, R. Paccagnella, G. Pautasso, P. Piovesan, L. Porte, S. Potzel, C. Rapson, M. Reich, O. Sauter, U. Sheikh, C. Sozzi, G. Spizzo, J. Stober, W. Treutterer, P. Zanica, and t. E. M. T. ASDEX Upgrade team, TCV team. Path-oriented early reaction to approaching disruptions in asdex upgrade and tcv in view of the future needs for iter and demo. Plasma Physics and Controlled Fusion, 60(1):014047, nov 2017. URL: <https://dx.doi.org/10.1088/1361-6587/aa8d05>, doi:10.1088/1361-6587/aa8d05.
- [65] V. Igochine. Investigation of mhd instabilities in conventional and advanced tokamak scenarios on asdex upgrade, 2002.
- [66] P. H. Rutherford. Nonlinear growth of the tearing mode. The Physics of Fluids, 16(11):1903–1908, 1973. URL: <https://aip.scitation.org/doi/abs/10.1063/1.1694232>, arXiv:<https://aip.scitation.org/doi/pdf/10.1063/1.1694232>, doi:10.1063/1.1694232.
- [67] E. Nardon, A. Fil, M. Hoelzl, G. Huijsmans, and J. contributors. Progress in understanding disruptions triggered by massive gas injection via 3d non-linear MHD modelling with JOREK. Plasma Physics and Controlled Fusion, 59(1):014006, 2017. URL: <http://stacks.iop.org/0741-3335/59/i=1/a=014006>.
- [68] R. Fitzpatrick. Helical temperature perturbations associated with tearing modes in tokamak plasmas. Physics of Plasmas, 2(3):825–838, 1995. URL: <https://doi.org/10.1063/1.871434>, arXiv:<https://doi.org/10.1063/1.871434>, doi:10.1063/1.871434.
- [69] L. Spitzer and R. Härm. Transport phenomena in a completely ionized gas. Phys. Rev., 89:977–981, Mar 1953. doi:10.1103/PhysRev.89.977.
- [70] O. Sauter, C. Angioni, and Y. R. Lin-Liu. Neoclassical conductivity and bootstrap current formulas for general axisymmetric equilibria and arbitrary collisionality regime. Physics of Plasmas, 6(7):2834–2839, 1999. URL: <https://doi.org/10.1063/1.873240>, arXiv:<https://doi.org/10.1063/1.873240>, doi:10.1063/1.873240.
- [71] A. Bock, E. Fable, R. Fischer, M. Reich, D. Rittich, J. Stober, M. Bernert, A. Burckhart, H. Doerk, M. Dunne, B. Geiger, L. Giannone, V. Igochine, A. Kappatou, R. McDermott, A. Mlynek, T. Odstrčil, G. Tardini, H. Zohm, and T. A. U. Team. Non-inductive improved h-mode operation at asdex upgrade. Nuclear Fusion, 57(12):126041, oct 2017. URL: <https://dx.doi.org/10.1088/1741-4326/aa8967>, doi:10.1088/1741-4326/aa8967.

- [72] V. Pustovitov. Resonant field amplification as a mechanism for seed island formation. *Nuclear Fusion*, 45(4):245, mar 2005. URL: <https://dx.doi.org/10.1088/0029-5515/45/4/004>, doi:10.1088/0029-5515/45/4/004.
- [73] R. L. Haye, R. Prater, R. Buttery, N. Hayashi, A. Isayama, M. Maraschek, L. Urso, and H. Zohm. Crossmachine benchmarking for iter of neoclassical tearing mode stabilization by electron cyclotron current drive. *Nuclear Fusion*, 46(4):451, 2006. URL: <http://stacks.iop.org/0029-5515/46/i=4/a=006>.
- [74] M. Hoelzl, G. Huijsmans, S. Pamela, M. Bécoulet, E. Nardon, F. Artola, B. Nkonga, C. Atanasiu, V. Bandaru, A. Bhole, D. Bonfiglio, A. Cathey, O. Czarny, A. Dvornova, T. Fehér, A. Fil, E. Franck, S. Futatani, M. Gruca, H. Guillard, J. Haverkort, I. Holod, D. Hu, S. Kim, S. Korving, L. Kos, I. Krebs, L. Kriepner, G. Latu, F. Liu, P. Merkel, D. Meshcheriakov, V. Mitterauer, S. Mochalsky, J. Morales, R. Nies, N. Nikulsin, F. Orain, J. Pratt, R. Ramasamy, P. Ramet, C. Reux, K. Särkimäki, N. Schwarz, P. S. Verma, S. Smith, C. Sommariva, E. Strumberger, D. van Vugt, M. Verbeek, E. Westerhof, F. Wieschollek, and J. Zielinski. The JOREK non-linear extended MHD code and applications to large-scale instabilities and their control in magnetically confined fusion plasmas. *Nuclear Fusion*, 61(6):065001, may 2021. URL: <https://doi.org/10.1088/1741-4326/abf99f>, doi:10.1088/1741-4326/abf99f.
- [75] G. Huysmans and O. Czarny. Mhd stability in x-point geometry: simulation of elms. *Nuclear Fusion*, 47(7):659, 2007. URL: <http://stacks.iop.org/0029-5515/47/i=7/a=016>.
- [76] O. Czarny and G. Huysmans. Bézier surfaces and finite elements for mhd simulations. *Journal of Computational Physics*, 227(16):7423 – 7445, 2008. URL: <http://www.sciencedirect.com/science/article/pii/S0021999108002118>, doi:<https://doi.org/10.1016/j.jcp.2008.04.001>.
- [77] C. Sovinec, A. Glasser, T. Gianakon, D. Barnes, R. Nebel, S. Kruger, D. Schnack, S. Plimpton, A. Tarditi, M. C. f, and the NIMROD Team. Nonlinear magnetohydrodynamics simulation using high-order finite elements. *Journal of Computational Physics*, 195(1):355 – 386, 2004. URL: <http://www.sciencedirect.com/science/article/pii/S0021999103005369>, doi:<https://doi.org/10.1016/j.jcp.2003.10.004>.
- [78] W. Park, E. V. Belova, G. Y. Fu, X. Z. Tang, H. R. Strauss, and L. E. Sugiyama. Plasma simulation studies using multilevel physics models. *Physics of Plasmas*, 6(5):1796–1803, 1999. URL: <https://doi.org/10.1063/1.873437>, arXiv:<https://doi.org/10.1063/1.873437>, doi:10.1063/1.873437.
- [79] S. Jardin. A triangular finite element with first-derivative continuity applied to fusion mhd applications. *Journal of Computational Physics*, 200(1):133 – 152, 2004. URL: <http://www.sciencedirect.com/science/article/pii/S0021999104001366>, doi:<https://doi.org/10.1016/j.jcp.2004.04.004>.

BIBLIOGRAPHY

- [80] R. Sweeney, W. Choi, R. L. Haye, S. Mao, K. Olofsson, F. Volpe, and The DIII-D Team. Statistical analysis of $m/n = 2/1$ locked and quasi-stationary modes with rotating precursors at DIII-d. *Nuclear Fusion*, 57(1):016019, nov 2016. URL: <https://doi.org/10.1088/0029-5515/57/1/016019>, doi:10.1088/0029-5515/57/1/016019.
- [81] D. Hu, G. T. A. Huijsmans, E. Nardon, M. Hoelzl, M. Lehnen, D. Bonfiglio, and J. Team. Collisional-radiative non-equilibrium impurity treatment for jorek simulations. *Plasma Physics and Controlled Fusion*, 63(12):125003, oct 2021. URL: <https://dx.doi.org/10.1088/1361-6587/ac2afb>, doi:10.1088/1361-6587/ac2afb.
- [82] H. Summers. The ADAS user manual, version 2.6, 2004. URL: <http://www.adas.ac.uk>.
- [83] K. Gál, É. Belonohy, G. Kocsis, P. Lang, G. Veres, and the ASDEX Upgrade Team. Role of shielding in modelling cryogenic deuterium pellet ablation. *Nuclear Fusion*, 48(8):085005, jul 2008. URL: <https://doi.org/10.1088/0029-5515/48/8/085005>, doi:10.1088/0029-5515/48/8/085005.
- [84] C. Hirsch. Chapter 9 - time integration methods for space-discretized equations. In C. Hirsch, editor, *Numerical Computation of Internal and External Flows (Second Edition)*, pages 413 – 489. Butterworth-Heinemann, Oxford, second edition edition, 2007. URL: <http://www.sciencedirect.com/science/article/pii/B9780750665940500527>, doi:<https://doi.org/10.1016/B978-075066594-0/50052-7>.
- [85] P. Hénon, P. Ramet, and J. Roman. Pastix: a high-performance parallel direct solver for sparse symmetric positive definite systems. *Parallel Computing*, 28(2):301 – 321, 2002. URL: <http://www.sciencedirect.com/science/article/pii/S0167819101001417>, doi:[https://doi.org/10.1016/S0167-8191\(01\)00141-7](https://doi.org/10.1016/S0167-8191(01)00141-7).
- [86] W. S. P.J McCarthy, P. Martin. The CLISTE interpretive equilibrium code, 1999. URL: http://inis.iaea.org/search/search.aspx?orig_q=RN:31057068.
- [87] I. Krebs, F. J. Artola, C. R. Sovinec, S. C. Jardin, K. J. Bunkers, M. Hoelzl, and N. M. Ferraro. Axisymmetric simulations of vertical displacement events in tokamaks: A benchmark of M3D-C1, NIMROD, and JOREK. *Physics of Plasmas*, 27(2):022505, 2020. URL: <https://doi.org/10.1063/1.5127664>, arXiv:<https://doi.org/10.1063/1.5127664>, doi:10.1063/1.5127664.
- [88] A. M. Arnold, P. Aleynikov, and P. Helander. Self-similar expansion of a plasmoid supplied by pellet ablation. *Plasma Physics and Controlled Fusion*, 63(9):095008, aug 2021. URL: <https://doi.org/10.1088/1361-6587/ac138d>, doi:10.1088/1361-6587/ac138d.
- [89] B. Pégourié. Review: Pellet injection experiments and modelling. *Plasma Physics and Controlled Fusion*, 49(8):R87–R160, jul 2007. URL: <https://doi.org/10.1088/0741-3335/49/8/r01>, doi:10.1088/0741-3335/49/8/r01.

- [90] R. Sweeney, W. Choi, M. Austin, M. Brookman, V. Izzo, M. Knolker, R. L. Haye, A. Leonard, E. Strait, and F. V. and. Relationship between locked modes and thermal quenches in DIII-d. Nuclear Fusion, 58(5):056022, mar 2018. doi:10.1088/1741-4326/aaaf0a.
- [91] V. A. Izzo. The effect of pre-existing islands on disruption mitigation in mhd simulations of diii-d. Physics of Plasmas, 24(5):056102, 2017. doi:10.1063/1.4977462.
- [92] F. Hitzler, M. Wischmeier, F. Reimold, D. P. Coster, and the ASDEX Upgrade Team. Impurity transport and divertor retention in ar and n seeded solps 5.0 simulations for asdex upgrade. Plasma Physics and Controlled Fusion, 62(8):085013, jul 2020. URL: <https://dx.doi.org/10.1088/1361-6587/ab9b00>, doi:10.1088/1361-6587/ab9b00.
- [93] R. Neu, R. Dux, A. Geier, A. Kallenbach, R. Pugno, V. Rohde, D. Bolshukhin, J. C. Fuchs, O. Gehre, O. Gruber, J. Hobirk, M. Kaufmann, K. Krieger, M. Laux, C. Maggi, H. Murmann, J. Neuhauser, F. Ryter, A. C. C. Sips, A. Stäbler, J. Stober, W. Suttrop, H. Zohm, and the ASDEX Upgrade Team. Impurity behaviour in the asdex upgrade divertor tokamak with large area tungsten walls. Plasma Physics and Controlled Fusion, 44(6):811, may 2002. URL: <https://dx.doi.org/10.1088/0741-3335/44/6/313>, doi:10.1088/0741-3335/44/6/313.
- [94] E. Nardon, D. Hu, J. Artola, the JOEKE team, and JET Contributors. 3D non-linear MHD modelling of massive gas injection-triggered disruptions in JET. Oral presentation at the 7th Theory and Simulation of Disruptions Workshop, Princeton, 8 2019. URL: <https://tsdw.pppl.gov/Talks/2019/Nardon.pdf>.
- [95] BNetzA. Bundesnetzagentur prüft Anträge zu systemrelevanten Anlagen der ersten Ausschreibung zum Kohleausstieg. Press Release, March 2021. URL: https://www.bundesnetzagentur.de/SharedDocs/Pressemitteilungen/DE/2021/20210304_Kohle.html [last checked 31. Januar 2023].

List of Figures

1.1	Schematic sketch of flux surfaces within a tokamak. Black lines represent the helical field lines on some flux surfaces (white). The poloidal flux Ψ of the outermost flux surface is defined as the flux going through the blue area S_p , while the toroidal flux Φ is defined by the red area S_t . The magnetic axis is marked in orange. The central solenoid lies close to the torus axis (green). Figure excerpted from [6].	3
1.2	Poloidal cross-section of flux surfaces of a plasma in divertor configuration. The plasma is divided by the separatrix (blue) into the inner region of closed magnetic field lines and the outer region of open field lines. Field lines outside the separatrix hit the divertor plates (black). Figure excerpted from [6].	4
1.3	Schematic sequence of events during a disruption.	6
2.1	Basic procedure of an injection: in the cooling chamber, a pellet is formed by gas condensation (1). The pellet's form is controlled by several barrel heaters, which acts in different ways during and after the pellet formation (2). Using a propellant gas, the pellet is pushed at a speed in the order of hundreds of m/s into the pipe towards the plasma (right direction) (3). The tube has a miter bend in the end, so that the pellet crashes and shatters (4). The shards are injected through the nozzle into the plasma (5). Graphic adopted with courtesy of Paul Heinrich.	13
2.2	Poloidal cut of the ASDEX Upgrade vessel. The injector is located in Port S16. The shatter bends are about 35 cm and 39 cm above the midplane, with the aim to shoot at the axis.	15
2.3	Shatter head configuration in the 2022 SPI campaign inside the vacuum vessel. Rectangular and circular shatter plates with different angles are mounted. Graphic and picture adopted with courtesy from Gergely Papp.	15
2.4	Schematic sketch of a kink mode. The Eigenfunction has a constant value inside the rational surface (at $\Psi_N = 0.6$) and drops to zero outside.	19
2.5	Schematic sketch of a tearing mode. A discontinuity of the first derivation at the radial position of the corresponding rational surface is an important property. The Eigenfunction is determined by the Rutherford equation. .	19
2.6	Schematic sketch of a (2/1) island. The surface in red is called the island separatrix. $\zeta \equiv \theta - \frac{n}{m}\phi$ is called the magnetic coordinate. O-Points at $\zeta = \frac{\pi}{2}$ and $\zeta = \frac{3\pi}{2}$; X-Points at $\zeta = 0$ and $\zeta = \pi$	21

LIST OF FIGURES

2.7 Equilibrium radiation coefficients of relevant elements at $n_e = 1 \times 10^{20}$ and varying T_e . The coefficients are calculated from OPEN-ADAS data. 25

3.1 Left: Profiles of the ASDEX Upgrade L-mode-like equilibrium considered in the present study. Right: poloidal cut of the initial flux surfaces with some relevant resonant surfaces marked as well as the average shard cloud position every 0.4 milliseconds. The core region ($\Psi_N \leq 0.1$) is shaded green. 30

3.2 Growth phase of the 2/1 island in the classically unstable equilibrium. Mode coupling is observable as described in [6]. Vertical lines mark the time points, from where the perturbations were taken and important into the classical stable equilibrium. 31

3.3 Evolution of total (top row) and core (bottom row) particle content (left column) and thermal energy content (right column) for runs without a pre-existing island. Dashed lines show the total particle content of the remaining shards of the corresponding run. The case of $N_{\text{SPI}} = 6 \times 10^{20}$ leads to a delayed FS about 1.5 ms after the shards started to dilute the core region and about 0.5 ms after full ablation. Simulations are usually stopped after reaching t_{FS} (marked by circles in the right upper plot), i.e., when FS is reached and the temperature in the whole plasma flattens. 34

3.4 Case with $N_{\text{SPI}} = 6 \times 10^{20}$. Magnetic energies show a strong coupling during the first MHD burst at $t = 1.2$ ms and successively a partial decay of the higher modes while $n = 1$ keeps growing continuously. The TQ onset is again correlated to strong mode coupling (around $t = 2.5$ ms). 36

3.5 Case with $N_{\text{SPI}} = 6 \times 10^{20}$. Poincaré plots are shown at various time points during the simulation, from an early stage where only small islands have formed up to the point of FS. 37

3.6 Midplane profiles of density (top), temperature (middle) and pressure (bottom) are shown for the case with $N_{\text{SPI}} = 6 \times 10^{20}$. A rapid drop of central temperature as well as central pressure occurs, when the first shards pass the $q = 3/2$ surface at $t = 1.2$ ms. The pressure profile becomes hollow after this first crash while the core gets continuously diluted (see density at the top). Only during the second crash corresponding to full stochastization (around $t = 2.5$ ms), pressure, temperature and density profiles flatten across the whole plasma domain. The trajectories of each shard are shown by black-orange lines, where the color represents the respective fraction of the material ablated. 38

3.7 Evolution of the 2/1 island width for two approaches of calculating the Spitzer-resistivity η . When it is calculated from the axisymmetric part of the temperature $T_{e,\text{axi}}$ (orange curve), the perturbation energy monotonously decays after $t = 0.6$ ms. The strongly increasing mode activity eventually leading to the TQ is only observed, when taking the helical temperature perturbations into account for the resistivity calculation (green curve). This confirms the important role of helical cooling, in particular on the $q = 2$ surface, for the plasma dynamics. 40

3.8 Complex phase (left) and amplitude (right) of the perturbed flux component $\Psi_{2/1}$ are shown in the early stage after injection. First (0.4 and 0.6 ms), a strongly kink dominated structure (phase shift at the $q = 2$ surface at $\Psi_N = 0.59$) is observed such that the small 2/1 island can be seen as a resistive MHD consequence of the strongly dominating ideal kink response. In this phase, the 2/1 island has the X-point in phase with the injection location. Later ($t \geq 0.8$ ms), the tearing structure starts to strongly dominate over the kink component, which coincides with the time at which helical cooling starts to take over as the main driver of the magnetic perturbation evolution. Here, the island O-Point is in phase with the shards, as expected for helical cooling ($\Psi_{2/1} \approx -\pi$). 41

3.9 Poloidal cuts for $N_{\text{SPI}} = 6 \times 10^{20}$ at $t = 0.6$ ms (left column) and $t = 1.0$ ms (right column), taken at the toroidal position of injection. The enhanced radial pressure gradient ∇p_r (top row) induces a kink parity plasma response. It relaxes and at $t = 1.0$ ms, the temperature perturbation T_e^* (bottom row) dominates, forming a tearing mode by helical cooling. 42

3.10 Evolution of total (top row) and core (bottom row) particle content (left column) and thermal energy content (right column) for injection without a pre-existing island (solid lines), an initial island width of $w_i = 2.4$ cm (tightly dashed) and $w_i = 6$ cm (loosely dashed). Time points of full stochastization are marked by circles. 43

3.11 Case of $N_{\text{SPI}} = 6 \times 10^{20}$. The evolution of the 2/1 island is hardly affected for small initial island sizes. For larger $w_i > 4$ cm, however, a transient decrease of the island sizes is observed, and the further growth is delayed by about 0.5 ms compared to the no-island case. This delay directly affects the time at which full stochastization is reached. Smaller fluctuation of each line are a non-physical artifact from the calculation of q' 44

3.12 Magnetic energy perturbations are plotted for the case with $w_i = 2.4$ cm (left) and $w_i = 6$ cm (right). The evolution of the energies is only weakly affected by small initial islands compared to the case without pre-existing island discussed in Section 3.2 and the non-linear coupling during the first crash is still very pronounced. For $w_i = 6$ cm, however, the $n = 1$ harmonic decays during and shortly after the first crash, which delays the growth of the $n = 1$ perturbation to the amplitude needed for the TQ onset. 45

3.13 Cases with $N_{\text{SPI}} = 6 \times 10^{20}$. Poincaré plots at several time points for $w_i = 2.4$ cm (top) and $w_i = 6$ cm (middle and bottom). 47

3.14 Case with $N_{\text{SPI}} = 6 \times 10^{20}$ and $w_i = 6$ cm. Up to the first crash ($t = 1.3$ ms), the evolution of temperature and pressure are very similar compared to cases without pre-existing island (Fig. 3.6) or with a small one. As a result of the delayed mode growth later on, the density profile remains hollow for a longer time and only flattens completely around $t = 3.6$ ms, when full stochastization is reached. 49

LIST OF FIGURES

3.15 Amplitude of the perturbed poloidal flux $\Psi_{2/1}$ of the cases with $w_i = 2.4$ cm (left) and $w_i = 6$ cm (right). When the initial amplitude ($t = 0.2$ ms) close to the $q = 2$ surface matches with the amplitude triggered by only the shards (perturbation of opposite phase), $\Psi_{2/1}$ cancels around $t = 0.6$ ms in the vicinity of $q = 2$ ($\Psi_N = 0.63$), which makes the otherwise sub-dominant $4/2$ structure visible for $w_i = 2.4$ cm (see Poincaré plots of Fig. 3.13). Dotted lines show the $\Psi_{4/2}$ component at $t = 0.6$ ms. For $w_i = 6$ cm, the initial $\Psi_{2/1}$ at $q = 2$ is much larger, such that a cancellation is not possible. 50

3.16 Injections into the X-point for different N_{SPI} and w_i . Evolution of total (top row) and core (bottom row) particle content (left column) and thermal energy content (right column) for injection without a pre-existing island (solid lines) and initial island with $w_i = 2.4$ cm (tightly dashed) and $w_i = 6$ cm (loosely dashed). Time points of full stochastization are marked by circles in the right upper plot. In contrast to the injection into the O-point, the core crash (of cases with $N_{\text{SPI}} = 3 \times 10^{20}$) respectively the full TQ (of cases with $N_{\text{SPI}} = 6 \times 10^{20}$) sets in earlier, which becomes in particular visible in the evolution of E_{tot} 54

3.17 Island widths in the cases with $N_{\text{SPI}} = 6 \times 10^{20}$, $w_i = 6$ cm and different injection phase. Injecting into the X-point ($\phi_0 = 180^\circ$) leads to a small island decrease, when shards pass the $q = 2$ surface ($t = 0.8$ ms). After $t = 1.0$ ms, the island growth is clearly enhanced for the XI-case, leading to the TQ occurring earlier than in the other cases. 55

3.18 Case with $N_{\text{SPI}} = 6 \times 10^{20}$, $w_i = 6$ cm and X-point injection. When shards reach the $q = 2$ surface, the island gets suppressed transiently ($t = 0.8$ ms). Hereafter, its O-point aligns with the shards and begins to grow rapidly. After the first crash at $t = 1.2$ ms, flux surfaces are not reforming ($t = 1.5$ ms) and the plasma becomes fully stochastic around $t = 1.8$ ms. 55

3.19 Case with $N_{\text{SPI}} = 6 \times 10^{20}$, $w_i = 6$ cm and X-point injection. Up to the first core crash, temperature and density behave similarly compared to the runs with other injection phases. However, due to the strong stochastization after $t = 1.5$ ms related to the rapid $2/1$ island growth, the hollow pressure profile is quickly lost as temperature and density profiles flatten already $t = 0.5$ ms after the onset of the first crash. 56

3.20 Evolution of the radial current density gradient for the NI- (top), OI- case (middle) and XI-case (bottom) with $w_i = 6$ cm. The radial position of the $q = 2$ surface is given in green. In the NI- and XI-cases, $\nabla_{\Psi_N} j$ is always negative (red) slightly inside the $q = 2$ surface after $t = 0.9$ ms (and also positive slightly outside of the $q = 2$ surface in the XI-case), which acts destabilizing. In the OI-case, however, it is flat (white) or positive (blue) at $q = 2$, which stabilizes the mode up to $t = 1.9$ ms. 57

3.21 Poloidal cuts of the temperature perturbation in the OI-case (top row) and the XI-case (bottom row), taken at the respective toroidal position of injection. As a response to the injection into the O-Point, the 2/1 perturbation at $q = 2$ is amplified, which causes the observed island growth beginning from $t = 0.8$ ms. It decays after $t = 1.0$ ms which is one cause for the island decay up to $t = 1.8$ ms. Injecting into the X-point reduces the initial perturbation in the early phase ($t < 1.0$ ms). Later on ($t = 1.5$ ms), a strong perturbation establishes, which drives the growth and position of the 2/1 island. 58

4.1 Radiative power of tungsten or argon for the concentrations selected in this study. While argon becomes strongly radiating at low temperatures (18 eV and 200 eV), which are reached within the core only during disruptions, tungsten may significantly reduce E_{th} even during normal operation due to a maximum around 1500 eV. 60

4.2 Evolution of total (top row) and core (bottom row) particle content (left column) and thermal energy content (right column) for injection without a pre-existing island (solid lines) or large initial island (dashed) and different concentrations of background argon. Time points of full stochastization are marked by circles. Due to enhanced Ohmic heating after dilution, the whole plasma reheats. In cases without impurities, this reheating prevents the full TQ. In cases with a full TQ, the injection into the O-point continues to have a retarding effect of about ≈ 0.3 ms. 61

4.3 Evolution of the 2/1 island width without impurities (solid) or 7% argon (dashed), O-point injection (ocher, left), X-point injection (ocher, right) or no pre-existing island (black). In cases without full TQ, the island saturates at about 15 cm. The sequence of decreasing island size for O-point injection after $t = 1.5$ ms is clearly reduced by impurities. For X-point injection, the island growth is marginally affected by impurities, which is related to the effect, that only for X-point injection, a TQ can be triggered independently of impurities under the conditions of this setup. 62

4.4 O-point injection and no impurities. During the first crash, only the region $q < 2$ becomes stochastic, while flux surfaces in the outer region establish, leading to a regain of thermal insulation. In the further course, due to Ohmic heating, high m/n modes in the core and the 2/1 mode are not as excited enough to trigger a full TQ: flux surfaces in the center remain intact. 64

4.5 Midplane profiles of pressure (top) and Ohmic heating (bottom) are shown for NI-case and no background impurities. During the first crash, Ohmic heating becomes significant. This leads to a heating of the $q = 2$ surface, as well as the core region. As a consequence, pressure in the core is fully regained after $t > 4$ ms. 64

LIST OF FIGURES

4.6 Midplane profiles of pressure (top) and Ohmic heating (bottom) are shown for the OI-case and no background impurities. The first crash around $t = 1.8$ ms is less violent, which keeps the pressure in the core at a larger value than in the NI-case. Also, material accumulates within the pre-existing islands, which reheats. This effect is more prone here compared to the cases without Ohmic heating (see Fig. 3.14). 65

4.7 Midplane profiles of pressure (top) and Ohmic heating (middle) and radiative cooling (bottom) are shown for NI-case and 7% argon impurities. The Ohmic heating is merely compensated by the radiative cooling. As a consequence, the dynamics are fairly similar as in the case without P_Ω or P_{rad} and a full TQ is reached at $t = 3$ ms. 66

4.8 Midplane profiles of pressure (top) and Ohmic heating (middle) and radiative cooling (bottom) are shown for the OI-case and with 7% argon impurities. Even though lots of Ohmic heating is radiated away also in this case, it is still dominating in the final phase of the simulation ($t > 3.3$ ms and a full collapse of the pressure profile is not reached. 67

4.9 O-point injection with $n_{\text{bg,Arg}} = 7\%$. Due to the radiative cooling of the edge, it stays stochastic during the whole simulation sequence, causing a degradation of the heat confinement. Because of this, growth rates of 2/1 mode and other modes of higher order is enhanced and nearly FS is detected during the seconds crash ($t = 3.4$ ms). 68

4.10 Evolution of total (left) and core (right) thermal energy content for injection without impurities (solid lines) and 7% argon (dashed) for different configurations of a pre-existing island. Time points of FS are marked by circles. In cases without impurities, Ohmic reheating prevents the FS. Injection with $\phi_0 = 90^\circ$ (injection between X- and O-point) leads to FS at a similar time point compared to the no-island case. The XI-case clearly accelerates the FS by ≈ 0.5 ms. 68

4.11 XI-case with argon impurities. After injection, the 2/1 island starts to grow, changes its phase and then region $q > 2$ stochastizes. When shards reach the $q = 2$ surface, also the core becomes stochastic gradually. For a short time period ($t = 2 \dots 2.3$ ms), flux surfaces in the center reestablish. Full TQ at $t = 2.5$ ms. For better comparison, the selected times corresponds to Fig. 3.18 with a shift of 0.5 ms. 70

4.12 Evolution of total (left) and core (right) thermal energy content (right column) for injection without a pre-existing island (solid lines) or O-point injection into a large initial island (dashed) and different concentrations of background tungsten. Time points of full stochastization are marked by circles. Tungsten only affects the dynamics for a large concentration of $n_{\text{bg,T}} = 0.5\%$. While a TQ sets in around $t = 3.6$ ms for this large concentration in the no-island case, the TQ is completely suppressed in the regarding OI-case. 71

LIST OF FIGURES

4.13 Evolution of the 2/1 island width without impurities (solid lines) or 0.5% tungsten (dashed), O-point injection (left) or X-point injection (right). In case of O-point or X-point injection, tungsten has virtually no effect, while it may trigger the FS in the NI-case. 72

4.14 Midplane profiles of pressure (top) and Ohmic heating (middle) and radiative cooling (bottom) are shown for the NI-case and with 0.5% tungsten impurities. Tungsten radiates in the core even before the disruption onset, but only at small values. P_{rad} significantly increases around the $q = 2$ only during the first crash ($t = 1.7$ ms) and is still below the level of P_{rad} from argon. The island drive caused by this cooling is sufficient, nevertheless, to drive the plasma into FS at $t = 4$ ms. 72

All figures are drawn by myself unless explicitly stated otherwise.

Acknowledgements

Foremost, I want to thank Matthias Hoelzl as my scientific supervisor, who has supported me during this adventure over the last 3.5 years. Only through him, my project found a shape, the paper writing in 2021 became a success and many ideas and improvements find their origin with him. Thank you for enduring my average physics skills and sometimes lack of motivation over such a long time! I thank Sibylle Günter for giving me the opportunity to conduct this project at IPP and also for supporting me regularly, together with Valentin Igochine and Karl Lackner. Besides of that, it was a great pleasure to work closely together with Eric Nardon over the years, having deep discussion about SPI simulations. His broad ideas became an important part of this thesis. Additionally, I thank the whole SPI-group of JOREK, including Di Hu, Mengdi Kong, Daniele Bonfiglio and Sang-Jun Lee. The disruption meeting we had regularly (for a certain time at least) were really motivating and insightful. Geri Papp became an important person regarding experimental SPI questions, and he helped me greatly by explaining things in a very detailed way. If it was about runaway electrons, I often came across Vinodh Bandaru who helped me a lot in understanding the physics of these crazy beasts. Apart from that, I had many great discussions with him about nuclear fusion and its (too) complicated properties. The JOREK group itself gave a wonderful environment, where I'm glad to have worked and laughed together with Nina Schwarz, Rohan Ramasamy, Andres Cathey, Javier Artola and Nikita Nikulsin. The discussions I had with Sergei Makarov became very deeply thanks to his curiosity about plasma physics, but also energy policy issues. (The wine drinking together is still to come!). I had and have deep discussion with Nathan de Oliveira as well, where his unconventional style of writing a PhD thesis motivated me to write an additional unconventional chapter for this thesis as well. (Well, I don't know if this additional chapter "Epilogue: the hope of redemption through technology in the 21st century" will ever be finalized and published somewhere.)

Darüber hinaus gilt ein ganz besonderer Dank auszusprechen einer Person, welche gar nicht dieser Arbeit selber zutrug, aber meinem darauf folgenden weiteren Lebensweg, indem sie mir die Augen öffnete. Als ich David Fuchs während der Coronazeit am 4. März 2021 via Zoom freudig erzählte, dass für drei Kohlekraftwerke, die nach der ersten Ausschreibung gemäß §32 KVBG aus dem Markt gegangen waren, eine langfristige Reservehaltung durch die BNetzA[95] geprüft werden musste, stellte er fest: "Du bist kein Plasmaphysiker. Du musst in die Entwicklung von Energiesystemen." Und damit hatte er absolut recht. Er erkannte, dass ich mich über die Jahre damit belog, meinen Sinn in der Entwicklung des vermeintlichen heiligen Gral der Energieerzeugung zu sehen, aber mich dabei viel mehr für die tagesaktuelle Energiewirtschaft und realistisch einsetzbare Techniken interessierte. Es brauchte nur wen, der mir das mal klar sagte. So bin ich

LIST OF FIGURES

sehr froh, dass ich meinen Lebensweg ab diesem Zeitpunkt immer mehr in die richtige Richtung korrigierte und nun bei einem dafür perfekten Arbeitgeber gelandet bin.